Development of terahertz systems using quantum cascade lasers and photomixers

Siddhant Chowdhury

Submitted in accordance with the requirements for the degree of
Doctor of Philosophy

The University of Leeds
School of Electronic and Electrical Engineering

September 2015

The candidate confirms that the work submitted is his own, except where work which has formed part of jointly authored publications has been included. The contribution of the candidate and the other authors to this work has been explicitly indicated below. The candidate confirms that appropriate credit has been given within the thesis where reference has been made to the work of others.

Devices fabricated in Chapter 2 of the thesis appeared in publications as follows:

"Coherent three-dimensional terahertz imaging through self-mixing in a quantum cascade laser", P. Dean, A. Valavanis, J. Keeley, K. Bertling, Y. Leng Lim, R. Alhathlool, *S. Chowdhury*, T. Taimre, L. Li, D. Indjin, S. J. Wilson, A. D. Rakić, E. H. Linfield and A. G. Davies, *Applied Physics Letters*, Vol. 103, No. 18, 2013.

Siddhant Chowdhury was responsible for fabrication of the sample measured in the work. Other authors were responsible for fabrication, measurements, data analysis, semiconductor material growth, and supervision of the work.

The work in Chapter 3 of the thesis appeared in publications as follows:

"Diffuse-reflectance spectroscopy using a frequency-switchable terahertz quantum cascade laser", A. Valavanis, *S. Chowdhury*, A. D. Burnett, A. R. Clarkson, D. R. Bacon, S. P. Khanna, A. G. Davies, E. H. Linfield and P. Dean, *IEEE Transactions on Terahertz Science and Technology*, [accepted].

Siddhant Chowdhury was involved in preparation of the powdered samples, measuring them using diffuse reflectance imaging and terahertz time-domain spectroscopy systems, and analysis of experimental data using Kulbeka–Munk theory. Other authors were responsible for development of the experimental technique, fabrication, measurements, data analysis, semiconductor material growth, and supervision of the work.

The work in Chapter 4 of the thesis appeared in publications as follows:

"Study of the effect of annealing temperature on low-temperature-grown-GaAs photomixers", S. Chowdhury, J. R. Freeman, M. C. Rosamond, R. A. Mohandas, M. Kumar, L. Li, P. Dean, A. G. Davies and E. H. Linfield, *UK Semiconductors,* Sheffield, UK, 2015.
Siddhant Chowdhury was involved in designing and fabrication of the photomixer device, building the experimental setup, performing the characterisation of each photomixer devices and analysing the data. Other authors were responsible for fabrication, measurements, semiconductor material growth, and supervision of the work.

"Generation of continuous wave terahertz radiation from Fe-doped InGaAs and InGaAsP", R. A. Mohandas, J. R. Freeman, M. C. Rosamond, *S. Chowdhury*, L. Ponnampalam, M. Fice, A. J. Seeds, P. J. Cannard, M. J. Robertson, D. G. Moodie, A. G. Davies, E. H. Linfield and P. Dean, *International Conference on Infrared, Millimeter, and Terahertz Waves*, HongKong, 2015.

Siddhant Chowdhury designed the photomixer device structure. Other authors were responsible for fabrication, measurements, data analysis, semiconductor material growth, and supervision of the work.

In Loving Memory of my Grandparents
–Late Smt Savitri Devi Chowdhury and Late Shri Tarachand Chowdhury

"The mind is not a vessel to be filled,
but a fire to be kindled."
–Plutarch

Acknowledgements

First and foremost, I would like to thank God or I would like to call it Mother Nature, for beautifully unwinding my life so far.

Words by itself may not do completely justice when it comes to expressing my gratitude towards my supervisors, Prof. Edmund H. Linfield, Prof. A. Giles Davies and Dr Paul Dean. They believed in me and gave an opportunity to do a PhD. For the entire duration, they were a constant source of motivation and positive energy. This seems to be an appropriate platform to mention that I had very limited background knowledge of semiconductor and optics, until I joined University of Leeds in September, 2008 for my undergraduate degree. It was Prof. Linfield's lectures on semiconductor materials and devices which nurtured my interest in this amazing field. Also, I would like to acknowledge Prof. John E. Cunningham for his valuable suggestions during supervisory meetings.

I would like to thank Dr Joshua R. Freeman, Dr Alexander Valavanis, and Dr Andrew D. Burnett for sharing their immense knowledge and helping me at different stages of this PhD. I would be lying if I said that writing this thesis would have been possible without your help. I would also like to thank Dr Osama Hatem and Dr Kashif Saeed for their help during the initial days of my PhD.

During the course, there was a research visit to *Lehrstuhl Für Angewandte Festkörperphysik*, Ruhr-Universität Bochum, Germany, along with Mr David Bacon. I would like to thank Dr Nathan Jukam and Prof. Andreas D. Wieck for such a warm welcome and organising everything from accommodation to experimental work. I would also like to thank all the members of the group including Dr Hanond Nong and Dr Shuvon Pal for making the visit a memorable one.

I owe a special thank you to Dr Mark C. Rosamond as his help in cleanroom

from training to fabrication has been immense. Without him doing the electron beam lithography, I could not have fabricated and measured the photomixers presented in this work. I would also like to thank Dr Li Chen for providing all the necessary trainings and helping hand in the cleanroom. I would also thank Dr Lianhe Li for MBE growth of all the semiconductor wafers. I would like to appreciate Mr Geoff Butterworth and Mr Jordan Thomas for all their support in the cleanroom. For providing all the administrative support, I would like to thank Ms Louise Redmonds, Mrs. Susan Hobson, Mrs. Clair Atkinson and Mrs. Anna De Jong.

I would also like to thank my colleagues Dr Iman Kundu, Ms Reshma A. Mohandas, Mr David Bacon, Mr Manoj Kumar, Dr Divyang Mistry, Dr Nickolas Hunter, Mr James Keeley, Mr Viktor Doychinov, Mr Dong Rui, and Dr Muhammad Y. Sandhu. Because of all of you guys, the journey towards my PhD was full of amazing moments! Finally, I would like to thank all the staff and students at Institute of Microwave and Photonics, School of Electronic and Electrical Engineering, University of Leeds.

I would also thank all my friends, especially Mr Ghulam Abbas, Mr Aamir Awan, Mr. Utkarsh Rana and Ms Neha Agarwal for extending their support all throughout, keeping me motivated, and being my small family away from home.

I am indebted to my parents, in-laws and close family for all their love, patience and support throughout. I hope you will feel proud DAD! The person whom I owe my entire life to is my Guruji– Mahatma Anand Priyadarshi. If it was not you, I would not be what I am today. The closest to my heart is my beautiful wife Karishma. Thank you my love for standing by me and being such an integral part of this journey.

Siddhant Chowdhury, September 2015

Abstract

The terahertz (THz) region of the electromagnetic spectrum lies between the more established bands of microwave and infrared radiation. In the past few decades, this region has seen huge growth in the development of both THz sources and detectors for a growing number of potential applications including security, wireless communications, medical diagnostics and astronomy. This thesis makes use of three different methods of generation of THz radiation, these being, THz quantum cascade lasers (QCLs), THz time-domain spectroscopy (TDS) and terahertz photomixing.

In the first set of experiments, diffuse reflectance imaging of a range of powered samples has been demonstrated using a THz QCL. Imaging was done at four discrete frequencies in the range of 3–3.35 THz by electrically tuning the emission wavelength of the laser. Absorption coefficients of the samples was inferred using Kubelka–Munk model and was found to be in good agreement with the Beer–Lambert absorption coefficient obtained from broadband (0.3–6 THz) THz-TDS measurements.

In the second part of the work, photomixers were designed and fabricated on low-temperature-grown (LTG) GaAs substrates. Ex-situ annealing temperature of LTG GaAs was optimised for maximum bandwidth of the photomixers and the impact on recombination lifetime and resistivity of LTG GaAs was also studied.

The final set of experiments examined locking a THz QCL to an external stable source. This would allow access to both amplitude and phase information of the laser emission, which in turn would significantly improve the quality of the data obtained from QCL based imaging techniques, making them useful in many different applications. After investigates of various techniques to achieve this, photomixers driven at telecommunications wavelengths (~1550 nm) were successfully used to obtain injection locking a THz QCL.

Table of contents

List of publications

The following were published by the author during the course of the presented research work.

Journal publications

- A. Valavanis, **S. Chowdhury**, A. D. Burnett, A. R. Clarkson, D. R. Bacon, S. P. Khanna, A. G. Davies, E. H. Linfield and P. Dean, "Diffuse-reflectance spectroscopy using a frequency-switchable terahertz quantum cascade laser", *IEEE Transactions on Terahertz Science and Technology*, [accepted].

  In this work, Siddhant Chowdhury was involved in preparation of the powdered samples, measuring them using diffuse reflectance spectroscopy and terahertz time-domain spectroscopy systems and analysis of experimental data using Kulbeka–Munk theory. Other authors were responsible for development of the experimental technique, fabrication, measurements, data analysis, semiconductor material growth, and supervision of the work.

- P. Dean, A. Valavanis, J. Keeley, K. Bertling, Y. Leng Lim, R. Alhathlool, **S. Chowdhury**, T. Taimre, L. Li, D. Indjin, S. J. Wilson, A. D. Rakić, E. H. Linfield and A. G. Davies, "Coherent three-dimensional terahertz imaging through self-mixing in a quantum cascade laser", *Applied Physics Letters*, vol. 103, no. 18, 2013.

  In this work, Siddhant Chowdhury was involved in fabrication of the sample measured. Other authors were responsible for fabrication, measurements, data analysis, semiconductor material growth, and supervision of the work.

- A. Valavanis, P. Dean, A. Scheuring, M. Salih, A. Stockhausen, S. Wuensch, K. Il'in, **S. Chowdhury**, S. P. Khanna, M. Siegel, A. G. Davies and E. H. Linfield, "Time-resolved measurement of pulse-to-pulse heating effects in a terahertz quantum cascade laser using an NbN superconducting detector", *Applied Physics Letters*, vol 103, no. 6, 2013.
- A. Scheuring, P. Dean, A. Valavanis, A. Stockhausen, P. Thoma, M. Salih, S. P. Khanna, **S. Chowdhury**, J. D. Cooper, A. Grier, S. Wuensch, K. Il'in, E. H. Linfield, A. G. Davies and M. Siegel, "Transient Analysis of THz-QCL Pulses

Using NbN and YBCO Superconducting Detectors", *IEEE Transactions on Terahertz Science and Technology,* 3(2), 172-179, 2013.

In these work, Siddhant Chowdhury helped in measurement and data acquisition of the devices. Other authors were responsible for fabrication, measurements, data analysis, semiconductor material growth, and supervision of the work.

Conference Publications

- **S. Chowdhury**, A. Valavanis, P. Dean, A. D. Burnett, S. P. Khanna, E. H. Linfield and A. G. Davies, "Diffuse reflectance imaging with a terahertz quantum cascade laser", *MITEPHO summer school*, London, UK, 2012. (Oral Presentation)

- A. Valavanis, P. Dean, L. Li, A. D. Burnett, J. Keeley, **S. Chowdhury**, R. Alhathlool, L. Chen, J. Zhu, Y. J. Han, J. R. Freeman, S. P. Khanna, D. Indjin, A. G. Davies, E. H. Linfield, T. Taimre, Y. L. Lim, K. Bertling and A. D. Rakic, "High-power (> 1 Watt) terahertz frequency quantum cascade lasers for stand-off imaging", *SET-210 Specialist Meeting on Novel infrared laser technology for modern battlefield requirements*, Salisbury, UK, 2014.

- A. Valavanis, P. Dean, **S. Chowdhury**, A. D. Burnett, S. P. Khanna, A. G. Davies and E. H. Linfield, "Spectroscopic analysis of powders through diffuse-reflectance imaging using a frequency-switchable terahertz quantum cascade laser", *International Conference on Infrared, Millimeter, and Terahertz Waves*, Mainz on the Rhine, Germany, 2013.

- A. Valavanis, P. Dean, Y. L. Lim, R. Alhatlool, A. D. Burnett, **S. Chowdhury**, R. Kliese , M. Nikolic, S. P. Khanna, M. Lachab, A. D. Rakić, A. G. Davies and E. H. Linfield "Feedback interferometry and diffuse reflectance imaging with terahertz quantum cascade lasers", *NATO Advanced Research Workshop on Detection of Explosives and CBRN (Using Terahertz)*, Cesme, Izmir, Turkey, 2012.

- A. Valavanis, P. Dean, Y. L. Lim, R. Alhatlool, A. D. Burnett, **S. Chowdhury**,

R. Kliese , M. Nikolic, S. P. Khanna, M. Lachab, D. Indjin, S. Wilson, A. D. Rakić, A. G. Davies and E. H. Linfield, "Detection of concealed weapons and characterisation of crystalline powders using terahertz quantum cascade lasers", *UK Semiconductors*, Sheffield, UK, 2012.

- A. Valavanis, P. Dean, A. D. Burnett, **S. Chowdhury**, A. Marshall, A. G. Davies and E. H. Linfield, "Terahertz frequency imaging for explosives and weapons detection", *IRC showcase event*, London, UK, 2011.

- A. Valavanis, P. Dean, A. D. Burnett, **S. Chowdhury**, A. G. Davies and E. H. Linfield, "Spectroscopic diffuse-reflectance imaging at a 1.5 m stand-off distance, using a frequency switchable terahertz quantum cascade laser", *The 11th International Conference on Intersubband Transitions in Quantum Wells*, Badesi, Italy, 2011.

In these work, Siddhant Chowdhury was involved in preparation of the powdered samples, measuring them using diffuse reflectance imaging and terahertz time-domain spectroscopy systems and analysis of experimental data using Kulbeka–Munk theory. Other authors were responsible for development of the experimental technique, fabrication, measurements, data analysis, semiconductor material growth, and supervision of the work.

- **S. Chowdhury**, J. R. Freeman, M. C. Rosamond, R. A. Mohandas, M. Kumar, L. Li, P. Dean, A. G. Davies and E. H. Linfield, "Study of the effect of annealing temperature on low-temperature-grown-GaAs photomixers", *UK Semiconductors*, Sheffield, UK, 2015. (Poster Presentation).

- **S. Chowdhury**, O. Hatem, P. Dean, R. Mohandas, L. Li, E. H. Linfield and A. G. Davies, "Terahertz emission and detection using Fe-doped InGaAs and low-temperature-grown-GaAs photoconductive switches", *UK Semiconductors*, Sheffield, UK, 2013. (Poster Presentation)

- **S. Chowdhury**, O. Hatem, P. Dean, L. Li, E. H. Linfield and A. G. Davies, "Terahertz emission and detection using Fe-doped InGaAs and low-temperature-grown-GaAs photoconductive switches", *MPNS COST Action Training School-MP1204 Tera-MIR Radiation: Materials, Generation, Detection* *and Application*, Cortona, Italy, 2013. (Poster presentation)

In these work, Siddhant Chowdhury was involved in designing and fabrication of the photomixer device, building the experimental setup, performing the characterisation of each photomixer devices and analysing the data. Other authors were responsible for fabrication, measurements, semiconductor material growth, and supervision of the work.

- R. A. Mohandas, J. R. Freeman, M. C. Rosamond, **S. Chowdhury**, L. Ponnampalam, M. Fice, A. J. Seeds, P. J. Cannard, M. J. Robertson, D. G. Moodie, A. G. Davies, E. H. Linfield and P. Dean, "Generation of continuous wave terahertz radiation from Fe-doped InGaAs and InGaAsP", *International Conference on Infrared, Millimeter, and Terahertz Waves*, HongKong, 2015.

  In this work, Siddhant Chowdhury designed the photomixer device structure. Other authors were responsible for fabrication, measurements, data analysis, semiconductor material growth, and supervision of the work.

- J. Keeley, P. Dean, A. Valavanis, T. Taimre, K. Bertling, Y. L. Lim, R. Alhathlool, **S. Chowdhury**, L. Li, D. Indjin, A. D. Rakic, E. H. Linfield, and A. G. Davies, "Electrical Modulation Schemes for Imaging by Self-Mixing in Terahertz Quantum Cascade Lasers", *International Quantum Cascade Lasers Summer School and Workshop*, Policoro, Italy, 2014.

- P. Dean, T. Taimre, A. Lui, K. Bertling, Y. L. Lim, A. Valavanis, J. Keeley, R. Alhathlool, **S. Chowdhury**, L. Li, S. P. Khanna, M. Lachab, D. Indjin, A. D. Rakic, E. H. Linfield, and A. G. Davies, "Coherent THz imaging using the self-mixing effect in quantum cascade lasers", *Optical Sensors, THz Sensing II, Optical Society of America*, Barcelona, Spain, 2014.

  In these work, Siddhant Chowdhury was involved in fabrication of the sample. Other authors were responsible for fabrication, measurements, data analysis, semiconductor material growth, and supervision of the work.

- A. Valavanis, P. Dean, A. Scheuring, M. Salih, A. Stockhausen, S. Wuensch, K. Il'in, **S. Chowdhury**, S. P. Khanna, M. Siegel, A. G. Davies and E. H. Linfield "Transient Analysis Of Substrate Heating Effects In A Terahertz

Quantum Cascade Laser Using An Ultrafast NbN Superconducting Detector”, *International Conference on Infrared, Millimeter, and Terahertz Waves*, Mainz on the Rhine, Germany, 2013.

- A. Scheuring, P. Dean, A. Valavanis, A. Stockhausen, P. Thoma, M. Salih, S. P. Khanna, **S. Chowdhury**, S. Wuensch, K. Il'in, E. H. Linfield, A. G. Davies and M. Siegel, “Analysis of THz pulses of a Quantum Cascade Laser in the time-domain using superconducting direct detectors”, Tagung Kryoelektronische Bauelemente, Freudenstadt-Lauterbad, Germany, 2012.

- A. Valavanis, P. Dean, A. Scheuring, M. Salih, S. P. Khanna, A. Stockhausen, **S. Chowdhury**, S. Wuensch, K. Il'in, M. Siegel, E. H. Linfield and A. G. Davies, “Time-resolved measurement of heating effects in a terahertz quantum cascade laser using an NbN superconducting detector”, International Quantum Cascade Lasers School and Workshop, Baden, Austria, 2012.

- P. Dean, A. Valavanis, M. Salih, S. P. Khanna, **S. Chowdhury**, E. H. Linfield, A. G. Davies, A. Scheuring, A. Stockhausen, P. Probst, S. Wuensch, K. Il'In and M. Siegel, ““Ultra-fast sampling of terahertz pulses from a quantum cascade laser using superconducting antenna-coupled NbN and YBCO detectors*”, International Conference on Infrared, Millimeter, and Terahertz Waves*, Wollongong, Australia, 2012.

In these work, Siddhant Chowdhury helped in measurement and data acquisition of the devices. Other authors were responsible for fabrication, measurements, data analysis, semiconductor material growth, and supervision of the work.

List of abbreviations

APC	Angled physical contact
AWG	Arbitrary waveform generator
CW	Continuous-wave
DAQ	Data Acquisition
DAST	4-N,N-dimethylamino-4′-N′-methyl stilbazolium tosylate
DI	De-ionised
DM	Dual mode
DR	Dynamic range
DRI	Diffuse reflection imaging
EBL	Electron-beam lithography
ECDL	External-cavity diode laser
EDFA	Erbium-doped fibre amplifier
EFA	Effective field approximation
EO	Electro-optic
EOPL	Effective-optical-path-length
ESA	Electrical spectrum analyser
ESD	Electrostatic discharge
FEL	Free electron laser
FFT	Fast Fourier transform
FOC	Fibre optic collimator
FTIR	Fourier transform infrared
FWHM	Full-width-half-maximum
HEB	Hot electron bolometer
IF	Intermediate frequency
IPA	Isopropyl alcohol
KM	Kubelka–Munk

LIV	Light-current-voltage
L-J	Light-current density
LO	Longitudinal optical
LTG	Low-temperature-grown
MBE	Molecular beam epitaxy
MIR	Mid-infrared
MSM	Metal-semiconductor-metal
MTF	Modulation transfer function
NF	Noise floor
OSA	Optical spectrum analyser
PC	Polarisation controller
PCB	Printed circuit board
PM	Polarisation maintaining
PMMA	Polymethyl methacrylate
PTFE	Polytetrafluoroethylene
QCA	Quasi-crystalline approximation
QCL	Quantum cascade laser
RBW	Resolution bandwidth
RTA	Rapid thermal annealer
RTD	Resonant tunnelling diodes
SI	Semi-insulating
SISP	Semi-insulating surface plasmon
SM	Single mode
SMU	Keithley 2400 series SourceMeter® unit
SNR	Signal-to-noise ratio
TDS	Time-domain spectroscopy
THz	Terahertz
TPI	Terahertz pulsed imaging

List of figures

List of tables

Chapter 1

Introduction

1.1 Background

The terahertz (THz) frequency region in the electromagnetic region is uniquely placed between the two very well developed microwave and the infrared bands. However, as the THz region is less developed than its neighbouring bands, it is often referred to as the 'Terahertz Gap' [1-3]. It can be defined as lying between 0.3–10 THz in frequency or ~1000–30 μm in wavelength [2], although historically, the precise range differs between authors. This *technology gap*; in the far-infrared range, was recognised back in 1897 by H. Rubens and E. F. Nichols who stated [4, 5]:

"*Since we have become accustomed to think of waves of electrical energy and light waves as forming component parts of a common spectrum, the attempt has often been made to extend our knowledge over the wide region which has separated the two phenomena, and to bring them closer together, …*"–H. Rubens & E. F. Nichols, Phy. Rev. 4, 314 (1897).

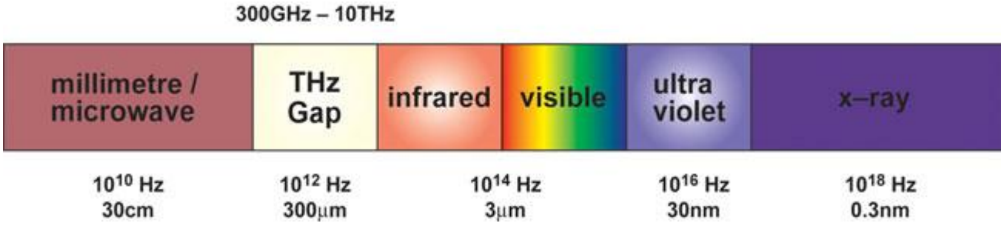

Figure 1.1: Electromagnetic spectrum highlighting the position of the terahertz region. Image taken from Ref. [6].

Initially, the terahertz region attracted astronomers and meteorologists due to the presence of unique spectral signatures from molecular rotations and excitations. Many cosmic emissions, such as those from cold interstellar clouds, the formation of stars, galactic evolution and even the Big Bang, are within the THz region [5, 7]. In fact, the whole universe is covered with plethora of (virtually invisible) THz radiation.

As THz radiation interacts with intermolecular vibrational modes, it can be used to detect chemical as well as structural information of different compounds [8]. THz radiation is also non-ionising due to its low photon energy and has the capability to penetrate optically opaque materials such as paper, clothes and plastics. It can traverse a few millimetres of biological tissue, but gets significantly absorbed by water molecules. Considering all of this, prospective applications for THz radiation have been identified in the fields of security and non-destructive imaging [9], pharmaceutical testing [10], spectroscopy [8, 11], investigation of condensed matter systems [12] and genetic sequencing [13]. As it can also penetrate through silicon, THz radiation can be used to investigate packaged integrated circuits [14]. Furthermore, there have been significant advances in non-invasive medical imaging and diagnostics such as detection *ex vivo* [15], and *ex vivo* and *in vivo* [16] of basal cell carcinoma, human breast tumours [17] and dental caries [18]. Due to significantly large bandwidth of the THz radiation, it can be used in high speed wireless communications [19, 20]. The potential of THz frequencies for studying space is enormous and has been comprehensively reported in Ref. [21]. As the field has matured with time, several extensive written books [22-32] and reviews on the development of the terahertz field [2, 5-7, 33-44] can also be found.

1.2 Terahertz sources

There are range of naturally available THz sources including cosmic radiations, the sun, and black-body radiation [36]. But these sources are very weak, incoherent and broadband. Hence, development of THz sources suitable for research and industrial applications has been necessary, and a comprehensive review of many THz sources can be found in Ref. [36].

Although the first successful demonstration of THz generation based on Hertzian oscillators, dates back to the 1920s [45], the region still lacks compact, room temperature, sources and detectors [2, 5, 37]. Frequency up-conversion from the electronics side of the spectrum, leads to a large roll-off in output power due to transit time and resistance–capacitance effects at such high frequencies [2]. For example, resonant tunnelling diodes (RTDs) have been reported at room temperature to operate up to 1.46 THz, but with only 0.36 μW output power [46] and planar Gunn diodes operating up to ~300 GHz have only 28 μW output power [47]. Similarly, frequency down-conversion from the optical side of the spectrum is challenging due to absence of semiconductor materials with such small band gap that can be processed into semiconductor devices. In the early 1980s, frequencies as low as ~6.5 THz were achieved using semiconductor heterojunction lasers based on PbSnTeSe solid solutions [48].

Alternative optical techniques have also been explored to generate THz radiation. THz radiation has been generated by using optical lasers to excite photomixers [49, 50], photoconductive antennas [51, 52], non-linear crystals for difference-frequency generation [53-55], THz parametric oscillators [56] and optical rectifiers [57, 58].

It should also be noted that there are higher power sources such as free electron lasers (FELs) [59] and optically pumped gas lasers [60, 61] available. Even though FELs provide kilowatts of power and tunability, they are extremely expensive, large, requires cryogenics and have high electrical power consumption, making them useful only for very limited scientific applications [62]. Gas lasers are also complex, expensive and bulky, and therefore not an attractive source for many industrial applications [62].

Semiconductor solid state lasers including THz quantum cascade lasers (QCLs) [63] and the p-doped germanium lasers [64] have also been developed. Both of these lasers are compact and cost effective but p-Ge lasers work at liquid helium temperatures, and THz QCLs have a maximum operating temperature of 199.5 K [65].

Three different approaches were used to generate terahertz radiation in this thesis. Pulsed THz radiation was generated using photoconductive switches (Chapter 3), continuous-wave THz radiation was generated using photomixing techniques (Chapter 4 and Chapter 5) and finally, THz radiation was generated both in pulsed and continuous-wave mode using THz QCLs (Chapter 2, Chapter 3 and Chapter 5). These techniques are now described further in this chapter.

1.3 Pulsed terahertz systems

Picosecond transient pulses can be generated by excitation of a photoconductive semiconductor material, and these pulses have a frequency bandwidth in the THz range. The generation and detection of picosecond pulses was first demonstrated using silicon-on-sapphire ultrafast photoconductive material, by D. H. Auston using a photoconductive switch, now commonly known as an Auston switch [66-68]. With the introduction of < 100 fs pulses from self-mode locked Ti:sapphire lasers [69], and improved photoconductive materials such as low-temperature-grown (LTG) GaAs and InGaAs, considerable work has been done to increase the output power and bandwidth of such systems [8].

THz pulses have also been generated in other ways such as using semiconductor surface fields [70], non-linear crystals [71], DAST [72, 73], the photo-Dember effect [74], semiconductor quantum structures [75], Bloch oscillations in a semiconductor superlattice [76], and coherent phonons in a semiconductor [77].

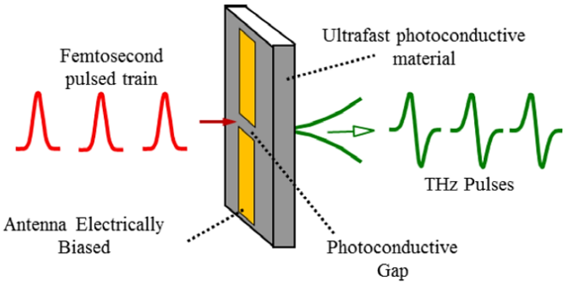

Figure 1.2: Femtosecond pulses focussed on a biased photoconductive gap (photoconductive switch) are used to generate pulsed THz radiation. Image taken from Ref. [78].

Photoconductive emitters (the Auston switch) are, however, by far the most efficient method of generating pulsed THz radiation using femtosecond lasers [8]. Figure 1.2 diagrammatically illustrates photoconductive generation of pulsed THz radiation using this technique. An antenna structure, such as bow-tie or dipole design, is fabricated on an ultrafast photoconductive semiconductor surface with a bias applied across the photoconductive gap. Femtosecond pulses generated from a mode-locked laser, which are above the bandgap of the semiconductor material, are focussed on the photoconductive gap. This generates photo-induced electron-hole pairs. These photo-excited carriers are accelerated under the influence of the applied electric field, resulting in the generation of transient current pulse. If the transients vary on a subpicosecond timescale then the emitted radiation will be in the THz region. The electric field intensity of the emitted THz radiation $\mathrm{E_{THz}}$ is proportional to the time derivative of the transient current density $\mathrm{J_{THz}}$. The current density can be expressed using the well-established expression $\mathrm{J_{THz}} = \mathrm{ne}\nu_d$, where n, e and ν_d are the carrier density, charge of an electron and drift velocity, respectively. The time derivative of the current density can be expressed as follows [78]:

$$\frac{\mathrm{dJ_{THz}}}{\mathrm{dt}} = \mathrm{ne}\frac{\mathrm{d}\nu_d}{\mathrm{dt}} + \frac{\mathrm{dn}}{\mathrm{dt}}\mathrm{e}\nu_d \qquad 1.1$$

For optimum THz emission, the photoconductive material should have a short electron-hole recombination time (carrier lifetime), allowing fast variation of current density. Also, the mobility of carrier should be high. High dark resistivity would also allow higher applied bias and hence increase of the emitted THz signal amplitude.

Intrinsic semiconductors such as GaAs do not have all the required properties to be an ideal candidate for THz generation, in particular the carrier lifetime is too large. Reduction of carrier lifetime can be achieved by introducing defects in the material. But this leads to lower mobility. Hence, however, a compromise is needed between requirements for short carrier lifetime, high resistivity and high mobility.

Conventionally GaAs is grown using molecular beam epitaxy (MBE) at ~600° C. Point defects are introduced by reducing the growth temperature to ~200–300° C in the presence of excess arsenic pressure. This creates donor sites close to the conduction band edge of the GaAs, resulting in a reduction of the electron-hole recombination time. Lifetimes as low as 90 fs have been reported [79]. Although point defects reduce the lifetime, they increase the availability of free carrier even without any optical illumination. To increase the dark resistivity, post-growth annealing of LTG GaAs at temperatures ~600° C has been found to reduce the defect densities by forming arsenic precipitates and hence increase the dark resistivity [80]. LTG GaAs have been shown to be the most promising candidate for THz generation at ~800 nm excitation wavelength. At telecommunications wavelength, cold Fe-implantion of InGaAs has been demonstrated to generate good THz signals [78].

Pulsed THz radiation can be detected using photoconductive switches [81] and also using the technique of electro-optic sampling [82, 83]. Photoconductive detection can be thought to operate along similar principles to photoconductive generation. A part of the femtosecond beam is time-delayed and focussed on the switch, generating photo-excited carriers. The THz radiation is also focussed onto the switch in the same region, creating transient currents. Thus, the THz field can be detected using a conventional lock-in detection technique to measure the transit current, and by time-delaying the femtosecond beam to sample the THz pulse completely. Obviously, the optical pulse duration must be much smaller than the THz pulse in order to sample the THz pulse correctly and this is the case why < 100 fs laser pulses are used. Also, the photoconductive material should have sufficiently low carrier lifetime to avoid saturation of the detector.

In this thesis, pulsed THz radiation, from photoconductive switches has been used in the well-developed terahertz time-domain spectroscopy (THz TDS) technique to measure spectroscopic signatures of various samples. The technique of

THz TDS along with electro-optic (EO) sampling is discussed in the following section.

1.3.1 Terahertz time-domain spectroscopy

The pulsed generation and detection of THz radiation can be used to obtain spectroscopic signatures of samples using techniques such as terahertz attenuated total reflection (ATR) or time domain spectroscopy. Here, the technique of THz TDS is explained in further details as this has been used further into the thesis. In this technique, a THz pulse is detected in the time domain after reflection from or transmission through the sample. This pulse is compared to a reference pulse (without any sample). Generally, compared with the reference, the signal passing through the sample is reduced in amplitude and delayed slightly in time. The THz pulses are mapped out in the time domain with subpicosecond resolution, and Fourier transformed to obtain the frequency response of the reference and the signal. As it is a coherent detection technique, the electric field amplitude and phase information are readily available, enabling direct analysis of the frequency spectra to obtain spectroscopic information such as the frequency-dependent absorption coefficient and refractive index of the sample, without applying Kramer–Kronig analysis [8].

THz TDS has a major advantage over the well-established Fourier transform infrared spectroscopy as the former can provide both amplitude and phase information and operates in room temperature, but the latter is principally based on intensity detection and requires cryogenically cooled bolometric detection. Also, THz TDS has better signal-to-noise ratio as it is not sensitive to thermal background radiation noise [8]. THz TDS can be performed under normal atmospheric conditions, but as the THz power is small and THz radiation gets strongly absorbed by the water content in the atmosphere, systems are generally purged to remove any water vapour. THz TDS does require expensive femtosecond source to generate broadband THz radiation.

1.3.1.1 Experimental configuration

The experimental configuration used for THz TDS measurements in this work is shown in Figure 1.3. To generate ultrashort femtosecond pulses, a Femtosource Compact titanium-sapphire femtosecond laser was pumped with 5.60 W optical power at 532 nm wavelength using a Spectra Physics Millenia XS diode laser. At a repetition rate of 80 MHz, pulses had a 12 fs pulse width, 800 nm centre wavelength with a full-width-half-maximum (FWHM) span of 109 nm, and 650 mW average output power. Two chirped mirrors were used for dispersion compensation, countering pulse broadening when it travels through the setup, before the beam is split into pump (90%) and probe (10%) beams. The pump beam was time delayed using a mechanical translational stage and then focussed onto a ~400 μm gap bow-tie antenna. The antenna was fabricated on LTG GaAs using optical photolithography and thermal or electron-beam evaporation. The THz radiation emitted from the surface of the emitter was collected [84] to obtain improved bandwidth, using a gold-coated parabolic mirror with a centred hole allowing the focused optical pump beam to pass though (see Figure 1.3). Radiation was collimated, focused through the sample plane, collimated again and focused on a ~150 μm thick gallium phosphide (GaP) crystal using parabolic mirrors. The THz beam was focused collinear with the probe beam on the crystal enabling coherent detection using EO sampling. The probe beam path length was calculated such that the optical pulse arrived around the same time as the THz pulse. The time delay between the two was then varied using a mechanical stage on the pump beam path.

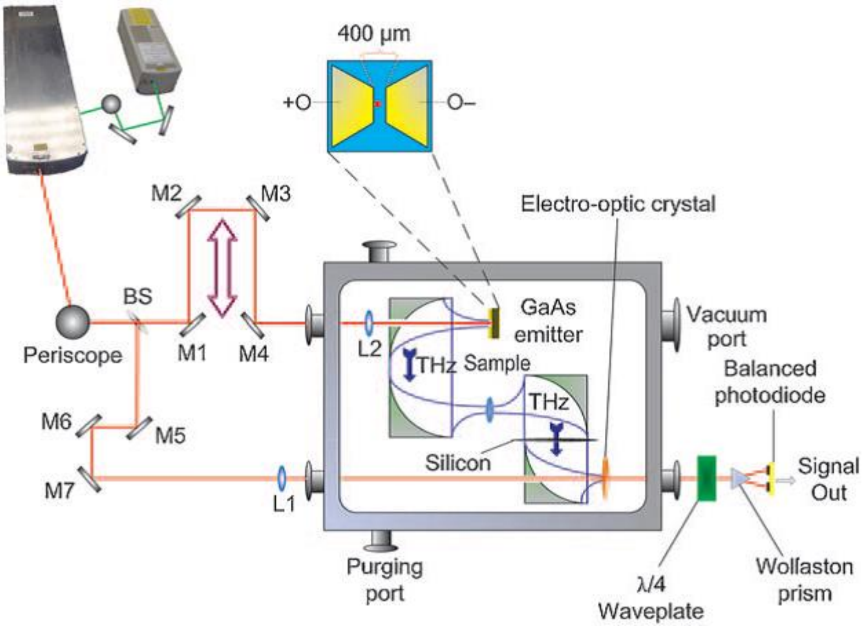

Figure 1.3: Illustration of a broadband terahertz time-domain spectroscopy system. BS, M# and L# represents beam-splitter, mirror and lens respectively. The purple coloured double headed arrow signifies the mechanical translational stage. Image has been taken from [85].

In EO detection, the THz beam causes an instantaneous birefringence as it slightly changes the refractive index of one crystal axis. A linearly polarised probe beam passing through the crystal then becomes slightly elliptically polarised, dependent on the incident THz field strength. The probe beam then passes through a quarter-wave plate, used to balance the photodiode output in the absence of the THz field, before being split into two orthogonal components after passing through a Wollaston Prism. Balanced photodiodes were used to measure the difference of the two components, which is proportional to the instantaneous amplitude of the THz field [86]. The complete time-varying amplitude of the THz pulse is mapped by time-delaying the pump beam, effectively delaying the incident THz pulse on the EO crystal. The signal from the photodiode was measured using lock-in detection technique with a 10 kHz modulation frequency. 10 kHz was chosen as it was the maximum operating frequency of the biasing source. EO sampling is diagrammatically represented in Figure 1.4.

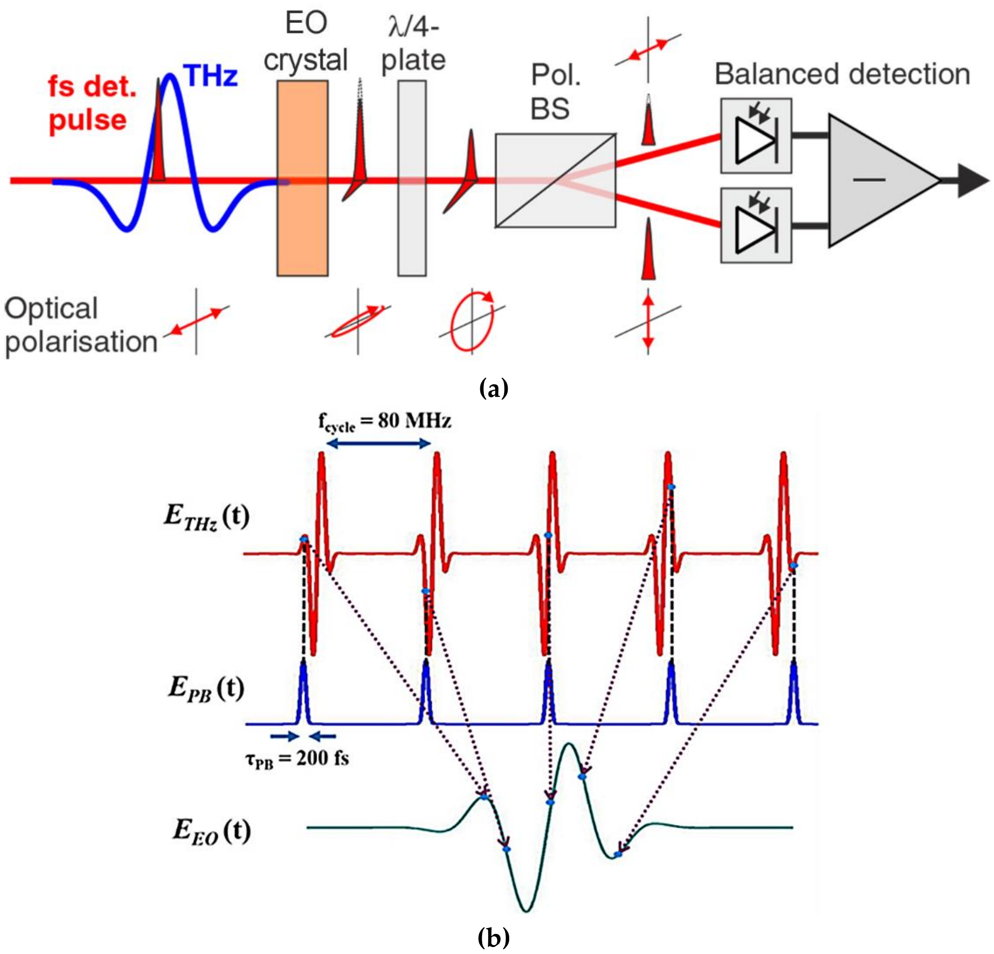

Figure 1.4: (a) Illustration of electro-optic detection of THz radiation. Image reproduced from Ref. [87]. (b) Diagram representing time-delay sampling of the THz electric field with a probe beam. Image taken from Ref. [86]

To avoid any reflected pump beam interacting with the EO crystal (GaP), a high resistivity silicon wafer was placed in the THz beam path, as shown in Figure 1.3. The optical paths from the emitter to the EO crystal were kept under a dry air purged environment to avoid any attenuation due to water absorption. Optical beams travelled in and out of the purge box through silica glass windows.

1.4 Continuous-wave terahertz systems

There has been a growing demand for continuous-wave (CW) tuneable THz sources for applications such as high resolution spectroscopy [88], and as local oscillators in heterodyne receivers for applications based on communications and astronomy [89]. CW THz generation have been demonstrated using backward wave oscillators [90], molecular transition based gas lasers [91, 92], RTDs [93], Schottky diode frequency multipliers [94], THz QCLs [95] and terahertz parametric oscillators [96]. Apart from their own sets of advantages, the disadvantages are combinations of being bulky, expensive, high electrical power consuming, cryogenically cooled and limited tuneability.

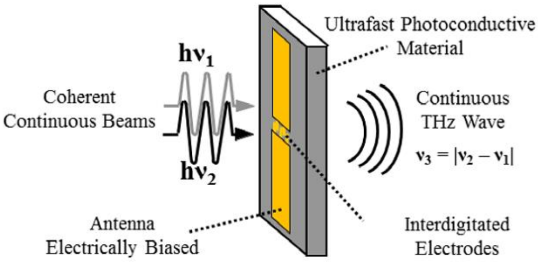

Figure 1.5: Two continuous-wave lasers, set at slightly different frequencies ν_1 and ν_2, are focussed on a photoconductive material with interdigitated electrodes and a biased antenna to generate continuous-wave THz radiation at the difference frequency $\nu_3 = |\nu_1 - \nu_2|$. Image taken from Ref. [78].

An alternative and preferred method of generating narrowband tuneable CW THz radiation is using the concept of photomixing as it is cheap, compact, low power consuming, continuously tuneable with narrow spectral bandwidth, room temperature operational and coherently detectable source [97]. Photomixing is frequency down-conversion from the optical region. Two CW lasers with a frequency difference in the THz range are focussed onto a photoconductive material such as LTG-GaAs, the photoconductance of which is modulated at the difference frequency (beat frequency). The photo-excited carriers accelerated by an applied bias then generate current oscillations at the beat frequency, which are then emitted as CW THz radiation using an antenna structure. Figure 1.5 illustrates diagrammatically CW THz generation using the concept of photomixing.

The major disadvantage of photomixing is the low output power due to poor efficiency of optical-to-electrical conversion, but extensive research is being done to improve its performance [98-101].

CW THz radiation can be incoherently detected using detectors such as a bolometer [102] or coherently detected using another photomixer as a receiver [97]. Photomixing has been considered for industrialisation as it enables a cheap and compact high resolution THz system, compared to pulsed THz approaches [22]. This technique will be further discussed in detail in Chapter 4.

1.5 Terahertz quantum cascade lasers

In conventional semiconductor lasers, radiation is generated by radiative recombination of electrons and holes between the conduction and valence bands, respectively. The laser frequency is dependent directly on the bandgap energy. These kinds of lasers are generally referred to as interband lasers and have been used for visible and near-infrared frequency region. However, due to unavailability of materials with smaller bandgap energies corresponding to emission in the mid-infrared or far-infrared region, utilising conventional methods is not possible [6].

As an alternative approach, in 1971 Kazarinov and Suris proposed the concept of light generation and amplification due to intersubband transitions of electrons within quantised energy levels in a quantum well [103]. This work was proposed shortly after work on superlattices reported by Esaki and Tsu [104]. The concept was only realised over two decades later in 1994 by Faist *et al* [105], who demonstrated the first quantum cascade (QC) laser. The emission wavelength of ~4.2 µm (~71 THz) was in the mid-infrared (MIR) region with peak power more than 8 mW in pulsed mode at 10 K.

QCLs are unipolar electrically pumped semiconductor lasers with photon generation entirely based on electron, i.e. transitions in the conduction band of multiple-quantum well structures. Chains of quantum wells stacked together form a superlattice with minibands of energy levels overlapping the upper and lower lasing energy levels in a quantum well. These minibands helps to achieve population inversion by fast scattering of electrons from the lower lasing level of a quantum well (extractor) to the upper lasing level of the following quantum well (injector). In principal, each electron pumped into the structure emits multiple photons as it travels through the entire '*cascaded*' or '*stepped waterfall-like*' active region.

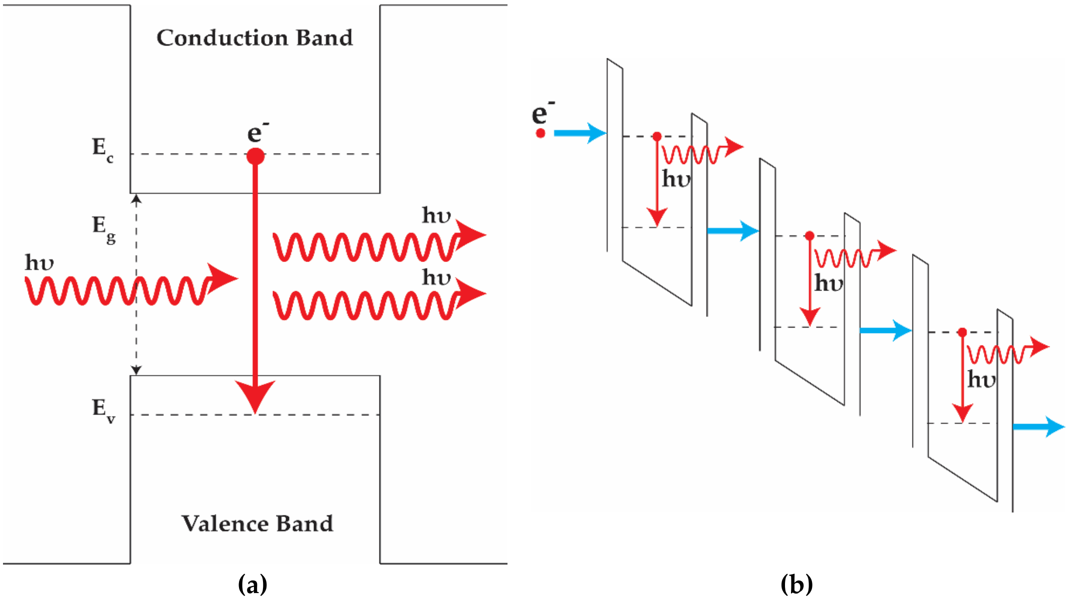

Figure 1.6: Illustration of photon generation using (a) a conventional interband laser and (b) an intersubband cascaded heterostructure.

The major difference between conventional interband lasers and intersubband lasers is that the former is bipolar (electron and holes) and the emission frequency is dependent upon the bandgap of the material whereas the latter is unipolar (electrons only) and the emission frequency can be tailored using the same semiconductor material by changing the quantum well layer thickness. A schematic of photon generation in interband and intersubband lasers is shown in Figure 1.6.

Following the development of the first MIR QCL, continuous-wave operation was soon demonstrated in 1995 [106] and room temperature operation was reported in 1996 [107]. Since then research in this field has been very actively pursued to improve parameters such as the output power, efficiency, and tunability. These developments have been extensively reviewed in Refs. [33, 108, 109].

Designing QCLs to operate below 10 THz was, however, a challenge in a number of ways. Unlike the MIR, where the required photon energies are much higher than the longitudinal optical (LO) phonon energy (36 meV or ~8.7 THz in GaAs), the THz regime is below this energy level (4–20 meV) [2]. Hence a different active region design is required to achieve population inversion and extraction of electrons between the closely spaced energy levels in THz QCLs. Another hurdle was to overcome the increase of free carrier losses in semiconductors which was approximately proportional to the wavelength squared. Finally, the thickness of conventionally used dielectric confinement layers was impractical to grow using MBE owing to the long terahertz wavelength (~100 μm in free space) [6].

Overcoming all these challenges, the first QCL operating at ~4.4 THz was demonstrated in 2002 [63] using an MBE grown GaAs/AlGaAs structure. The active region, shown in Figure 1.7, was based on a chirped superlattice design in a single plasmon waveguide geometry. The laser operated in pulsed mode with a peak output power of ~2 mW at 8 K and maximum operating temperature of 50 K.

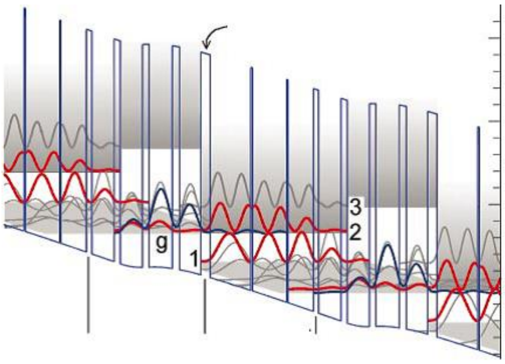

Figure 1.7: Design of the first THz QCL active region based on a chirped superlattice structure. Image taken from Ref. [63]

Soon after the demonstration of first THz QCL which operated in pulsed mode, CW operation of a THz QCL was reported with 410 μW peak power at a 10 K heatsink temperature [110]. Since then efforts have been made to enhance the performance of THz QCLs. Currently THz QCLs have collectively demonstrated a spectral coverage from 1.2 THz [111] to more than 5 THz [112] without the influence of external magnetic fields. Maximum operating temperature of 199.5 K [65] in pulsed mode and 129 K [113] in CW mode has been achieved. The maximum peak powers recorded pulsed and CW mode are >1 W [114] and 138 mW [115], respectively. With an applied magnetic field as high as 31 T, lasing action has been observed using a THz QCL, over a frequency range of 0.68–3.33 THz and a maximum operating temperature of 225 K obtained [116].

Apart from improvements in the GaAs/AlGaAs QCL performance, QCLs at 3.1 THz with a maximum temperature operation of 122 K have been successfully demonstrated using InGaAs/InAlAs on InP substrates [117]. THz QCLs fabricated using GaInAs/GaAsSb lattice matched to InP have been reported up to a 142 K maximum temperature, with a broad spectral coverage of 3.3–4 THz [118]. THz QCL heterostructures based on InGaAs/AlInGaAs have showed operations up to 148 K without magnetic field, and 195 K under 12 T magnetic field [119]. Furthermore, an electroluminescence peak at 4 THz has been measured from an InAs/AlSb quantum cascade structure [120].

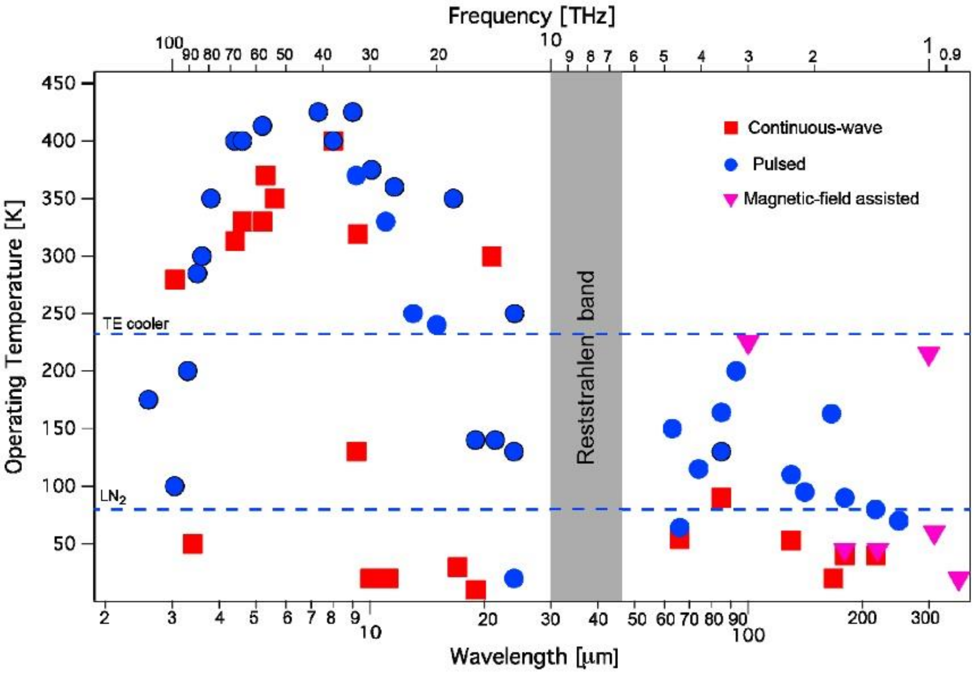

Figure 1.8: Temperature performance of quantum cascade lasers over a range of frequencies from the MIR to THz region. Image taken from Ref. [33]

Amongst various options to generate THz radiation, THz QCLs are one of the most promising candidate as they are compact and generates relatively high THz powers. The drawback are their need for cryogenic operating conditions. As MIR QCLs have been operating at room temperature for some time, they have been used to demonstrate intracavity frequency difference generation in the THz range using a dual colour MIR QCL cavity [121, 122].

Temperature performance as a function of wavelength/frequency of current MIR and THz QCLs is shown in Figure 1.8. Recently, the performance and applications of MIR/THz QCLs have been extensively reviewed in Ref. [33-35].

1.6 Summary

This chapter has presented a general introduction to the THz region of electromagnetic spectrum and its potential applications. Various THz approaches, including broadband THz TDS, narrowband THz photomixing and semiconductor solid state THz QCL have been discussed. These sources were used in this thesis.

Chapter 2 describes in detail, the fabrication of semi-insulating surface plasmon (SISP) terahertz quantum cascade lasers. Characterisation of a fabricated device is explained.

Chapter 3 demonstrates diffuse reflectance imaging with an electrically, frequency-tuneable THz QCL, a potential terahertz spectroscopic technique taking advantage of the high power of THz QCLs. A Kubelka–Munk model is applied to calculate absorption coefficients from the reflectance signal, and results are compared with those from conventional THz TDS.

Chapter 4 presents the fabrication and characterisation of photomixers, an alternative approach to generate THz radiation. They offer wide frequency tunability without cryogenic cooling. The effect of annealing temperature and material resistivity on the bandwidth of photomixers is studied. Also, state-of-the-art photomixers from TOPTICA Photonics are characterised and their bandwidth compared with the fabricated photomixers.

Chapter 5 reports a new technique for CW injection locking of a THz QCL using THz radiation generated from photomixers and locking of a THz QCL is demonstrated.

Chapter 6 concludes the work carried out in this thesis, and discusses possible directions for further investigation and improvement of the work

Chapter 2

Fabrication and characterisation of THz QCLs with a SISP waveguides

2.1 Introduction

The fabrication and characterisation of solid-state devices such as THz QCLs, photoconductive antennas and photomixers were carried out substantially during the course of this degree. The fabrication and characterisation of photomixers will be explained in Chapter 4.

Additionally, a sample was also fabricated for experiments based on coherent three-dimensional imaging using self-mixing in THz QCLs. It consisted of a three-stepped structure, fabricated on a GaAs substrate using a wet chemical etching process, and the top half of the sample was subsequently coated with gold (see Figure 2.1). The work based on this stepped sample has been reported in Refs. [34, 123-126]. During the course of this degree, THz QCLs were also characterised with superconducting detectors made from either NbN or $\mathrm{YBa_2Cu_3O_{7-8}}$ (YBCO) and has been reported in Refs. [127-132]. The transient characteristics of a THz QCL was studied, which included ultrafast detection of nanosecond pulses from a THz QCL, the transient intrapulse response and interpulse heating effects. These works were not the prime objectives of this thesis and hence have not been further mentioned.

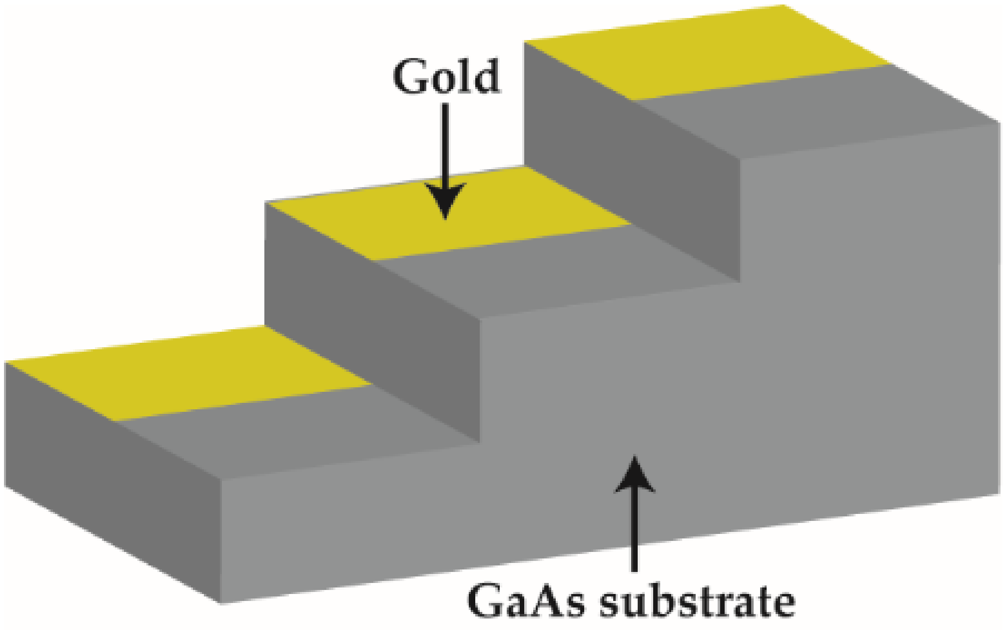

Figure 2.1: Illustration of stepped sample fabricated for self-mixing experiments.

This chapter discusses in detail the fabrication methodology used to process terahertz quantum cascade laser with a semi-insulating surface plasmon (SISP) waveguide. The experimental setup used to characterise the light-current-voltage (LIV) and emission spectra of a standard THz QCL is also described along with the characterisation results from a typical THz QCL device.

2.2 Fabrication of semi-insulating surface plasmon waveguide terahertz quantum cascade laser

Typically, a THz QCL wafer was grown on a semi-insulating (SI) GaAs substrate using molecular beam epitaxy (MBE). A sample with dimensions of 6 mm x 8 mm was then processed into a THz QCL chip. The MBE growth was carried out by Dr Lianhe H. Li.

All of the processing steps were undertaken at the nanotechnology cleanroom facility in the university. An overview of the processing steps is diagrammatically illustrated in Figure 2.2 and can be categorised as:

1. Dicing, cleaning and edge bead removal.
2. Wet chemical etching to define the laser ridge.
3. Bottom contact metallisation and annealing.
4. Top contact metallisation.
5. Over-layer metallisation.
6. Substrate thinning and metallisation.
7. Top contact sintering.
8. Cleaning, mounting and wire bonding.

Details of each stage of the fabrication procedure are explained in the following subsections. The protocol to fabricate THz QCLs with semi-insulating surface plasmon waveguides was provided by Dr Iman Kundu and similar processing techniques have also been described in Refs. [133-135]. Intrinsic details of micro and nanofabrication techniques are beyond the scope of this thesis and can be found in Refs. [136, 137].

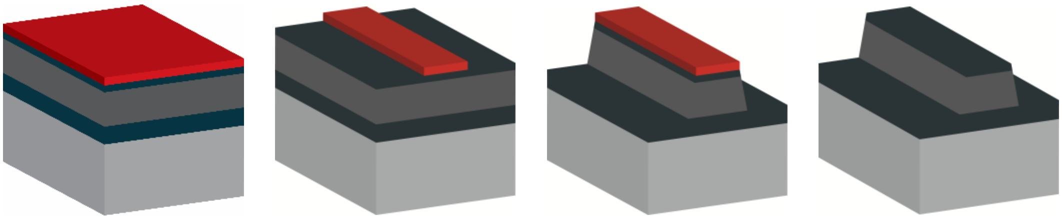

Resist Spin *Photolithography* *Mesa etching* *Laser ridge*

(a) Wet chemical etching to define laser ridge

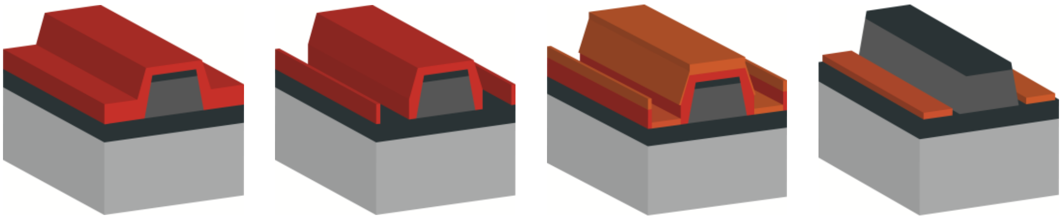

Resist Spin *Photolithography* *AuGeNi deposition* *Lift-off & anneal*

(b) Bottom contact metallisation

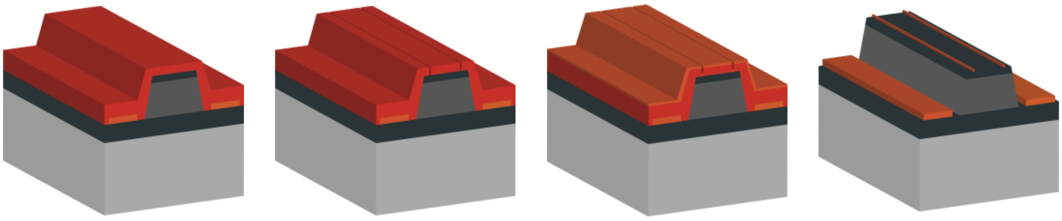

Resist Spin *Photolithography* *AuGeNi deposition* *Lift-off*

(c) Top contact metallisation

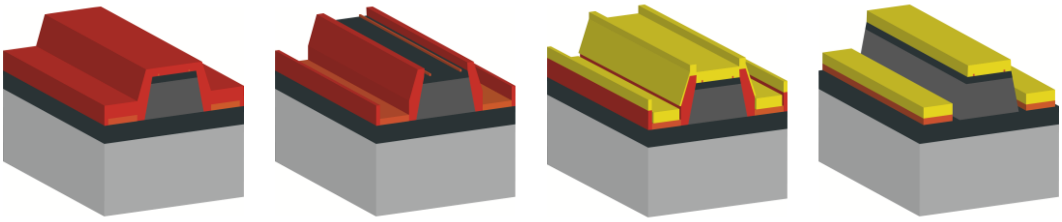

Resist Spin *Photolithography* *Ti/Au deposition* *Lift-off*

(d) Over-layer metallisation

Substrate etching *Backside Ti/Au deposition*

(e) Substrate thinning and metallisation

Figure 2.2: Overview of steps involved in fabrication of THz QCL with a SISP waveguide.

2.2.1 Cleaving, cleaning and edge bead removal

A sample with dimension of 6 × 8 mm was diced from of the MBE grown wafer. This was the optimum dimension as the mask sets used was designed to fabricate three laser ridges (each ~6 mm long) on each sample simultaneously. Images shown (top view) in the following subsections are from one of the fabricated ridges.

Cleaning the sample was the first step before any photolithographic procedure and was done a number of times throughout the fabrication process. The sample was immersed in an acetone based ultrasonic bath with ~10% power for a minute to remove any unwanted contaminants and organic deposits from its surface. It was then rinsed with isopropyl alcohol (IPA) and blow dried using dry N_2 stream. A thorough clean was done by placing the sample in an Emitech K1050X Plasma Asher for five minutes at 85 W.

The cleaned sample was spin coated with a positive photoresist (Shipley Microposit S1813) at 5000 rpm for 30 seconds. This resulted in a typical resist thickness ~1.2 μm [138]. Resist coated sample was soft baked to evaporate any excess solvent, using a hotplate at 115° C for one minute. Spin coating of resist leads to uneven resist build up around the sample edges and its corners. These edge beads could potentially impact the quality of any consequent patterning using optical photolithography technique. Hence, a chrome-on-glass photolithographic mask set was specifically designed to expose the resists around the edges. Using this mask, the sample was exposed with 310 nm UV radiation at 10 $\mathrm{mW/cm^2}$ for 10 seconds and the resist was developed for two minutes in Shipley Microposit MF319. The sample was rinsed with De-ionised (DI) water to inhibit further development and was blow dried using dry N_2 stream.

Generally, in a photolithographic step the sample was spin coated with resist, exposed with UV under a suitable mask for three seconds, developed in MF319 and rinsed with DI water. At the end of each fabrication step sample was cleaned with acetone and IPA and blow dried with dry N_2 stream unless otherwise stated. A longer duration of UV exposure for edge bead resist was necessary because of the thick resist at the edges.

2.2.2 Wet chemical etching to define laser ridge

The active region of the THz QCL was sandwiched between two highly doped n^+ layers. An etching process is necessary in order to expose the highly n^+ doped layer beneath the active region. The n^+ layer on the surface of the sample (top contact) and the post-etch exposed n^+ layer (bottom contact) would form the electrical contacts of the active region with the outside world. This section describes the process used to etch the mesa and to form a laser ridge, as shown in Figure 2.2 (a).

After edge bead removal, the sample was exposed with UV radiation under a chrome mask, developed for 90 seconds, rinsed with DI water and blow dried to define the ridge across the sample surface. Figure 2.3 (a) shows an optical microscopy image of resist (dark brown) patterned on the sample surface to define the laser ridge.

Wet chemical etching technique was used to etch the mesa and define the laser ridge. A solution of H_2SO_4, H_2O_2 and H_2O mixed in the ratio of 1:8:40 by volume was used as an etchant [139]. As the prepared etchant was exothermic in nature, it was allowed to cool down for ~15 minutes to room temperature. The sample was carefully etched through the active region, exposing the bottom contacts. The etch depth was defined by the active region thickness, typically in the range of~12-15 μm. An excessive etching would result in the complete removal of the bottom contact layer (500–600 nm), preventing proper electrical contact and would render the sample useless. In order to ensure a correct etching depth was reached, the etch depth (ridge height including the resist thickness) was measured using an Alpha step surface profiler during the etching process. After etching, resist was stripped off using acetone and the sample was cleaned. Figure 2.3 (b) shows a ridge defined on the sample after etching.

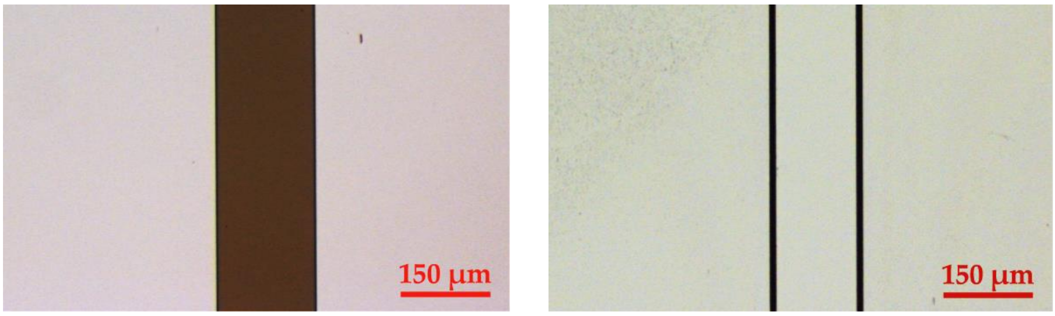

(a) **(b)**

Figure 2.3: Microscope image of sample after (a) photolithography and (b) wet chemical etching to define the laser ridge.

2.2.3 Bottom contact metallisation and annealing

This section describes the processes followed to form an electrical connection to the buried contact layer under the active region of the device and is illustrated in Figure 2.2 (b). Positive resist was spun, pre-baked at 90° C and exposed with UV radiation under a mask suitable to pattern the bottom contact layer region. Generally, it is essential to have an undercut profile in the developed resist for a good lift-off of the deposited metals. In order to achieve this, the UV exposed sample was soaked in chlorobenzene for 2 minutes, blow-dried, developed for 70 second, rinsed and blow-dried. Chlorobenzene soak results in a differential rate of development of the exposed resist, creating an overhang feature [140]. The sample was subsequently cleaned in an oxygen plasma asher for 70 seconds at 25 W before loading it inside a thermal evaporator for metal deposition. Figure 2.4 (a) shows a sample prepared for metallisation of the bottom contact, after development of the photoresist.

An eutectic alloy of AuGeNi was deposited to a thickness of ~250–300 nm at an evaporation rate of ~2 Å/sec under vacuum ($\sim 2 \times 10^{-6}$ mbar). AuGeNi alloy is commonly used to form a low resistivity ohmic contact for GaAs/AlGaAs heterostructures and *n*-type GaAs [141, 142]. The metal evaporated sample was immersed in acetone for lift-off. This dissolved the unexposed (remaining) photoresist from the sample, effectively removing the unwanted metals from the sample. The sample was then cleaned, and blow-dried. Figure 2.4 (b) shows metallised bottom contacts on both sides of the laser ridge.

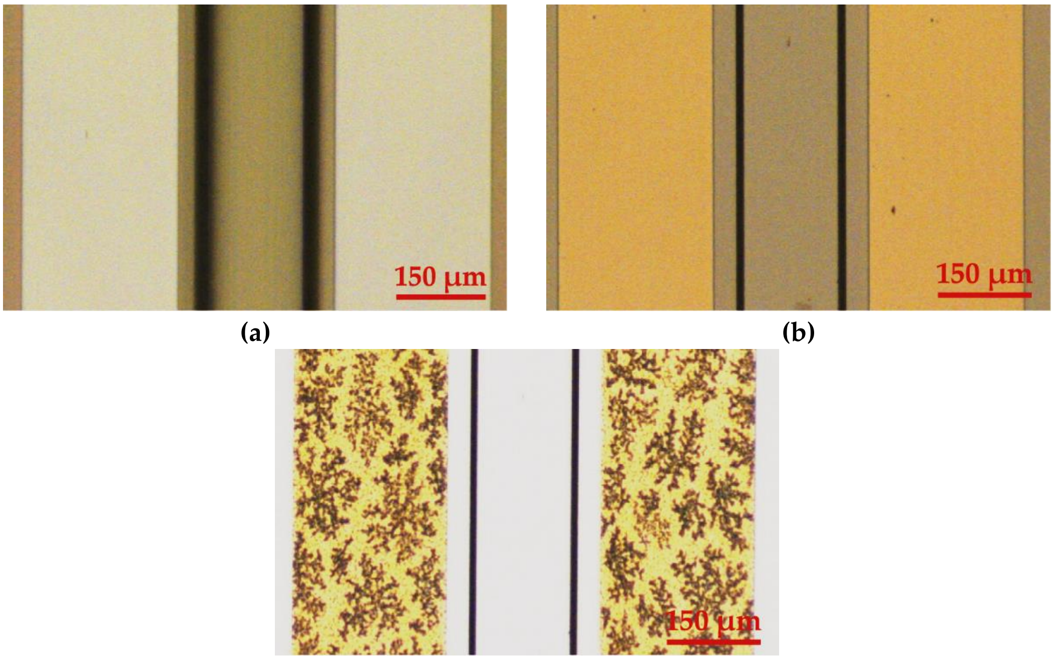

(a) **(b)**

(c)

Figure 2.4: Microscope image after (a) photolithography, (b) bottom contact metallisation (AuGeNi) and (c) annealing of the device.

The sample was annealed at 430° C for one minute using an AnnealSys rapid thermal annealer. Annealing of the deposited alloy was essential to decreases contact resistivity [142, 143] to as low as ~$10^{-6}\ \Omega/\mathrm{cm}^2$. Annealing at such temperatures allows Ge atoms to diffuse into the underlying GaAs and increasing its effective doping concentration [141, 144, 145]. Figure 2.4 (c) shows a microscope image of a sample after annealing. The change in metallised bottom contact appearance is evident due to the effects of annealing.

To check the quality of the electrical contact, the resistance between the bottom contacts was measured, using a multimeter and a probe station. The resistance between the contacts typically ranges between 5–10 Ω. A higher resistance could potentially arise due to fabrication issues such as an over-etched mesa or poor metallisation of bottom contacts, and could possibly result in poor thermal performance of the device. As such, it was not advisable to continue fabrication of such a sample.

2.2.4 Top contact metallisation

This section describes the deposition of thin metallic ohmic contact rails on top of the laser ridge to serve as the second electrical terminal on top of the laser ridge (top contact) and is illustrated in Figure 2.2 (c). To reduce waveguide losses, only two 10 μm-wide rails of ohmic contact was metallised along the length of the ridge on top of the laser [146]. However, annealing of this ohmic contact, similar to the annealing of the bottom contact, was not carried out after deposition to avoid diffusion of Ge atoms into the active region of the device.

The fabrication steps used to deposit the top electrical contact is similar to those used to form the bottom contact metallisation, as mentioned in the previous section and is briefly described here. After annealing of the bottom contact, the sample was cleaned, spin coated with photoresist, pre-baked, exposed to UV radiation under a suitable mask for top contact lithography, soaked in chlorobenzene, developed, rinsed and blow-dried. Figure 2.5 (a) shows a microscope image of the sample with two exposed thin rails on top of the laser ridge formed after the development of the resist. Further processing steps included cleaning of the exposed sample surface in oxygen plasma asher, thermal evaporation of 100–130 nm-thick AuGeNi alloy and lift-off in acetone. Figure 2.5 (b) shows a microscope image of a sample with metallised top contact.

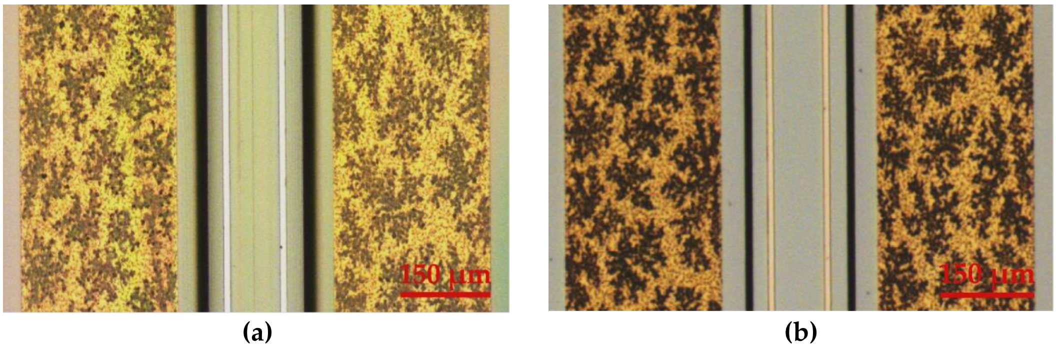

(a) (b)

Figure 2.5: Microscope image of sample after (a) photolithography and (b) top contact metallisation (AuGeNi) on top of the laser ridge.

2.2.5 Over-layer metallisation

This section describes the deposition of a thin layer of Ti/Au on top of the laser ridge and the bottom contacts, and is illustrated in Figure 2.2 (d). The deposition was necessary to confine the THz radiation inside the laser cavity and to facilitate wire bonding of the contacts as explained later in Section 2.2.8. Cr or Ti has been widely used as an adhesive layer for Au.

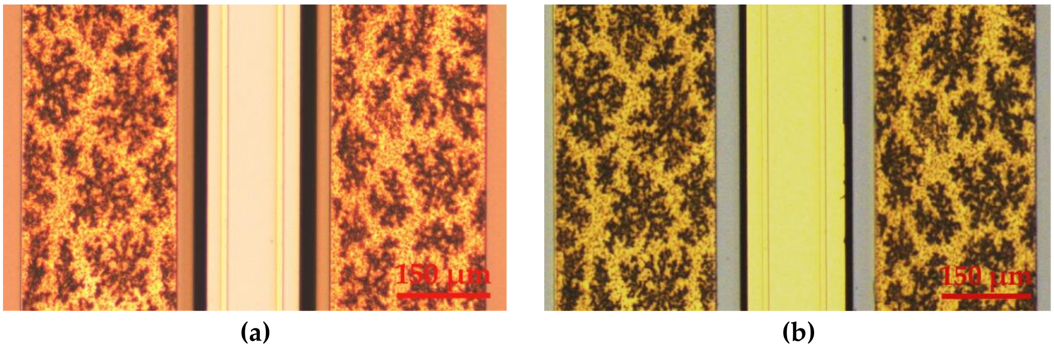

(a) (b)

Figure 2.6: Microscope image of the sample after (a) photolithography and (b) over-layer metal deposition over the bottom contacts and laser ridge.

The fabrication steps followed during this stage were similar to both the bottom and the top contact metallisation, as mentioned previously. Figure 2.6 (a) shows a microscope image of a sample with exposed bottom contacts and the top of the ridge after photoresist development. Similarly, Figure 2.6 (b) shows a microscope image of a sample after thermal evaporation of Ti/Au (20 nm/200 nm) and lift-off.

2.2.6 Substrate thinning and metallisation

This section describes the etching of the substrate and metallisation of the backside with Ti/Au and is illustrated in Figure 2.2 (e). Reducing the SI-GaAs substrate thickness allows better heat dissipation and hence improves thermal performance of the device [63]. Metallisation of the backside allows improved adhesion to the indium on copper block during mounting, mentioned later in Section 2.2.8.

The sample was placed with the laser ridge side immersed in molten wax on a glass slide. It was important for the wax to cover and protect the ridges while etching the 500 μm substrate. The sample stuck to the glass slide was immersed in an etchant solution of H_2SO_4, H_2O_2 and H_2O mixed in 1:8:1 proportion by volume, with a much higher etching rate than the solution prepared to define the laser ridge (see Section 2.2.2). The etchant was heated at 50° C and an etch rate of approximately 20 μm/min was measured. A Tesatronic micrometer was used to regularly monitor the etch depth. Approximately 300 μm of the substrate was etched. The sample was then rinsed and blow-dried to stop any further etching. The sample on glass slide was then heated to carefully remove the chip from the molten wax. The sample was then immersed in trichloroethylene to remove any residual wax, cleaned in acetone and IPA and blow-dried.

After thinning of the substrate, the sample was very fragile to handle and extra care was taken in all subsequent processing steps. The sample was cleaned in oxygen plasma asher for 70 seconds at 25 W power. Thermal deposition of Ti/Au (20 nm/150 nm) was done on the backside of the sample.

2.2.7 Top contact sintering

The sample was then sintered at 270° C for four minutes in a rapid thermal annealer. A similar soft annealing, especially for the top contact, has also been reported in Ref. [110]. Sintering at such temperature prevents unwanted penetration of Ge atoms into the active region. Although this step could have been performed before over-layer metallisation, performing it at this point has been reported to improve overall adhesion of deposited metals [135].

At this point, the laser ridge was ready to be cleaved into laser ridges of the desired length, packaged onto a copper block and wire bonded for electrical connections.

2.2.8 Cleaving, mounting and wire bonding

As mentioned earlier, each fabricated sample had three sets of laser ridges (each ~6 mm long) processed on the same chip. The ridges were separated by scribing with a JFP S-100 scriber and manually applying force to cleave through the scribed region. Each laser ridge could then be precisely scribed to a desired Fabry–Pérot cavity length by using the same scriber. Scribed ridges were then carefully cleaved to obtain a mirror–like facet on either side of the device. Facets were inspected under an optical microscope for any cracks or visible damage, as these could potentially increase mirror losses. Alternatively, scribing was also performed manually using a scalpel knife by gently scratching the edge of the sample in the direction of cleaving. This technique was impractical to produce devices of precise cavity length and had low yield due to manual handling and the resulting damage.

Two scribed laser ridges were packaged on a copper block for characterisation. A copper block with a single polished side was cleaned using an ultrasonic bath in acetone and IPA. The polished surface was subsequently coated with thermally evaporated Ti/Au (20 nm/150 nm). Gold-coated ceramic pads were glued into the copper block using Ge and would serve as the physical terminals of the mounted laser after wire bonding.

Indium foil was melted on the gold-coated surface of the Cu block at a temperature of ~145° C. The temperature was subsequently reduced to 130° C, below the melting point of indium. Each of the two laser ridges were then carefully position and pinned down on the indium foil. The temperature of the hotplate was then increased above the melting point of indium. The indium improved the adhesion of the substrate with the copper block and consequently improved the thermal contact between device substrate and copper block. Ridges and their respective bottom contacts were then wire-bonded to the ceramic pads using a Kulicke & Soffa 4524 Ball Bonder at a reduced heatsink temperature of 80–100° C.

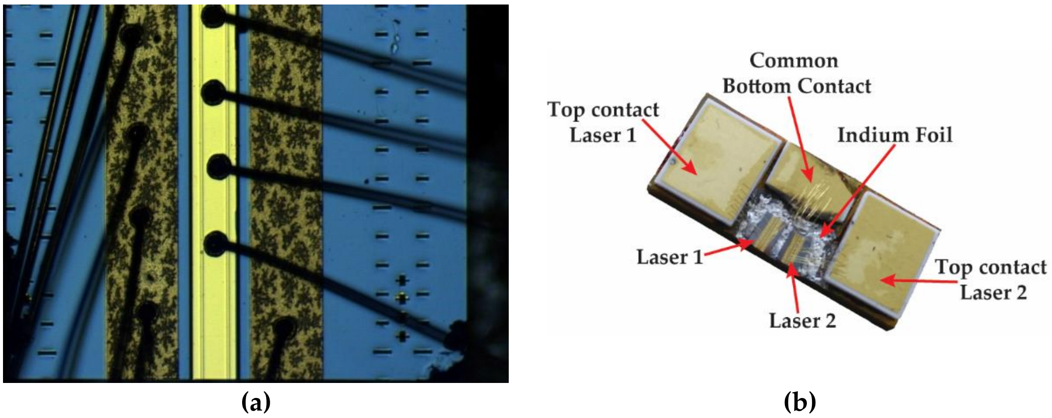

(a) **(b)**

Figure 2.7: (a) Microscopy image of a wire-bonded device. (b) Optical image of two devices packaged on a copper block.

Figure 2.7 (a) shows a microscope image of wire bonded laser ridge and its bottom contact. Figure 2.7 (b) shows a diagrammatic representation of a completely packaged copper block along with two wire-bonded laser ridges and ceramic pads. The packaged devices were subsequently characterised, as discussed next.

2.3 Characterisation of THz QCLs with a SISP waveguide

The power-current-voltage (LIV) characteristics and spectral emission of THz QCLs were characterised post-fabrication. A detailed explanation of experimental setup and results from an exemplar device fabricated from a wafer labelled L-786 are discussed in the following sections.

2.3.1 Experimental configuration

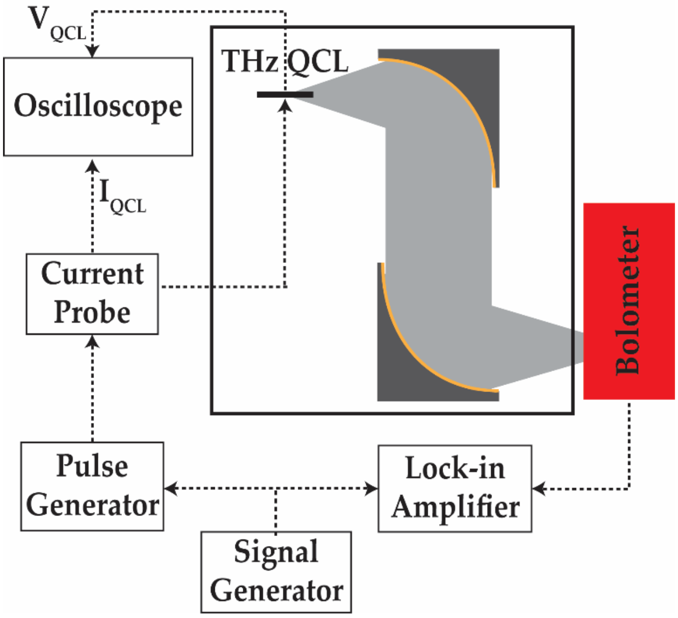

Figure 2.8: Schematic of the LIV characterisation setup of a standard THz QCL.

The experimental configuration for characterising the LIV relations of a THz QCL is diagrammatically represented in Figure 2.8. The packaged device(s) was placed on the cold finger of a Janis ST-100 continuous flow cryostat. The cryostat itself was mounted on a XYZ manual translation stage to precisely control the device position with respect to other optical components, and was pumped down to a vacuum pressure of ~8×10^{-6} mbar using a turbo vacuum pump, and subsequently cooled using liquid helium. The radiation from the laser traversed through the polyethylene window of the cryostat and was collected, collimated and focussed onto a He-cooled bolometer with the help of two off-axis gold-coated parabolic mirrors. The environment was purged with N_2 to reduce the effect of water vapour absorption of the emitted THz radiation. The absolute power of the device was measured using a pre-calibrated Thomas Keating Absolute Terahertz Power Meter.

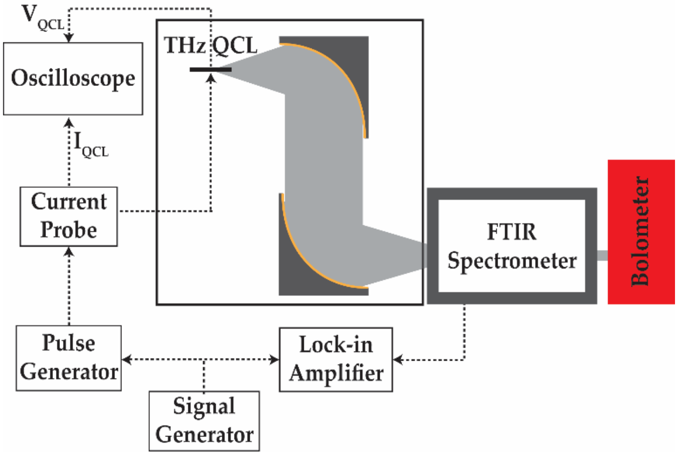

Figure 2.9: Schematic of the experimental setup used for spectral characterisation of a standard THz QCL.

The experimental configuration for characterising the spectral response is diagrammatically represented in Figure 2.9. Two off-axis parabolic mirrors were used to collect and direct the radiation inside a Bruker Optics IFS66/V Fourier transform infrared (FTIR) spectrometer (7.5 GHz resolution bandwidth). Bolometric detection was used to record the interference signal from the spectrometer and also align the laser for better signal-to-noise ratio.

The THz QCL was biased using an Agilent 8114A High Power Pulse Generator, with a 10 kHz pulse train, maximum operational frequency of the generator, at 2% duty cycle and this signal was modulated for lock-in detection at 167 Hz (30 Hz) to match the bolometer's (absolute power meter) peak responsivity for better signal sensitivity. The optimised modulation frequency for bolometer and absolute power meter was provided by their respective manufacturers. An inductive loop current probe with 1:1 current-to-voltage representation was used to measure the output current from the pulse generator feeding the device. The output of the loop was terminated with a 50 Ω load on one channel of an oscilloscope to record the current through the device. The heatsink temperature was controlled and monitored through a temperature controller. A semi-automated measurement environment was created using a LabVIEW program, courtesy of Dr A. Valavanis. For spectral characterisation, the output of the bolometer was connected to the FTIR spectrometer and a computer software package was used to calculate the spectra.

2.3.2 Results

Characterisation results from a 2.54 mm-long, 12 μm-high and 150 μm-wide THz QCL with a bound-to-continuum active region design (wafer L-786) has been presented in this section. LIV characterisation was carried out in pulsed mode at a range of heatsink temperatures from 4–60 K and is shown in Figure 2.10 (a). Peak emission was measured to be 0.18 mW with the absolute power meter at a heatsink temperature of 4K. The maximum operating temperature was observed to be 72.5 K beyond which no lasing was observed.

Spectral characterisation of the device was performed with a range of applied biases from 3.50–5.50 V at a heatsink temperature of ~4K. The spectra obtained have been stacked together in Figure 2.10 (b). A multimode emission with a Fabry–Pérot longitudinal mode spacing of ~17.8 GHz centred at 2.81 THz was observed. Emission spectra with approximately 8–9 Fabry–Pérot modes were observed at higher electrical bias.

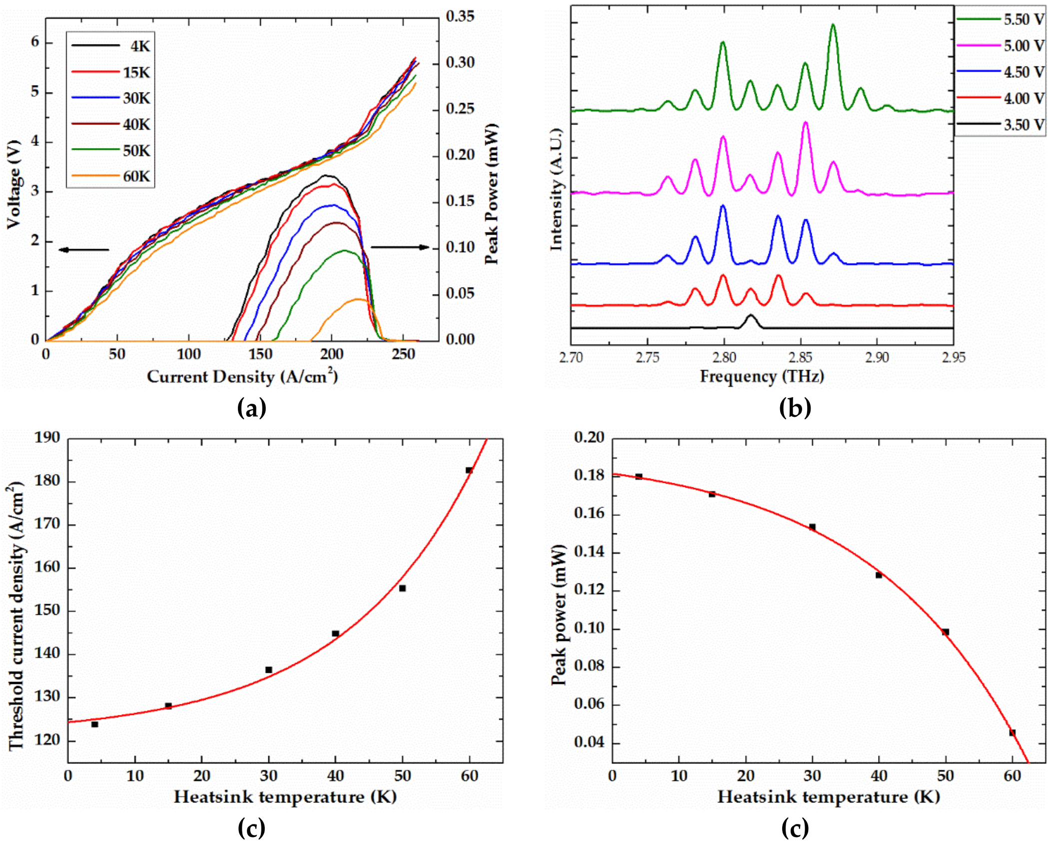

Figure 2.10: (a) LIV from a fabricated THz QCL (wafer L-786) at various heatsink temperatures. (b) Spectral emission at a range of applied drive biases at a heatsink temperature of 4 K. (c) Threshold current density and (d) peak power as a function of heatsink temperature (black dots) with exponential and Boltzman fit (red line) respectively.

LIV characterisation data was analysed further and the threshold current density is plotted as a function of heatsink temperature [Figure 2.10 (c)]. The increase of threshold current density agrees well with an exponential fit (red solid line) and this result is in agreement with that observed in other quantum cascade lasers and other laser types as reported in Ref. [109]. The exponential relationship can be expressed in a general form as $J_{th}(T) = J_0 \exp\left(\frac{T}{T_0}\right) + J_1$, where J_0 and J_1 are the constants, J_{th}, T_0 and T are the threshold current density, characteristic temperature and absolute temperature, respectively. For this particular device, T_0 obtained from the exponential fit was 20 ± 2.7 K. This characteristic temperature is a measure of temperature sensitivity of a device. A higher characteristics temperature implies improved temperature performance of the device [147]. Typically, characteristic temperature values vary from 100–200 K for MIR QCLs and is typically below 100 K for other semiconductor laser types [109]. The lower value of T_0 in THz QCLs can be attributed to the thermal backfilling and thermally activated LO phonon scattering [148]. Thermal backfilling refers to backfilling of electrons in lower lasing state due to increase in their thermal excitation or "reabsorption of non-equilibrium LO-phonons" [2]. Thermally activated LO phonon scattering refers to the process when electrons in the upper lasing state gains enough energy to depopulate by emission of non-radiative phonon and reach the lower lasing state [2]. Both processes causes reduction in population inversion and hence performance of the laser. T_0 in THz QCLs have been reported as high as 69.9 K [148].

Finally, the estimated peak power was plotted as a function of the heatsink temperature as shown in Figure 2.10 (d). It agrees well with a Boltzmann fit (red line) and is consistent with previously reported results in Refs. [133, 149].

2.4 Summary

In this chapter, the processing steps to fabricate terahertz quantum cascade laser with a semi-insulating surface plasmon waveguide was described in detail. The processing steps involved etching, photolithography, metallisation, annealing, manual cleaving and wire bonding.

The characterisation apparatus to measure light-current-voltage relationships and emission spectrum was explained. Results obtained from a semi-insulating surface plasmon waveguide THz QCL fabricated on a home-grown wafer were discussed.

THz QCLs fabricated following a similar methodology as discussed in this chapter were used in a range of applications including diffuse reflectance spectroscopy and continuous-wave injection locking, which are discussed in Chapter 3 and Chapter 5 respectively.

Chapter 3

Diffuse reflectance spectroscopy at terahertz frequencies

3.1 Background

Under ideal conditions, a perfectly non-absorbing medium would reflect an incident THz beam in two limiting ways depending on its surface. A perfectly smooth surface gives rise to mirror-like specular reflections; as stated in Fresnel's law of reflection, the angle of incidence is equal to the angle of reflection. A completely scattering (rough) surface, i.e. a Lambertian surface, would uniformly reflect light in all direction; this is known as diffuse reflection. As real-world objects are far from ideal, incident light is not either specularly or diffusely reflected, but a portion of it is absorbed or is transmitted through the medium. These material-specific transmission and reflection properties can be utilised to image objects, and acquire spectroscopic signatures.

Demonstration of terahertz imaging can be traced way back to 1960s in the field of astronomy [26]. Transmission imaging at these frequencies have been reported as early as 1970s [150, 151]. Various terahertz imaging systems have been reported using either a transmission [9, 11, 14, 16, 32, 152-157] or reflection geometry [8, 158-165]. In transmission mode, a THz beam is focused at the sample plane and detected using either near-field [166, 167] or far-field [8, 11, 157] imaging configurations. This allows access to material specific parameters such as absorption coefficients and refractive index over a broad spectrum of frequencies, as large as 100 THz [168].

Most of the experimental configurations have used the concept of terahertz time-domain spectroscopy (THz TDS), which has been described in Section 1.3.1. These terahertz pulsed imaging (TPI) systems rely on expensive near-infrared/visible extremely short pulse (~fs) laser, and an extremely low THz power (~μW) is generated from emitters fabricated on photoconductive semiconductor substrates [44] with a maximum frequency resolution of ~5 GHz [34]. Hence only very thin samples, typically $\lesssim 1$ mm, with relatively low absorption at THz frequencies can be used for imaging purposes to prevent complete absorption of the radiation [162, 165].

For real-world applications a reflection geometry is more desirable as spectroscopic imaging of bulky and highly absorbing samples is possible even with low THz incident power [8]. Under a reflection geometry, the interaction of incident radiation with a rough surface can include directional specular reflection, non-directional diffuse Fresnel reflection [160] and absorption of radiation [162].

Diffuse reflections generally provide a more practically useful way of imaging objects than specular. Indeed, most of the images perceived by the eye are formed due to diffuse reflections from rough surfaces, with the exceptions such as smooth or polished metals, shiny objects, glass, and luminous objects. A few of the very many potential applications of diffuse reflectance are detection of cancerous tissues [169] and explosives [160], characterisation of powdered materials [162, 165], in the field of pharmaceuticals [43], dentistry [170], biomedical [171], acoustics [172], astronomy [173], geology [174], dark field microscopy [175] and Diffuse Reflectance Infrared Fourier Transform Spectroscopy (DRIFTS) [176].

Diffuse Reflection Imaging (DRI) techniques sense scattered radiation from the surface of an object and have their own set of advantages over transmission or specular reflection imaging. Diffuse reflections depends on the scattering cross-section and bulk-absorption properties of rough surfaces or powdered samples [177] and can provide more detailed signatures of the sample such as particle size, packing density, distribution of particle sizes and shape as compared to specular reflection. Unlike transmission or specular reflection geometries, DRI allows real-life stand-off imaging of objects where precise alignment of collection optics is not possible [160] in applications such as security imaging, imaging of surfaces of planets using satellites [173], identification of mineral composition of soil [178], and segregation of pharmaceutical particles [179]. Objects concealed in smooth surfaced packaging materials or those having strong sub-surface scattering such as powders, would be challenging to identify using specular reflection imaging techniques. As the collection optics of DRI are aligned away from the specular reflection path, reflections from smooth packaging would not contribute in the measurements, enabling imaging of concealed items [162]. The intensity of diffuse reflections depends on the particle size with respect the incident radiation wavelength and also the complex refractive index of the material, which determines the amount of radiation absorbed while traversing through the particles [162].

DRI at terahertz frequencies has been previously reported using a THz TDS system [160]. Phase information of the signal was not available using this technique due to the difference in the radiation scattering position of the sample and the reference. Absorbance values were calculated for an explosive compound commonly known as RDX (hexahydro-1,3,5-trinitro-1,3,5,-triazine) using a Kramers–Kronig transformation. These results were in good agreement with the absorption coefficient obtained from conventional THz TDS in a transmission geometry. DRI was also performed with RDX concealed in materials including paper, polyethylene, leather and polyester, and showed an acceptable match in spectral signatures of RDX in each case.

As diffusely reflected signal amplitudes are very low, high intensity sources such as THz QCLs would be ideal for DRI. QCLs have been reported previously as sources for imaging in transmission geometries [180, 181] because of their high emission powers and very narrow linewidths. They are also a good alternative source for DRI and have been used for analysis of powdered samples at a single THz frequency [162, 165, 182].

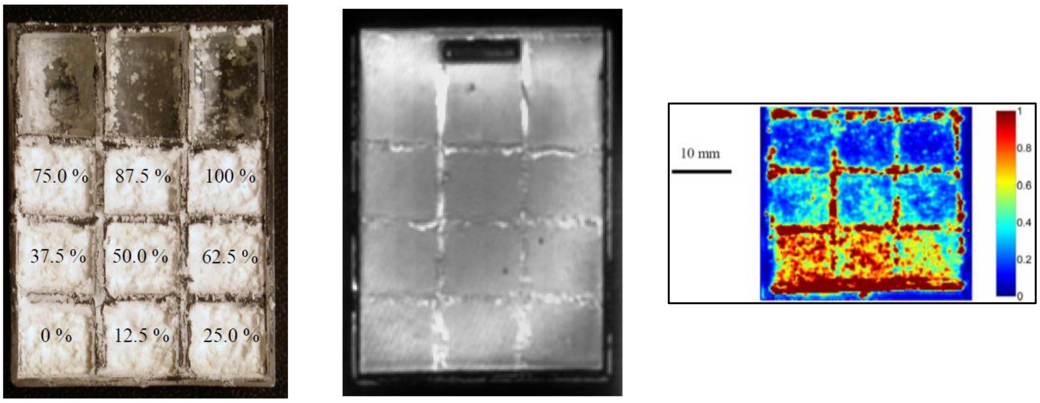

(a) **(b)** **(c)**

Figure 3.1: (a) Optical image of admixtures of polymethyl methacrylate (PMMA) and polystyrene in a polystyrene sample holder without any lid. PMMA mass-concentration has been labelled. (b) Specular and (c) diffuse reflection images of sample with lid on. Image taken from [34, 162].

Diffuse reflection imaging of various concentration (wt%) of PMMA diluted with weakly absorbing powdered polystyrene was performed at 2.8 THz. Figure 3.1 shows (a) optical image of the content (without lid), (b) specular THz (with lid on) and (c) diffuse reflection images of samples in a polystyrene sample holder. Diffuse reflection imaging was able to reveal the concealed powders, whereas the specular image comprised predominately of specular reflection of the incident beam off the polystyrene lid on the sample holder. Varied diffuse reflectance intensities were observed with respect to sample concentration, as seen in Figure 3.1 (c). This work [162] provided the first demonstration of a calculation of absorption coefficient from diffuse reflectance using THz QCL.

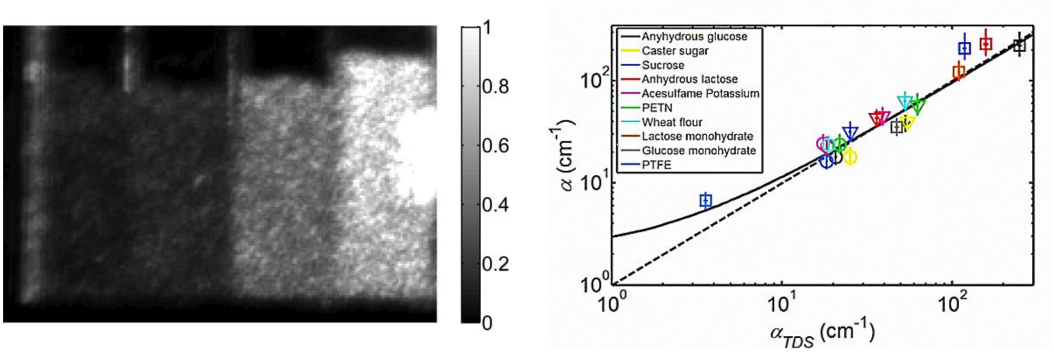

(a) **(b)**

Figure 3.2: (a) Diffuse reflection image at 2.8 THz of 100% purity powdered sample (from left: sucrose, lactose monohydrate, glucose monohydrate and polyethylene) in a polystyrene sample holder. (b) Absorption coefficients α inferred from quasi-crystalline approximation plotted against Beer–Lambert absorption coefficient α_{TDS} obtained from THz TDS measurements for number of different samples. 100% purity samples have been marked with squares, 40% and 15% diluted samples in triangles and circles respectively. Samples were diluted with polyethylene powder. The dashed line represents the identity line. The solid line represents a line of best fit. Images taken from [165].

Another work reported DRI of a range of powdered materials at a single THz QCL frequency, and the absorption coefficients of the samples were determined using a quasi-crystalline approximation (QCA) in a T-matrix formation, using an assumed Percus–Yevick pair distribution of particles [165]. Figure 3.2 (a) shows a diffuse image at 2.8 THz of samples in a polystyrene container (from left: sucrose, lactose monohydrate, glucose monohydrate and polyethylene). A plot of absorption coefficients inferred from the QCA versus those obtained from THz TDS for a number of different samples is shown in Figure 3.2 (b). The calculated absorption coefficient is in a good agreement with the absorption coefficient obtained from THz TDS over a wide range of effective absorption coefficient.

This chapter discusses the optical and electronic configuration for DRI measurements using an electrically tunable multi-frequency THz QCL, including the characterisation of the source, the THz spot-size, and the signal-to-noise ratio (SNR) of the system. Powdered samples packed in plastic cuvettes with strong specular reflection are imaged at four different THz QCL emission frequencies. The absorption coefficient is extracted using simplistic models such as an effective-optical-path-length and the Kubelka–Munk theory. Inferred absorption coefficients are then compared with the Beer–Lambert absorption coefficient obtained using more established THz TDS measurements.

3.2 Experimental configuration

The THz source used in this work was a THz QCL with a heterogeneous active region, as already described in Ref. [183]. The active region was carefully engineered to allow tuning of the lasing frequency by changing the applied electric field and was based on three-well resonant-phonon depopulation design as mentioned in Ref. [184]. Molecular beam epitaxy (MBE) was used to grow the heterogeneous structure. The growth rate of Ga was ramped in a periodic manner over 23 modules each with 10 repeated periods to form the active region. The wafer was then fabricated into a single-metal surface-plasmon waveguide [185] with ridge dimensions of ~1.5 mm long and ~140 μm wide. The device was packaged on a Cu block and mounted on the cold finger of a closed cycle pulse-tube helium refrigerator (CRYOMECH PT403-2440320). The emission window was made of polyethylene. The cryostat was pumped with a turbo vacuum pump below 1×10^{-5} mbar before turning on the cryo-cooler.

The device was cryogenically cooled to ~6 K, monitored on a temperature controller connected to the cold-finger, and biased using an Agilent 8114A pulse generator and a current doubling transformer, with a 10 kHz pulse train at 2% duty cycle. The detector used was a helium cooled silicon bolometer. The THz QCL bias was modulated using a function generator for lock-in detection at a frequency of 167 Hz, which was chosen to match the bolometer's peak responsivity for better detection sensitivity.

The schematic diagram of the experimental apparatus, with its optical path and electrical connections, is shown in Figure 3.3. A similar experimental configuration has been reported elsewhere [162, 165]. The incident optics (M_1, M_2) collected, collimated and focused the diverging radiation from the QCL onto the sample plane at an incident angle of 30° using two gold plated parabolic reflectors. The first parabolic reflector (M_1 in Figure 3.3) had a 3-inch diameter, 90°off-axis with focal length to diameter ratio of *f*/1.7, and the second parabolic reflector (M_2 in Figure 3.3) had a focal length of 33 cm and *f*/4.3. A 2-inch-diameter, 90° off-axis f/2 parabolic reflector (M_3 in Figure 3.3) was placed normally to the sample plane for the purpose of collecting diffusely scattered and non-directional reflected radiation. Collimated radiation was reflected using a planar gold-coated mirror (M_4 in Figure 3.3) onto a final 90° off-axis parabolic reflector (M5 in Figure 3.3) and focused into the helium-cooled silicon bolometer. The off-axis alignment of the collection optics ensured that no contribution of the specular reflected radiation coupled into the detector. The total optical path length between sample and detector was ~30 cm.

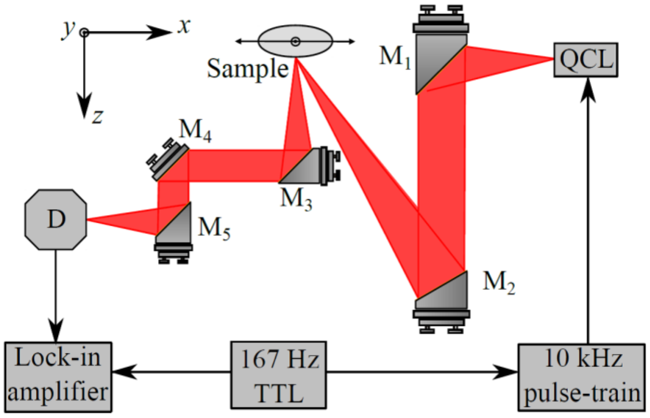

Figure 3.3: Schematic diagram of diffuse reflectance imaging setup. The detector marked with 'D' was a helium-cooled silicon bolometer. Image courtesy of Dr A. Valavanis and also presented in Ref. [186, 187].

The emission frequency of the THz QCL was determined as a function of drive current using a Fourier-transform infrared (FTIR) spectrometer as discussed in Section 2.3. A discrete blueshift in peak emission frequency was observed with increase in drive current as shown in Figure 3.4, with a discrete tuning range of ~290 GHz. The threshold current density was 1150 Acm^{-2}, with maximum operating temperature of ~70 K and peak optical output power of ~8 mW. The four primary quasi-single-mode emission frequencies were determined to be 3.06, 3.21, 3.28 and 3.35 THz. The mid-value of the drive current range for each frequency was chosen as its operating current level to maximise output power. 3.13 THz was avoided for imaging purposes because emission was not single mode. As a result, it would add complications to the experimental data analysis. Hence, the operating currents for the 3.06, 3.21, 3.28 and 3.35 THz emission frequency lines were 2.72, 3.24, 3.60, 3.80 A, respectively.

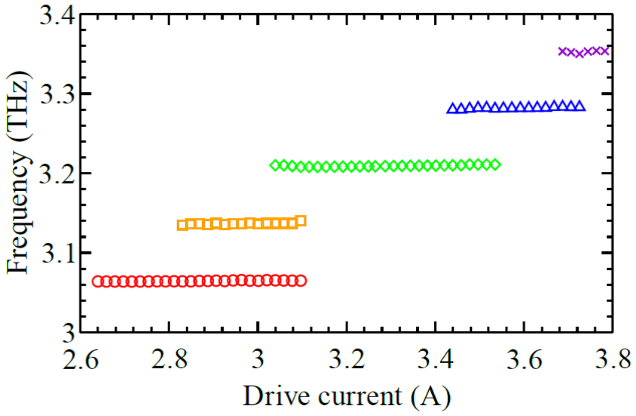

Figure 3.4: Peak emission frequency at various drive current levels. Spectral intensities below 20 dB of peak emission have been neglected. Data courtesy of Dr A. Valavanis and have been presented in Ref. [187].

Imaging was carried out by mounting either two or three samples on a two-axis translational stage and raster scanning them across the focal plane of the incident THz radiation with a step size of 250 μm. A time-averaged lock-in signal was measured with a time constant of 10 ms for each point. A 120 × 120 pixel image was acquired for each frequency point, totalling to ~20 minutes of scan time for all four frequency points. All the measurements were carried out under normal atmospheric conditions (i.e. not in a purged environment), thereby demonstrating real-world application of this technique.

3.3 System characterisation

The THz radiation spot size on the sample plane was measured using a 'knife-edge' measurement technique. A gold-coated ISO P120 sandpaper, with an average particle size of 120 μm, was placed on a smooth microscope glass coverslip. It was mounted on the sample holder of the translational stage, scanned in the x-direction through the radiation spot (as shown in Figure 3.3) and the DR power at 3.28 THz was measured close to the edge of the gold-coated sandpaper. The translational stage was moved in the z-direction to optimise the focal spot size. An image of the gold-coated sandpaper during one of the scans at 3.28 THz is shown in Figure 3.5 (a). The measured DR power across the edge of the gold-coated sandpaper followed a Gauss error function with a half-width at half-maximum $\omega = \sim 1.5$ mm as shown in Figure 3.5 (b). The measurement was carried out by Dr A. Valavanis. Note that a smaller spot size of ~300 µm with the same system has been reported earlier using a 2.8 THz QCL [162]. Since this work has been carried out with a THz QCL operating at higher frequency, better system resolution can be achieved. An optimised spot size was not a necessity as a number of independent measurements of the sample could be performed with the spot size obtained. A tightly focussed spot was not required as obtaining powder distribution was not of interest in the current work. Besides, a relatively big spot helped in averaging out variations in the powder. Since the powder grain size used for this work was ~10–15 µm, it can be considered as a quasi-homogeneous scattering media within the frequency domain of interest.

The contrast performance of the imaging system was characterised by modulation transfer function (MTF) technique. This method is used to measure how accurately does the imaging system image an object. Ideally, a sinusoidal varying pattern has to be scanned across the sample plane to obtain a sine-wave-like response, but fabricating such a test pattern is difficult. Hence, a bar pattern of gold-on-glass was used as a resolution target to scan across the sample plane in both horizontal (x) and vertical (y) directions. The MTF of the system shown in Figure 3.5 (c) was obtained by measuring the square-wave modulation and applying a first-order Coltman expansion [188]. The MTF was fairly constant until a spatial frequency of 0.6 mm^{-1}, which corresponds to spatial distance of approximately 1.7 mm. This estimate of the spot size was close to the result from 'knife-edge' measurement. The method has also been explained in Ref. [162]. This measurement was courtesy of D. R. Bacon and Dr A. Valavanis.

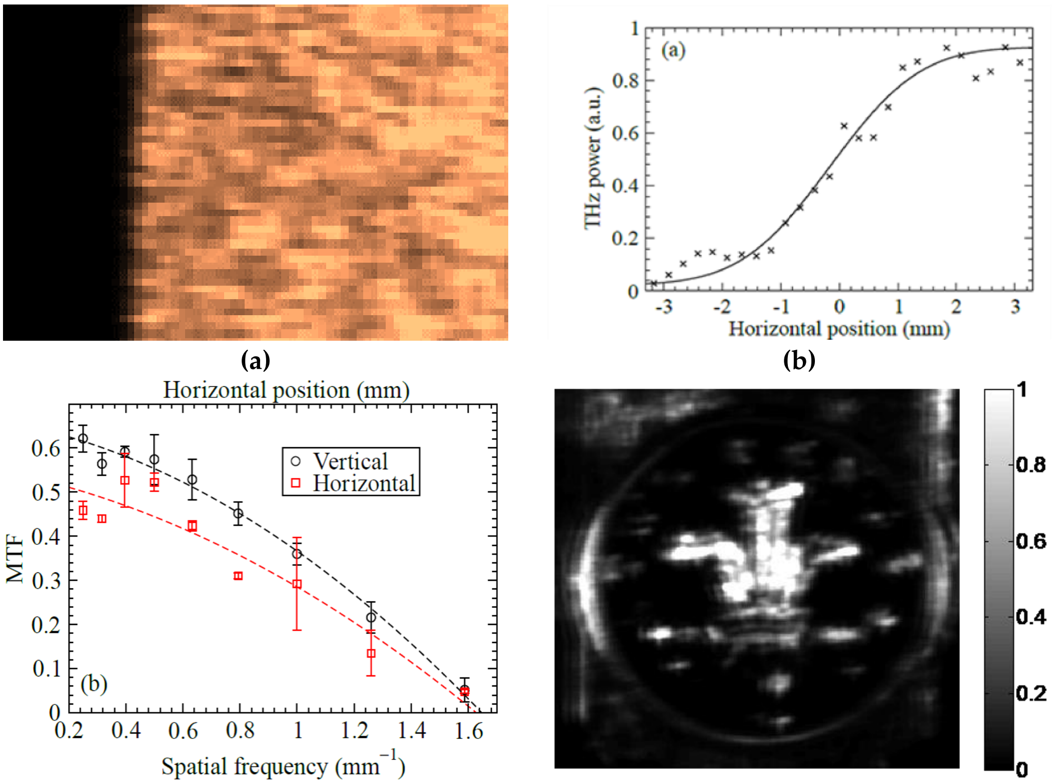

(a) **(b)**

(c) **(d)**

Figure 3.5: (a) Diffuse reflection image obtained of gold-coated sandpaper (bright area) on a glass coverslip (dark area) at 3.28 THz. (b) Measured THz power as scanned across the edge of gold-coated sandpaper at 3.28 THz. A fitted Gauss error function is represented by the solid line. (c) MTF scans performed in both horizontal (x) and vertical (y) directions with error bars signifying the range of values obtained from three individual scans. (d) Diffuse reflection image of a two pence coin taken at 3.28 THz. Data shown in (b) and (c) courtesy of Dr A. Valavanis and D. R. Bacon.

To demonstrate the quality of the imaging system, a two-pence coin was mounted on a microscope coverslip and placed on the sample holder. It was cleaned with citric acid and a mixture of acetone and methanol to remove any inorganic and organic contaminations from its surface. A two-dimensional image was acquired at 3.28 THz with a step size of 0.25 mm as shown in Figure 3.5 (d). The strong reflections on the right and left edges of the coin were actually the specular off-axis reflections from the edge of the glass coverslips. Areas with no textures or writing appear very dark as they are smooth surfaces and diffuse reflections are minimal. With this resolution small features on the coin were visible.

An arbitrary spot on the gold-coated sandpaper was used to approximate a perfectly diffuse reflecting sample. The maximum SNR of the system was estimated as the ratio of the mean to the standard deviation of the signal obtained from the lock-in amplifier at a 10 ms and 1 s time-constant for each of the emission frequencies as shown in Table 3.1. The SNR achieved with a 10 ms time-constant was between ~15–20 dB but was improved by ~20 dB when the lock-in time-constant was increased to 1 s.

The bolometer was the only optical component that could be displaced easily on an everyday basis when it was topped up with liquid nitrogen or helium. Everything else was bolted down to the optical bench. To realign the bolometer, the gold-coated sandpaper was placed on the sample mount of the translational stage. The stage was positioned so that the THz beam spot was on the gold-coated sandpaper. The bolometer was manually positioned to improve the DR signal measured on the lock-in amplifier.

Frequency (THz)	**SNR (10 ms)**	**SNR (1 s)**
3.06	20.5	40.9
3.21	15.1	36.0
3.28	23.1	42.8
3.35	15.2	39.0

Table 3.1: SNR in decibels for each emission frequencies. Data courtesy of Dr A Valavanis and has been presented in Ref. [187].

3.4 THz TDS reference measurement

THz TDS was performed on the samples used for diffuse reflectance measurements.

These measurements were done to provide a reference value of absorption coefficients obtained from a conventional technique to be compared with the absorption coefficients inferred from DRI measurements. The THz TDS apparatus has already been explained in 1.3.1.1. As the THz TDS technique employed here is a transmission measurement, the THz pulse had to pass through the sample to be measured. Most of the signal would have been lost due to scattering by loosely packed powdered particles. Hence samples were prepared in the form of pressed pellets for THz TDS as explained below. Conversely, samples for diffuse reflectance imaging measurements were prepared in powdered form, as explained in Section 3.5. Pellets with almost smooth surfaces would have very weak diffuse reflection and hence would be unsuitable for DRI because specular reflection would be more prominent.

All the samples prepared and measured using THz TDS have been listed in Table 3.2. A total powder admixture of 40 mg was weighed precisely using an OHAUS Adventurer Balance AR0640. It was then placed within a thin copper O-ring and a mechanical force of 8–8.5 tons was applied for 5 minutes using a SPECAC Manual Hydraulic Press. The powdered admixture was pressed into a circular pellet of 8 mm diameter and 0.3-0.4 mm thickness as shown in Figure 3.6.

Figure 3.6: Optical image of a sample pressed into a pellet for THz TDS measurement.

Sample	Sample
PTFE 55 μm	Granulated Sugar
Glucose Monohydrate	Sucrose
Glucose Monohydrate	Caffeine
Lactose Monohydrate	Lydocaine
Glucose Anhydrous	Benzocaine
Lactose Anhydrous	Cellulose micro-granular
Ammonium Nitrate	

Table 3.2: Samples prepared for THz TDS and DR imaging measurement

A reference time-delayed THz pulse scan was taken without any sample placed in the system. Pellets were then placed in the sample holder. For each pellet, ten scans were performed at a single position on the sample surface and averaged in order to reduce any pulse amplitude error due to fluctuation of laser intensity, or optical, electronic and mechanical errors. Nine different positions were scanned and averaged to minimize error due to inhomogeneity of the sample. The obtained electric fields of the reference signal and from the sample were terminated after ~5 ps in order to eliminate the effect of any reflected THz radiation from the electro-optic crystal. Signals were then padded to a total length of 15 ps in time with the last known amplitude. A fast Fourier transform (FFT) was performed on the reference and sample signals. Padding of the signal helped to achieve interpolation between specific frequencies, and hence smoothing of data points. Due to termination of the time-domain signal, the spectral resolution was ~175 GHz before padding of the signal. A typical reference time-domain THz pulse and THz pulses through pressed pellet of 100% sucrose, 100% caffeine and 100% cellulose microgranular are shown in Figure 3.7. Most noticeably signals detected through samples show a decrease in amplitude and a phase lag as compared to the reference signal.

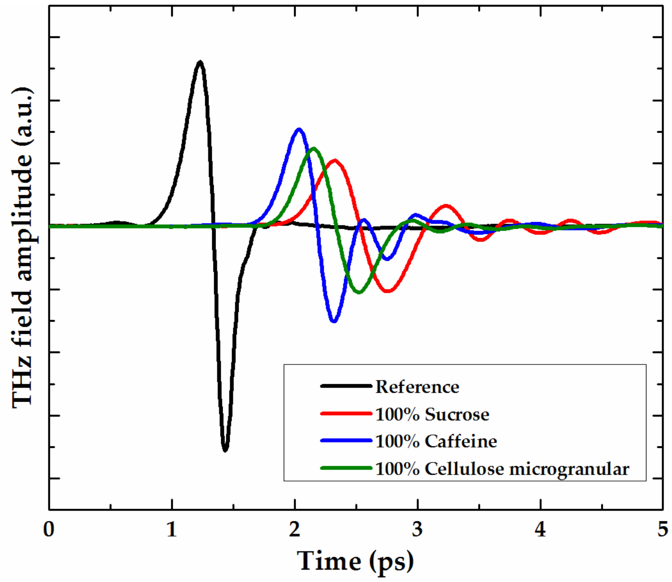

Figure 3.7: Time-domain THz reference pulse (black line) and pulses through 100% sucrose, 100% caffeine and 100% cellulose microgranular samples (red, blue and green lines respectively).

The frequency domain signal was further processed mathematically to obtain the refractive index, absorption coefficient of the sample under consideration and maximum measureable absorption coefficient. The pellet was assumed to be quasi-uniform and therefore the effect of radiation scattering was considered negligible. The measurement technique and the following analysis have already been reported in Ref. [165].

The refractive index of the sample under consideration, $\mathrm{n_{sam}}(v)$, Fresnel reflection coefficient, $\mathrm{R}(v)$ and absorption coefficient, $\alpha_{\mathrm{TDS}}(v)$ can be expressed as:

$$\mathrm{n_{sam}}(v) = 1 + \frac{c}{2\pi d v}[\varphi_{\mathrm{sam}}(v) - \varphi_{\mathrm{ref}}(v)] \qquad 3.1$$

$$\mathrm{R}(v) = \left|\frac{\mathrm{n_{sam}}(v) - \mathrm{n_{air}}}{\mathrm{n_{sam}}(v) + \mathrm{n_{air}}}\right|^2 \qquad 3.2$$

$$\alpha_{TDS}(v) = -\frac{2}{d}\ln\left\{\frac{\mathrm{A_{sam}}(v)}{\mathrm{A_{ref}}(v)(1-\mathrm{R}(v))}\right\} \qquad 3.3$$

where c is the speed of light, d is the thickness of sample, v is frequency, [$\varphi_{\mathrm{sam}}(v)$, $\mathrm{A_{sam}}(v)$] and [$\varphi_{\mathrm{ref}}(v)$, $\mathrm{A_{ref}}(v)$] are the phase and amplitude of the sample and reference in frequency domain, respectively, and $\mathrm{n_{air}}$ is the refractive index of the air, assumed as 1 [157].

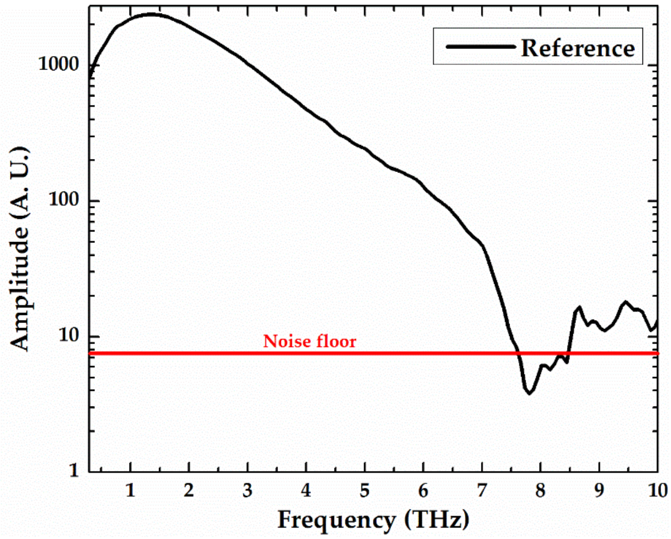

Figure 3.8: Fast Fourier Transform of the reference signal with the noise floor marked in red.

The absorption coefficient calculated using THz TDS has certain limitations which has been qualitatively explained in Ref. [189]. The maximum measureable absorption coefficient of a system largely depends on the noise floor (NF) of the system. A signal level just above the maximum bandwidth of the reference scan was estimated as noise floor of the system, as shown in Figure 3.8. The dynamic range (DR) can be expressed as DR = (A_ref (v)) / NF and the maximum measureable absorption coefficient α_{MAX}, of the system was calculated using the following equations: [189]

$$\alpha_{\mathrm{MAX}} = \frac{2}{d}\ln\left[\mathrm{DR}\,\frac{4\mathrm{n}_{\mathrm{sam}}(v)}{(\mathrm{n}_{\mathrm{sam}}(v)+1)^2}\right] \qquad 3.4$$

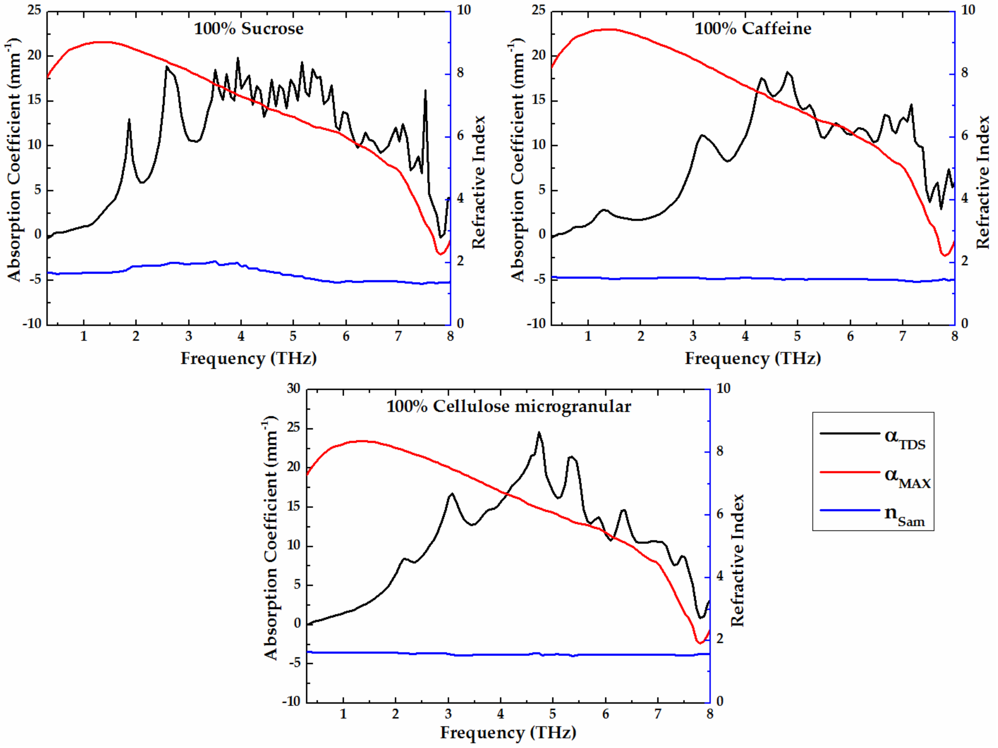

Figure 3.9: Absorption coefficient α_{TDS} (black line), maximum measureable absorption coefficient α_{MAX} (red line) and refractive index $\mathrm{n}_{\mathrm{sam}}$ (blue line) calculated from the time-domain THz pulses for various pure samples.

Figure 3.9 shows exemplar traces of the absorption coefficient, maximum measureable absorption coefficient and refractive index of 100% sucrose, 100% caffeine and 100% cellulose microgranular samples. Similar calculations were carried out for all the measured samples in Table 3.2. Each sample shows a unique spectral fingerprint. The absorption coefficient values are unreliable once it exceeds the maximum measureable absorption coefficient. [189, 190]. But this does not limit the measured refractive index [189].

3.5 Diffuse reflectance sample preparation

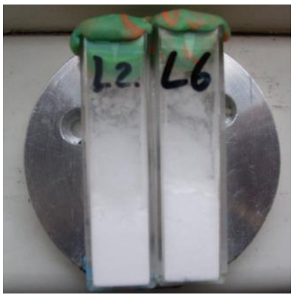

Figure 3.10: Optical image of powdered samples filled into plastic cuvettes. (left) PTFE as a reference and (right) 60% glucose monohydrate sample. Image presented in [186].

Crystalline and polycrystalline samples with broad absorption features between 3 and 3.4 THz were chosen for this multi-frequency imaging purpose. They were dehydrated in an oven at 40 °C for 48 hours to remove any moisture content. Each of the powdered solids was then ground for five minutes using a pestle and mortar to break them up into smaller particles. Amongst all the selected compounds, polytetrafluoroethylene (PTFE) powder was not ground as it aggregated and formed clusters. Instead, PTFE powder was commercially sourced with particle diameter of 55 μm. This was used as a fixed reference sample as it has a low absorption coefficient over the THz frequency range under consideration, and does not exhibit any spectral absorption peaks in this range.

Most of the samples (listed in Table 3.2) were blended with PTFE, by weight, in order to dilute the absorption features of these highly absorbing materials. The admixture was gently stirred for 5 minutes using a thin sample spatula before being loosely packed in flat-sided 10 ml polystyrene cuvettes and mounted on the sample holder of the two-axis translational stage as shown in Figure 3.10.

3.6 Diffuse reflectance imaging of powdered samples

Data processing was performed offline using commercially available software (MATLAB). Each sample powder mentioned in Table 3.2 was scanned at four-different frequencies along with the fixed PTFE reference. Image of PTFE and 60% glucose monohydrate at four different frequencies are shown in Figure 3.11 (a). A relatively high diffusely reflected signal is observed in the areas around the edges of cuvette. This is due to strong off-axis specular reflections.

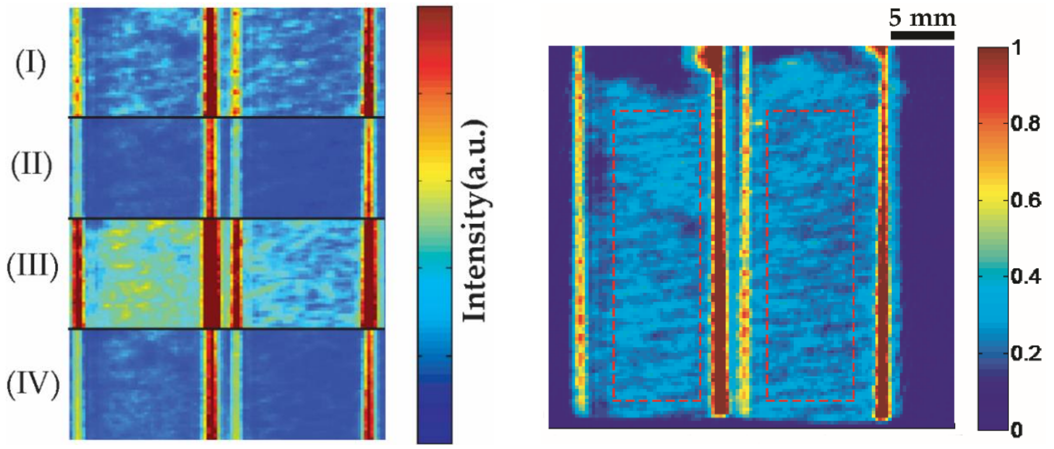

(a) **(b)**

Figure 3.11: (a) Four colour diffuse reflection images at (I) 3.06 THz, (II) 3.21 THz, (III) 3.28 THz, and (IV) 3.35 THz of powdered 55 μm PTFE (left cuvette) and 60% glucose monohydrate (right cuvette). The red dotted line in (b) shows the enclosed powder area used for data analysis.

Due to the uneven distribution of particle sizes, measurement of such samples causes significant variation in the recorded data, leading to a substantial standard deviation. In order to improve accuracy, a large number of independent points have been scanned across the sample surface and their intensity averaged. For any given image, the region surrounded by red dotted lines as shown in Figure 3.11 (b), both for reference and sample, was used for calculating the number of pixels enclosed $\mathrm{N_{px}}$, mean intensity μ_p, and its standard deviation σ_p. To improve accuracy, pixels on the edge of the cuvettes were avoided in calculations, as their intensity was influenced by the strong off-axis specular reflections from the edges of the container. Typically ~1000 pixels were obtained, with a pixel size of $\mathrm{A_{px}} = 0.25 \times 0.25\ \mathrm{mm}^2$. The relative reflectance of each sample with respect to the PTFE powder, $\mathrm{R_{rel}}$, was calculated by dividing the mean intensity of the sample, μ_sample, with that of the PTFE, μ_ref, as $\mathrm{R_{rel}} = \mu_\mathrm{sample}/\mu_\mathrm{ref}$.

Since the THz spot size was bigger than the pixel size, an approximation of the number of independent sample points, N, per powder scan was obtained by dividing the total image area ($\mathrm{N_{px}A_{px}}$) by the THz beam spot area ($\pi\omega^2$). It can be represented as $N = N_{px}A_{px}/\pi\omega^2$. Typically $\mathrm{N}{\sim}20$ for any given image.

As the powders were inhomogeneous, the standard deviation of the reflected radiation would only represent the intrinsic inconsistency within the sample rather than the image. Hence, the standard relative uncertainty, υ_p, in the mean value of the powder's DR would take into account the independent sample points, N. It can be represented as $\upsilon_\mathrm{p} = \sigma_\mathrm{p}/(\mu_\mathrm{p}\sqrt{\mathrm{N}})$.

Therefore, the standard relative uncertainty in the relative diffuse reflectance of a sample, υ_R could be calculated as the root-sum-square of the standard relative uncertainty in the mean value of the reference and the sample, and can be expressed as $\upsilon_\mathrm{R} = \left(\upsilon_\mathrm{P,sample}^2 + \upsilon_\mathrm{P,ref}^2\right)^{1/2}$. The absolute standard uncertainty in mean value of relative diffuse reflectance, $\mathrm{R_{err}}$, can be calculated as:

$$\mathrm{R_{err}} = \upsilon_\mathrm{R} \times \mathrm{R_{rel}} \qquad 3.5$$

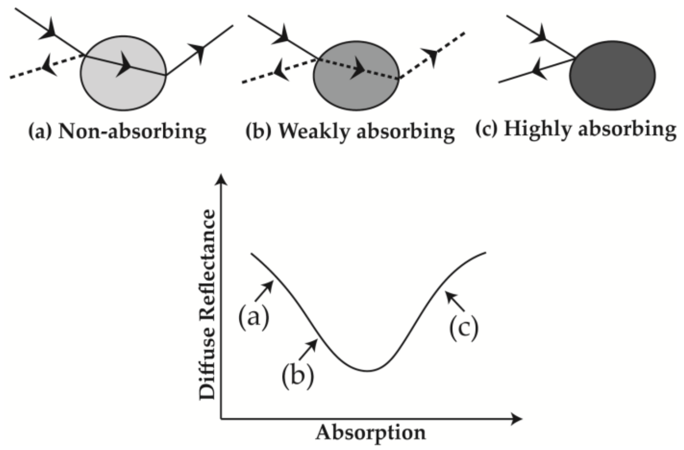

Figure 3.12: Illustration of diffuse reflection from (a) non-absorbing, (b) weakly absorbing and (c) highly absorbing samples. The graph shows a rough trend of diffuse reflectance as function of absorption.

Diffuse reflectance of fine-grained powder samples can be broadly divided into three different types as shown in Figure 3.12. For a completely non-absorbing sample very high diffuse reflectance is expected as there is no radiation loss due to absorption when the signal is scattered by the material (Type 'a'). Samples which are mildly/weakly absorbing, the diffuse reflectance signal drops with increase in absorption (Type 'b'). The radiation travels through the particles with finite absorption and gets scattered. On the other hand, samples that are very strongly absorbing, also have very high Fresnel surface reflectivity, and do not allow radiation to pass through it. Most of the signal reflects from the surface of the particles and hence diffuse reflectance signal also increases with increase in absorption (Type 'c'). The relationship of diffuse reflectance as a function of absorption is schematically illustrated in the graph shown in Figure 3.12. These diffuse reflectance behaviours have further been explained in Ref. [191].

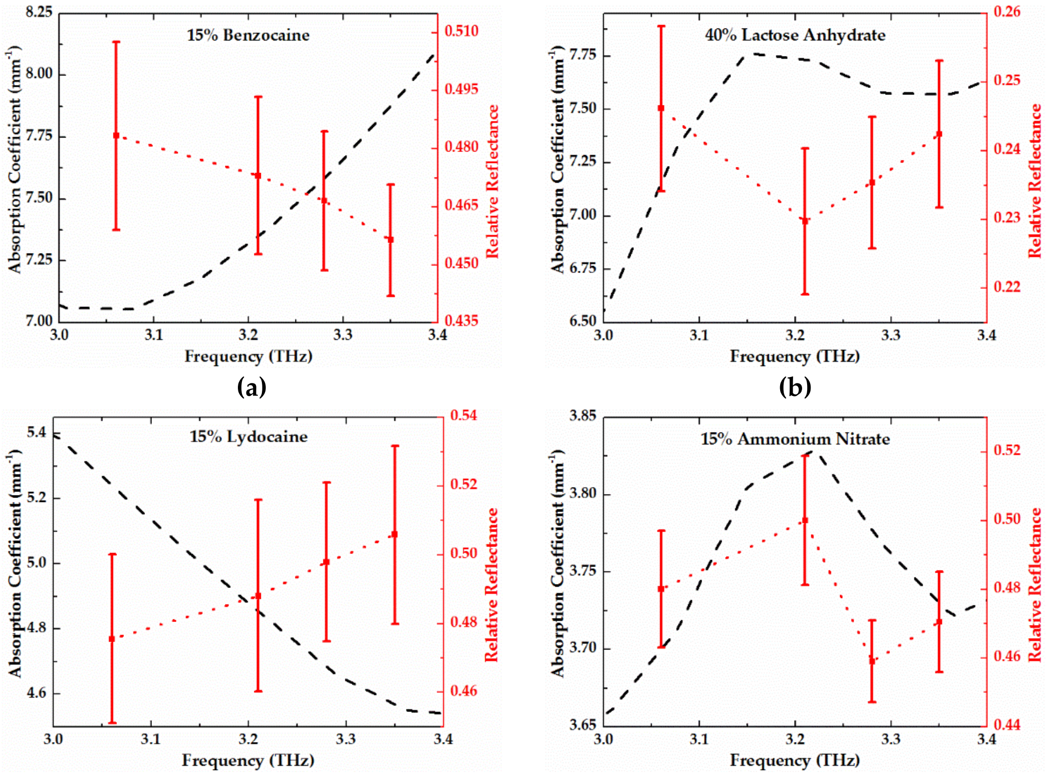

(a) **(b)**

(c) **(d)**

Figure 3.13: Absorption coefficient obtained from THz TDS (black dotted lines) and relative diffuse reflectance (red scattered plot) (a) 15% Benzocaine, (b) 40% lactose anhydrous, (c) 15% lydocaine and (d) 15% ammonium nitrate. The error bars indicate the absolute standard-uncertainty υ_R in the mean of relative diffuse reflectance.

As most of the samples used for this work were weakly absorbing (Type 'b'), there should be an inverse relationship between absorption and relative reflectance. An increase in absorption would lead to lower relative reflectance value and vice-versa. Figure 3.13 shows exemplar plots of absorption coefficient calculated from the THz TDS measurements and relative reflectance with $\mathrm{R_{err}}$ as error bars for various diluted samples. For benzocaine, the absorption coefficient increases with frequency whereas the relative diffuse reflectance drops. The complete reverse was observed for the lydocaine sample. The inverse relationship between absorption coefficient and relative reflectance also agrees well for the lactose anhydrous sample. The relationship between the absorption coefficient and relative diffuse reflectance agreed with these findings in all the finely powdered samples measured. This is because they do not have very high absorption coefficient and the majority of the diffuse reflections arises from the subsurface grains rather than from the surface of randomly oriented particles.

Ammonium nitrate is a very highly absorbing material [8] and acts more like Type ‘c’ materials as explained earlier. Hence the relative diffuse reflectance of ammonium nitrate does not follow the trend of Type ‘b’ materials. Most of the radiation is reflected from the arbitrarily positioned particles at the surface of the material [191], causing high Fresnel reflections, and therefore an increase of diffuse reflectance with an increase in absorption coefficient is expected. Considering this, the relative diffuse reflectance follows the trend of the measured Beer–Lambert absorption coefficient (see Figure 3.13 (d)). As THz TDS measurements were performed in a transmission geometry, there is a limit to the maximum sample concentration that can be measured within the dynamic range of the system. Therefore, higher concentration samples were not studied further in this work. But the diffuse reflectance measurement technique is not limited by this factor and potentially higher concentration samples could be studied in future.

Imaging of 5–100% concentration of cellulose microgranular and lactose monohydrate admixture with PTFE were carried out at the four imaging frequencies. The relative diffuse reflectance of the samples at the four imaging frequencies as a function of the sample concentration is shown in Figure 3.14. As the concentration approaches zero, the relative diffuse reflectance value tends to 1, an obvious result as the sample and the reference material were both essentially PTFE powder. From Figure 3.14, it can be observed that relative diffuse reflectance of cellulose increases with frequency, signifying a decrease in absorption coefficient. Hence the data reveals some spectroscopic information about the samples imaged. Further analysis of the data has been explained in the next section.

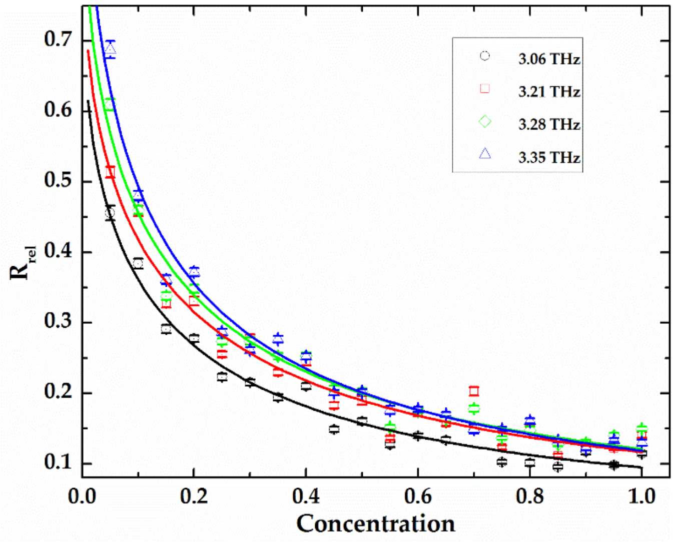

Figure 3.14: Relative diffuse reflectance of cellulose microgranular as a function of admixture concentration with PTFE at the four different emission frequencies. The dotted lines shows the fitting of equation 3.13 with γ=1.03. Data courtesy Dr A. Valavanis and A. R. Clarkson. Image replotted from Ref. [187].

For real world applications such as security screening of explosives and other hazardous materials, a large working distance is desirable for an imaging system. The optical path length between the sample and detector was ~30 cm. To test the robustness of the diffuse imaging system, the distance was increased to ~1.5 m by reflecting the collected radiation from the sample through a number of plane mirrors and focusing onto the detector. A range of samples was rescanned with the extended system to confirm repeatability of relative diffuse reflectance measurements, as carried out with the short working distance setup. The extended optical path between the sample and detector is illustrated in Figure 3.15 (b). The relative diffuse reflectance values for various samples scanned in each system configuration is shown in Figure 3.15 (c) and (d). The error bars show the absolute uncertainty in the

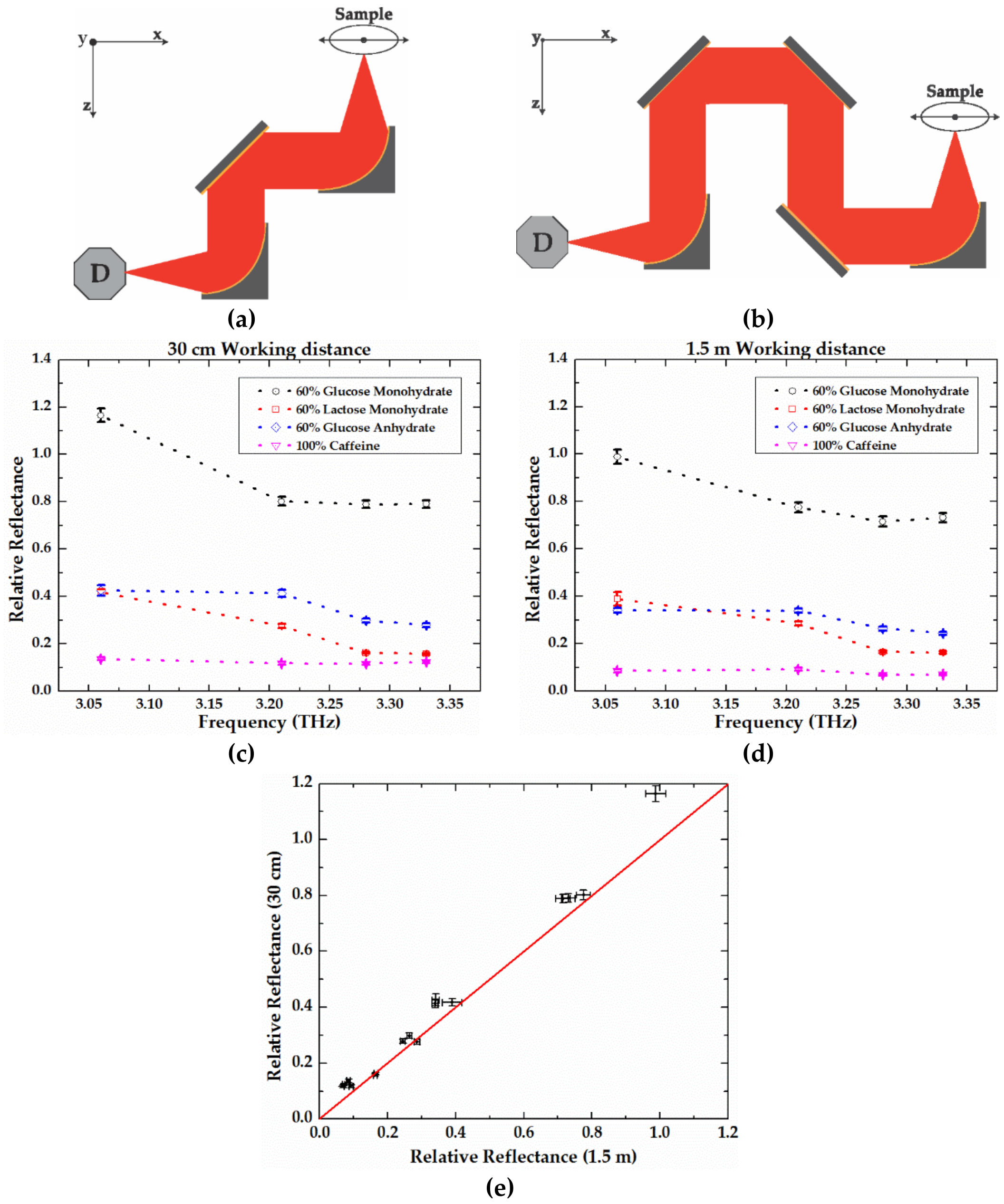

Figure 3.15: Schematic of optical path of the collection optics of the DRI system between sample and detector for (a) ~30 cm and (b) ~1.5 m working distance. Comparison of relative reflectance for various samples at (c) ~30 cm and (d) ~1.5 m working distance. (e) Linear correlation between the data sets. Identity line shown as red line. Data shown in (c) courtesy of Dr A. Valavanis.

mean value and are calculated using Equation 3.5. A linear correlation between the relative diffuse reflectance values demonstrates agreement between both configurations as shown in Figure 3.15 (e). The red solid line represents the line of equality.

3.7 Extraction of absorption coefficient

Imaging of samples in spectroscopic systems such as THz TDS allows access to material specific spectral signatures of absorption coefficient and refractive index. Previously, scattering models such as the effective field approximation (EFA) [162], quasi-crystalline approximation (QCA) [162], QCA along with the Percus–Yevick pair distribution function [165], and the Kubelka–Munk (KM) theory [162] have been used to derive Beer–Lambert absorption coefficient using data obtained from diffuse reflectance imaging. The QCA model assumes scattering media to be perfectly spherical monodisperse particles and also takes into account correlation between particle positions. For very dilute samples, particle positions can be neglected (assumed as independent) and the model reduces to a much simpler version known as EFA. Further, Percus–Yevick pair distribution of polydispersive randomly sized scattering particles have been applied along the QCA model to calculate effective absorption coefficient of samples. Although the QCA approach requires prior knowledge of various particle parameters such as particle size, volume fraction and refractive index, it provides accurate reproduction of absorption coefficients [34]. Despite its advantages, it is numerically intensive and results can be unreliable over a wide range of frequencies [187].

The KM model previously reported obtained absorption coefficient values at single frequency whereas this work reports calculation of KM absorption coefficient using multi-frequency THz source and has been further detailed in Section 3.7.2.

In this work, a new, numerically simple effective-optical-path-length model has been developed and the well-established KM theory has been used to infer absorption coefficient from diffuse reflectance data of the samples measured. Analysis has been done for all four frequency points and compared with Beer–Lambert absorption coefficients obtained from a more established THz TDS technique.

3.7.1 Effective optical path length

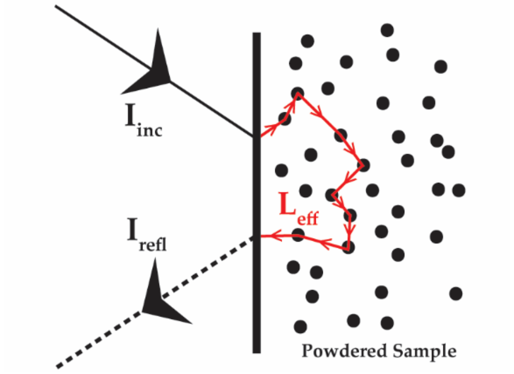

Figure 3.16: Illustration of effective optical path length model.

A simple effective-optical-path-length (EOPL) technique has been hypothesised to calculate absorption coefficient from DR measurements. In a crude approximation, THz radiation has been considered to behave as ray of light. Radiation incident on a powdered sample gets partly absorbed and reflected after traversing an effective length of L_{eff} through the material (see Figure 3.16). Using the Beer–Lambert law, the intensity of incident ($\mathrm{I_{inc}}$) and reflected ($\mathrm{I_{refl}}$) radiation can be related to the absorption coefficient (α) of the material via $\mathrm{I_{refl}} = \mathrm{I_{inc}} \mathrm{e}^{-\alpha L_{\mathrm{eff}}}$. The reflectance is $\mathrm{r} = \mathrm{I_{refl}}/\mathrm{I_{inc}} = \mathrm{e}^{-\alpha L_{\mathrm{eff}}}$. The relative reflectance of the sample with respect to a reference material can be expressed as $R/R_0 = \mathrm{e}^{(-\alpha \mathrm{L_{eff}})}/\mathrm{e}^{(-\alpha_{\mathrm{ref}} \mathrm{L_{eff,ref}})}$, where R_0 and α_{ref} are the reflectance and absorption coefficient of reference sample, respectively. The effective length traversed by the radiation through the reference material has been represented by $\mathrm{L_{eff,ref}}$. The natural logarithm of the previous equation can be expressed as:

$$\ln\left(\frac{R}{R_0}\right) = \alpha_{\mathrm{ref}}\mathrm{L}_{\mathrm{eff,ref}} - \alpha L_{\mathrm{eff}} \qquad 3.6$$

As the reference (PTFE) has low absorption over the frequency range of interest, $\alpha_{\mathrm{ref}}\mathrm{L}_{\mathrm{eff,ref}}$ can be assumed to be negligible compared with αL_{eff}. The effective path length L_{eff} is assumed to be a multiple (b) of the free-space wavelength (λ) of the incident radiation. Therefore the effective optical path length can be expressed as $L_{eff} = b\lambda$ and the Beer-Lambert absorption coefficient can be inferred using the following equation [34, 192]:

$$\alpha = -\frac{1}{b\lambda}\ln\left(\frac{R}{R_0}\right) \qquad 3.7$$

The frequency independent dimensionless parameter b was calculated by linear regression of the measured data of various concentrations of granulated sugar. It was found to be 0.60 ± 0.06. Using this value, α was calculated for 15% and 100% granulated sugar-PTFE admixture samples at all four emission frequencies. Figure 3.17 shows the absorption coefficient obtained from THz TDS (solid lines) and inferred absorption coefficient from relative reflectance (square boxes) at the four emission frequencies. The absorption coefficient calculated with the error limit of relative reflectance has been shown as error bars.

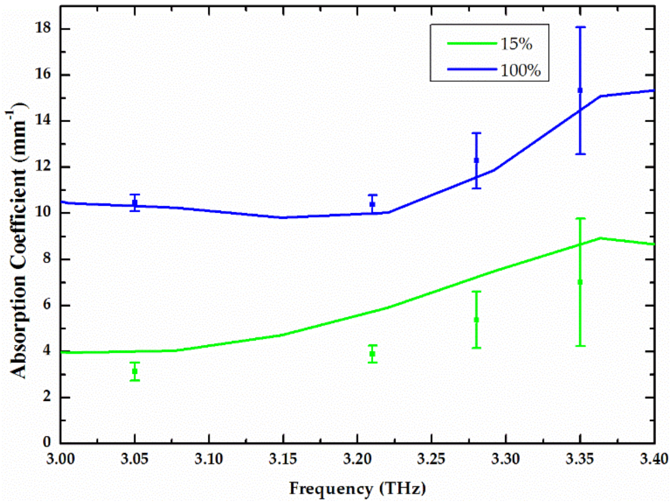

Figure 3.17: Comparison of absorption coefficient obtained from THz TDS (solid lines) and using EOPL model (square boxes) on relative diffuse reflectance data of 15% and 100% concentration of granulated sugar admixture with PTFE by weight, at the four imaging frequencies. Image presented in Ref. [34, 192].

As the terahertz wavelength is much bigger than the particle size, the radiation cannot be assumed to behave like a ray of light reflecting/refracting from the surface of the powdered particles. Realistically, it needs to be considered as a field incident on the particles and then remitting out in scattered directions. Although the approximation used for the model is flawed and the technique also neglects the particle geometry or the polarisation of incident radiation, it does produce reasonable agreement with Beer-Lambert absorption coefficient values obtained from THz TDS measurements [34, 192]

3.7.2 Kubelka–Munk theory

KM theory, another relatively simple analytical model was used to predict the Beer–Lambert absorption coefficient. Unlike the QCA model, it does not predict the absolute Beer–Lambert absorption coefficient but does reproduce the relative value reasonably accurately. The model used for this work has been validated at a single THz QCL frequency previously [162].

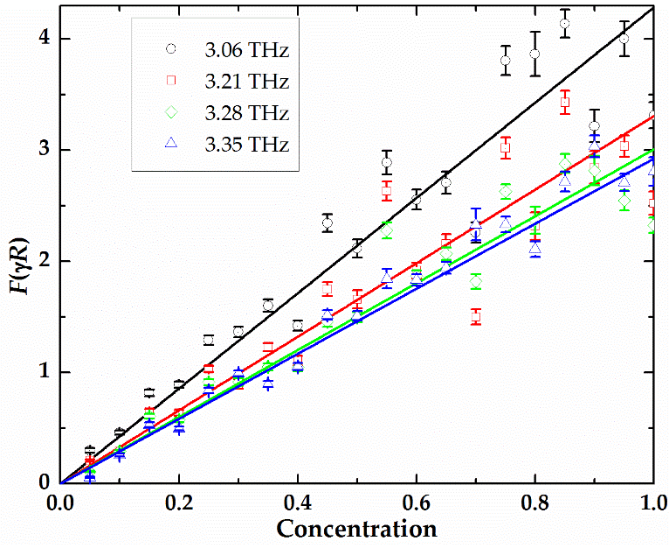

Figure 3.18: Kubelka–Munk remission function as a function of cellulose mass-concentration in admixture with PTFE. The dotted line is a linear fit to the data and error bars are the standard uncertainty. Data courtesy of Dr A. Valavanis and A. R. Clarkson. Data replotted from Ref. [187].

The diffuse reflectance of a sample, is described in KM theory using the following equation [193]:

$$F(R_\infty) = \frac{K}{S} = \frac{(1 - R_\infty)^2}{2R_\infty} \qquad 3.8$$

where the KM remission function $F(R_\infty)$ is the ratio of the KM absorption coefficient, K, and the scattering coefficient, S. It further relates the relative diffuse reflectance R_∞ of an infinitely thick absorbing powdered sample to a purely diffusing and non-absorbing ideal reference sample. However, the real reference sample (PTFE) cannot be assumed as ideal as it is very weakly absorbing and R_∞ can be replaced by $R_\infty = \gamma R_{\text{rel}}$, in order to match the reflectance of PTFE to an ideal sample using a fitting constant γ [162, 187]. The reflectance relationship between PTFE and an ideal sample can be assumed to be proportional as the absorption coefficient and scattering parameter of PTFE are fairly constant over the frequency range. The KM absorption coefficient is assumed to be proportional to the Beer–Lambert absorption coefficient and therefore varies linearly with sample mass-concentration c. Thus, K can be represented as $\mathrm{K} = \beta\mathrm{\alpha}(\mathrm{c}) = \beta\mathrm{\alpha}_0\mathrm{c}$ where β is a sample-specific proportionality constant (related to its refractive index) and $\mathrm{\alpha}_0$ is the absorption coefficient of the undiluted sample [194]. Equation 3.8 may be further written as follows:

$$F(\gamma R_{\mathrm{rel}}) = \frac{\beta\alpha(c)}{S} = c\frac{\alpha_0\beta}{S} = \frac{(1-\gamma R_{\mathrm{rel}})^2}{2\gamma R_{\mathrm{rel}}} \qquad 3.9$$

The natural logarithm of the above equation can be represented as:

$$\ln[F(\gamma R_{\mathrm{rel}})] = \ln(c) + \ln\left(\frac{\alpha_0\beta}{S}\right) \qquad 3.10$$

where, β and γ are the two unknown constants and the scattering coefficient S is considered a constant independent of frequency and concentration. The above equation is linear in the form $y = mx + C$ with slope $m = 1$ and y-intercept $C = \ln\left(\frac{\alpha_0\beta}{S}\right)$. Linear regression of $\ln[F(\gamma R_{\mathrm{rel}})]$ vs $\ln(c)$ would result in $\gamma = 1.03$ and $\ln\left(\frac{\alpha_0\beta}{S}\right) = 1.22$ for the cellulose microgranular sample. The KM remission function as a function of concentration is plotted in Figure 3.18 for the cellulose microgranular sample. The dotted line represents a linear fit as function of concentration. The experimental data is thus in good agreement with the analytical KM model. The error bars represents the standard uncertainty in the KM remission function $\upsilon_{\mathrm{F}(\gamma\mathrm{R}_{\mathrm{rel}})}$ and have been calculated using [195]:

$$\upsilon_{\mathrm{F(\gamma R_{rel})}} \approx \frac{\mathrm{d[F(\gamma R_{rel})]}}{\mathrm{d(\gamma R_{rel})}} \mathrm{R_{err}} \qquad 3.11$$

Equation 3.9 can be rearranged so that it forms a quadratic equation in terms of $\mathrm{R_{rel}}$

$$\gamma {R_{\mathrm{rel}}}^2 + R_{\mathrm{rel}} \left[-2\gamma \left(c\frac{\alpha_0 \beta}{S} - 1\right)\right] + 1 = 0 \qquad 3.12$$

As relative reflectance is known to decrease with increase in sample concentration, the negative branch of the solution to the quadratic equation is used as a fitting function in Figure 3.14, yielding very good agreement with the experimental data. The solution can be expressed as:

$$R_{\mathrm{rel}} = \frac{1 + c\frac{\alpha_0 \beta}{S} - \sqrt{c\frac{\alpha_0 \beta}{S}(2 + c\frac{\alpha_0 \beta}{S})}}{\gamma} \qquad 3.13$$

Having obtained the remission function values, the KM absorption coefficient can be calculated by rearranging equation 3.9 as $\alpha(c) = \frac{S}{\beta} F(\gamma R_{\mathrm{rel}})$. It can be assumed that the scattering coefficient and refractive index of the material are independent of sample concentration and fairly constant over the THz QCL emission frequency range of ~290 GHz, from 3.06 THz to 3.35 THz. Hence the scaling factor S/β remains constant for any given sample irrespective of the frequency and concentration. The KM remission function has been assumed to vary linearly with the Beer–Lambert absorption coefficient α_{TDS} obtained from THz TDS measurements. The scaling factor $\mathrm{S/\beta} = 5.23 \pm 0.17\,\mathrm{mm^{-1}}$ was determined from the gradient of a linear fit of α_{TDS} against $F(\gamma R_{\mathrm{rel}})$ in Figure 3.18 (a) for 5%, 15% and 100% cellulose concentration at each frequency point. The inferred KM absorption coefficient is compared with the measured Beer–Lambert absorption coefficient in Figure 3.19.

The KM absorption coefficient has fairly good agreement with α_{TDS} over the range of sample concentrations, but the absorption coefficient values were most accurately calculated for 15% concentration. The calculated KM absorption coefficient deviates from α_{TDS} for very high and very low concentration samples [193]. The model breaks down at low concentrations, as the absorption coefficient of the weakly absorbing matrix material cannot be neglected in comparison with the absorption coefficient of the diluted sample. The model tends to break at high concentration values, as the concentration dependence of the scattering coefficient cannot be ignored.

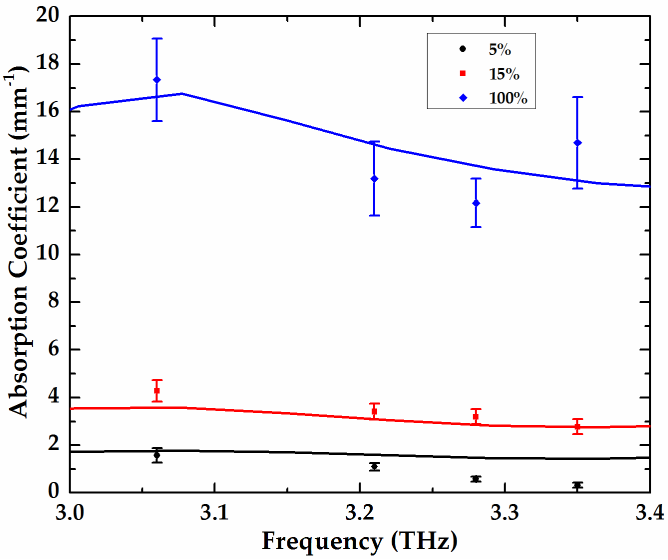

Figure 3.19: Comparison of absorption coefficients obtained from THz TDS (solid lines) and analytically calculated from Kubelka-Munk theory (symbols) using diffuse reflectance measurement for 5%, 15% and 100% cellulose microgranular. Data reproduced from Ref. [187].

The scaled-up KM remission function provided the absolute value of the absorption coefficient. The remission function itself conserves the spectral features of the Beer–Lambert absorption coefficient and the absolute value is not necessary in spectral identification techniques such as principle component analysis [11]. It is hypothesised that the calculated $\gamma = 1.03$ from the cellulose samples of various concentration would serve as a global constant for all other materials having PTFE as diluting matrix material as γ relates the reflectance of the reference PTFE material to a non-absorbing completely diffusing ideal reference sample. Having determined the only unknown parameter, γ, the KM remission function and absorption coefficients could be directly calculated for range of samples diluted with PTFE.

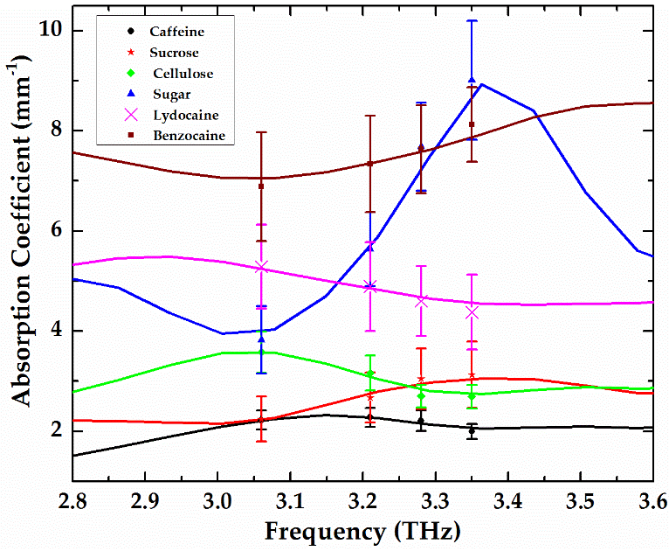

Figure 3.20: Comparison of absorption coefficients obtained from THz TDS (solid lines) and those inferred from diffuse reflectance imaging at the four emission frequencies using Kubelka–Munk theory (symbols) for caffeine (black circle), sucrose (red star), cellulose microgranular (green diamond), granulated sugar (blue triangle), lidocaine (pink cross) and benzocaine (brown square). 15% mass-concentration for all the samples admixture with PTFE. Data reproduced from Ref. [187].

The KM remission function was calculated for range of 15% mass-concentration samples using $\gamma = 1.03$. The scaling factor was obtained for each sample using linear regression as already explained for cellulose samples, and are given in Table 3.3. Figure 3.20 compares the Beer–Lambert absorption coefficients from the THz TDS and analytically calculated KM absorption coefficient on the same axes for various samples. The range of the Beer–Lambert absorption coefficient for all the samples considered were within 2–10 mm^{-1} with the scaling factor between 4–40 mm^{-1}. For these low-concentration samples a good agreement in terms of retracing the spectral features has been achieved between Beer–Lambert absorption coefficients and those calculated using the KM model. Due to the low sample concentration, the refractive index of all the samples studied here could be considered to be very close to that of PTFE, but the scattering coefficient differs with material leading to a different scaling factor. The model breaks down for high concentration of samples because the radiation scattering is dominated by the sample particles rather than the matrix material. Since the matrix material has a finite absorption and is not perfectly non-absorbing, the model breaks down for very low concentration of samples as well.

Materials	Scaling factor S/β (mm^{-1})
Caffeine	4.04 ± 0.05
Sucrose	26.4 ± 0.5
Cellulose	5.68 ± 0.09
Granulated Sugar	37.5 ± 0.6
Lydocaine	19.9 ± 0.3
Benzocaine	27.2 ± 0.3

Table 3.3: Scaling factor S/β (mm^{-1}) for 15% mass-concentration of various samples used in calculation of Kubelka-Munk remission function and absorption coefficient. Table reproduced from [187].

3.8 Summary

Diffuse reflection imaging of a range of powdered samples was performed using an electrically frequency-tuneable THz QCL as a radiation source emitting at 3.06, 3.21, 3.28, and 3.35 THz. Absorption coefficient values were inferred from relative reflectance measurements using two relatively simple analytical models: a new effective-optical-path-length model, and the well-established Kubelka–Munk theory. The absorption coefficients were compared with the Beer–Lambert absorption coefficients derived from complementary terahertz time-domain spectroscopy techniques.

These models did not reproduce absolute value of Beer–Lambert absorption coefficient but showed a scalable trend over the frequency range of the THz QCL (~290 GHz). To obtain accurate values of Beer–Lambert absorption coefficient, more complex analytical models such as a quasi-crystalline approximation can be used. The Kubelka–Munk model broke down for both very low and very high concentration samples but was shown to reproduce spectral features accurately for samples having absorption coefficient within the range of 2–10 mm^{-1}.

In this work, the diffusely reflected radiation off various powdered samples was measured using an incoherent bolometric detection technique. Imaging using coherent detection of signal has its own sets of advantages as this enables access to both the signal amplitude and phase information. This allows much more accurate determination of spectroscopic signatures such as refractive index and absorption coefficients. In order to obtain phase and amplitude information of THz QCLs, they should be phase locked to a known stable reference. Later in this thesis, the concept of photomixing [196] has been used to phase lock a THz QCL working under continuous-wave operation.

Chapter 4

Terahertz Photomixing

4.1 Background

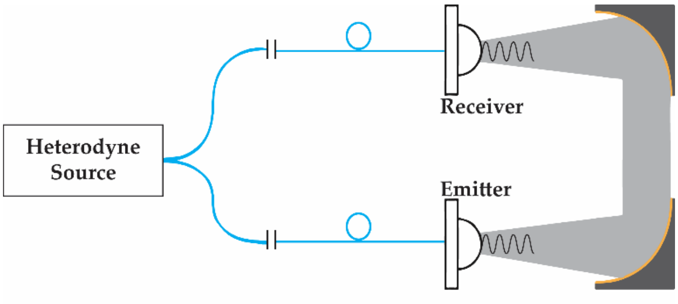

Figure 4.1: Basic schematic of a terahertz photomixing apparatus.

Terahertz photomixing refers to an optical heterodyning technique used to generate narrowband continuous-wave (CW) radiation in the terahertz range. By mixing two laser modes detuned at the intended terahertz frequency in a suitable material, its carriers are modulated at the beatnote (difference) frequency of the two laser modes, generating heterodyne emission. The output emission frequency can be tuned by changing the beat frequency between the two laser modes [197].

A basic photomixing schematic with all fibre coupled heterodyne source and photomixers (emitter and receiver) is illustrated in Figure 4.1. Optical radiation focused onto a biased photoconductive gap or the active region of a photomixer generates photocurrent. This is modulated at the beat frequency and coupled into an antenna structure for the emission of the electromagnetic radiation. A high resistivity hyper-hemispherical silicon lens can be placed behind the antenna to improve collection and collimation of the radiation. For detection, the incident THz radiation creates a bias across the metal-semiconductor-metal interfaces of the device. Free carriers generated by the incident THz radiation are thus modulated by the incident heterodyne beam. The photocurrent generated by separation of these carriers in the presence of the bias is then measured. Time delaying either the incident THz radiation or the optical envelope on the receiver can be used to map out the phase and amplitude of the THz field [97]. It is useful to have zero path delay between the detector optical beam and incident THz radiation from the emitter on the receiver, since this enables frequency-independent detection of the signal amplitude; due to finite linewidth of lasers, any jitter in frequency would translate to noise in amplitude for a non-zero path delay system. The signal detected on the receiver $\mathrm{I_{det}}$ at a finite path difference Δd is proportional to the incident THz field $\mathrm{E_{THz}}$ and optical beam on the detector $\mathrm{P_{opt}}$, and can be expressed as shown in Equation 4.1 where ν_{THz} is the heterodyne frequency and c is the speed of light [196].

$$\mathrm{I_{det}} \propto \mathrm{P_{opt}}\,\mathrm{E_{THz}} \cos\left(\frac{\nu_{\mathrm{THz}}}{\mathrm{c}}\Delta d\right) \qquad 4.1$$

Key limiting factors for high frequency operation of photomixers include the carrier lifetime, the transit time of carriers and the RC roll-off. The latter is due to the radiation impedance (R) of the antenna and the capacitance (C) of the metal-semiconductor-metal (MSM) interface in the active area of the device. These limiting factors have been explained in great detail in Ref. [197]. A sub-picosecond carrier lifetime of the material is essential as the photo-generated carriers are required to recombine quickly before the next cycle of the CW excitation. The transient time of the carriers to their respective electrodes is decreased by having gaps as small as possible between the electrodes, typically < 2 μm. However, too much reduction in the gap size would cause a reduction in the number of generated carriers and hence an overall loss in output power. As the time period between each cycle reduces with an increase in frequency, fewer carriers contribute towards generation of the beat frequency. This is due to the finite recombination time of carriers and the trade-off between a reduction of transit distance and the number of photo-generated carriers is therefore required [198].

RC roll off serves as another important limitation on the performance of these photomixers. The radiation impedance of the integrated antenna and the device capacitance are in parallel with the applied bias. For broadband antennas such as a log-spiral design, the radiation impedance is close to ~72 Ω across the working frequency range [197]. The capacitance of the device needs to be low enough to reduce the effect of RC roll off on the frequency response of the photomixer. A reduction in capacitance can be achieved by increasing the distance between the electrodes, or by reducing the overall active area of the device. However increasing the electrode separation would also increase the transit time of the carriers. Furthermore, reduction of the active area implies dissipation of higher optical powers in a smaller area, which could lead to problems such as thermal breakdown of the device [197]. Hence a compromise between the RC roll-off, thermal heating (P_{joule}) and transit time of the carrier (τ) has to be met. The following equation can be used to estimate the capacitance of the MSM structure analytically [199]:

$$C \approx \frac{\pi(1+\epsilon)\epsilon_0 A}{2(w+g)\log\left[2\left(1+\sqrt{\kappa}\right)/\left(1-\sqrt{\kappa}\right)\right]} \qquad 4.2$$

where

$$\kappa = \left(1 - \tan^4\left[\frac{\pi w}{4(w+g)}\right]\right)^{1/2} \qquad 4.3$$

and, ϵ, A, w, and g are the relative permittivity, the active area of the device, the width of each finger and the gap, respectively.

The following equations can be used to calculate P_{joule}, and the maximum THz emission power $P_{THz}^{max}(\omega)$ at any given frequency [200]:

$$P_{joule} = \left[\frac{\eta\mu e\tau}{gh\nu}\right]\frac{V_B^2}{\sqrt{A}}(P_1 + P_2) \qquad 4.4$$

$$P_{THz}^{max}(\omega) = \frac{2RP_{joule}}{\sqrt{A}}\left[\frac{\eta\mu e\tau}{gh\nu}\frac{mP_1P_2}{(P_1+P_2)}\right]\left[\frac{\tau}{[1+(\omega\tau)^2][1+(\omega RC)^2]}\right] \qquad 4.5$$

where $\eta, \mu, e, h\nu$ and V_B are the external quantum efficiency, effective carrier mobility, charge of an electron, photon energy and DC bias, respectively, and, P_1, P_2 are the optical laser powers and $\omega = 2\pi(\nu_1 - \nu_2)$, ν being one of the optical frequency.

The generation of CW radiation in the THz frequency range using the concept of photomixing was first reported in 1993 [201] on a LTG-GaAs substrate with bolometric detection. Subsequently, improved designs were reported with bandwidths up to 3.8 THz and higher output powers [49, 102, 202]. The first demonstration of simultaneous coherent generation and detection of CW-THz radiation was demonstrated in 1998 using two CW Ti:sapphire lasers and photomixers fabricated on LTG-GaAs substrate [97]. LTG-GaAs has always been the favoured material for photomixing due to its inherent properties such as high resistivity, high mobility and short carrier lifetime. ErAs:GaAs material has also shown an improved photomixing response [203, 204].

Initially photomixing at THz frequencies was done using wavelengths between 780–850 nm but attempts have been made to push it towards the more developed telecommunications wavelength range (1.3–1.55 μm). Performance of GaAs and InGaAs photoconductive materials as both a photoconductive switch and a photomixer have recently been reviewed in Ref. [78]. The first successful demonstration of photomixing with lasers working at telecommunications wavelengths was reported using the LTG-InGaAs as photoconductive material [205]. The material suffered from very high dark current leading to high background noise in the measurement. Many different techniques have been implemented to improve the photoconductive response of the material such as Fe-implanted InGaAs [206], ErAs:InGaAs [207], Br-irradiated InGaAs [208], Be-doped LTG InGaAs/InAlAs [209], Fe-doped InGaAs [210] and Cold Fe-implanted InGaAsP [211].

Apart from improving the photoconductive material characteristics for photomixing, enhancement of planar antennas and the MSM electrode designs also improves the out coupling of the generated electromagnetic radiation. Most of the developed photomixers have either resonant antenna designs [202, 212] or broadband antenna structures such as bow-tie [200], log-periodic [213] or log-spiral [203, 214] integrated with very closely spaced electrodes forming the active area of the device. The resonant antenna design has been proved to provide the highest output power, while the majority of reported photomixer active region designs have interdigitated electrode structures. Recently however, nano-gap electrodes with meander micro-antennas have been reported, claiming output emission powers two orders of magnitude higher than interdigitated structures with similar dimensions [98]. As well as that, plasmonic nanostructure electrode designs have also been demonstrated to have at least one order of magnitude higher THz output power efficiency, as compared to conventional interdigitated electrodes [99].

Conventional THz-TDS configurations are based expensive femtosecond Ti:sapphire lasers. Although the cost of these lasers have significantly dropped over time, THz photomixers provide an ideal alternative as they are not only cheap and ultra-compact but compared to other coherent THz sources, photomixers are the most widely tuneable [42]. The THz linewidth from photomixers depends directly on the linewidth of the optical excitation. Hence THz radiation with extremely high spectral purity and resolution can be achieved. This allows access to hyperfine spectroscopic features of samples which is not possible with conventional THz-TDS systems. Nevertheless, tuneablity of photomixers comes at the cost of relatively low output power compared to other THz sources.

This chapter discusses detailed design, fabrication and characterisation techniques for photomixer emitters employing a broadband log-spiral antenna and interdigitated electrode structure on a LTG-GaAs substrate. System dependencies such as the combined linewidth, frequency stability and piezoelectric transducer tuning of the two excitation diode lasers are characterised. A technique used to find the zero path delay of the system, along with a knife-edge measurement of optical beam spot used to excite emitters are also explained. Then an annealing temperature study of LTG-GaAs photomixers is described, in order to optimise the emission bandwidth of the photomixers. Furthermore, the carrier-lifetime of the emitters is also determined using a photocurrent correlation technique. The effect that the annealing temperature, the carrier lifetime and material resistance has on the frequency bandwidth of the emitters is explained and summarised. In addition, state-of-the-art photomixers (emitter and receiver) were bought from TOPTICA Photonics and their bandwidth is characterised. Finally, the TOPTICA emitter and receiver were used for the continuous-wave transmission spectroscopy of a $LiYF_4$-Ho crystal, which is used to demonstrate measurement of hyperfine features in the spectra.

4.2 Photomixer Design

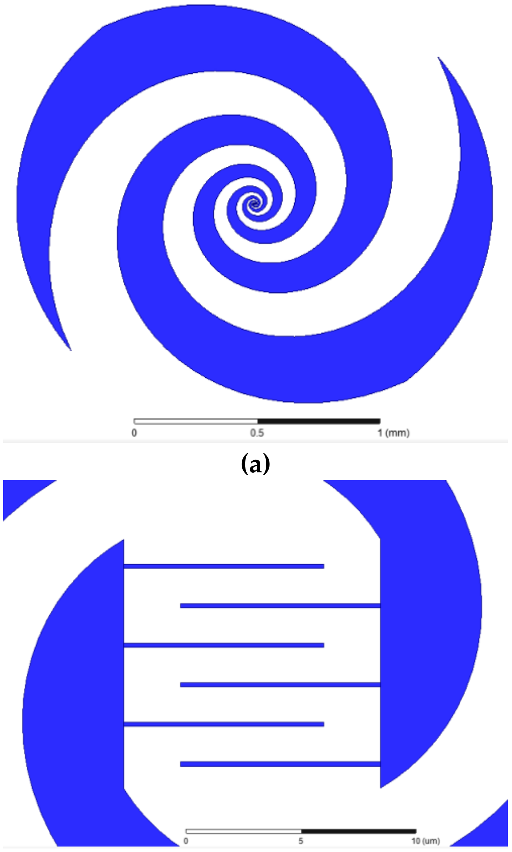

(a)

(b)

Figure 4.2: (a) Design of three-turn self-complimentary log-spiral antenna. (b) The central active area was 11.3 µm X 11.3 µm and consisted of three pair of interdigitated electrodes each 0.2 µm wide with 1.6 µm gap.

For this work, the design of photomixer emitter was an interdigitated electrode geometry centred in a three-turn self-complimentary broadband log-spiral antenna.

The antenna was designed using ANSYS® HFSS software package. It was a planar self-complimentary antenna design with logarithmic spiral arms with three complete turns. Log-spiral antenna design was chosen as the commercially purchased photomixer receiver also had log-spiral antenna structure. The spiral arms was designed using the equation $r = r_0 e^{a\varphi}$, where r_0 is the inner radius, φ is the angular position and a is the growth rate of the spiral arms. The growth rate can be represented as $a = \ln(\alpha)\,/2\pi$ where. α is the expansion ratio. For the antenna design used in this work, $r_0 = 8\,\mu m$ and $\alpha = 5$. The log-spiral designed had a central square-shaped 'active area' of 11.3 µm in length and outer radius of 1 mm. The antenna design has been shown in Figure 4.2 (a). Unfortunately, the whole photomixer structure could not be simulated as the resources required was more than 32 GB of computational memory (RAM). There was no standalone computer available with more than 32 GB memory. ANSYS® HFSS does allow high performance computing (HPC) using multiple computing nodes, but due to lack of technical support from ANSYS® to implement HPC, further simulation and optimisation of the antenna was not done.

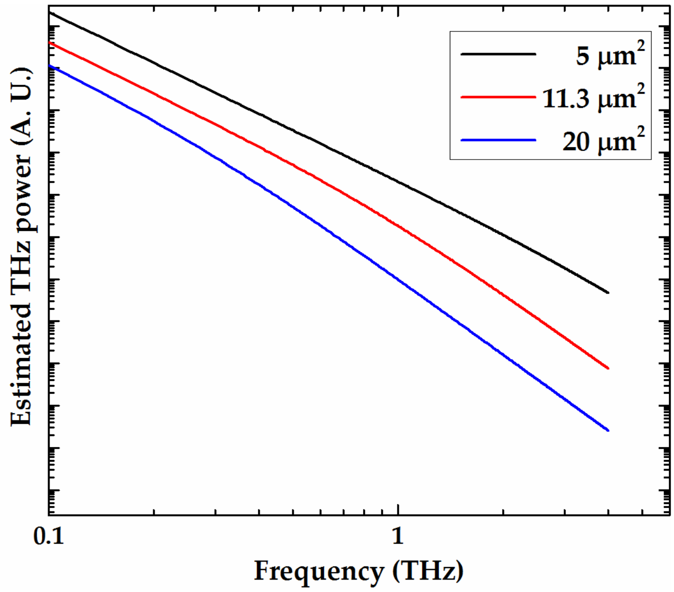

Figure 4.3: Estimated THz output power as a function of frequency for three different active area dimensions with each electrode geometry of 200 nm wide and 1.6 µm gap.

The 'active area' consisted of three pairs of interdigitated electrodes. Each electrode was 8.8 μm long and 200 nm wide. The spacing between each electrode was 1.6 μm. The electrode spacing used was close to the already optimised spacing (1.6–1.7 μm) for CW photomixers as reported in Ref. [199, 200]. In order to calculate the emitter THz power, Equation 4.5 suggests to minimise the width of the photoconductive gap and the active area for improved emission power. This holds true as long as the active area is similar to the laser spot size and can efficiently handle the thermal heating. Hence, the equation was used to calculate the frequency roll-off for devices of different active areas. Figure 4.3 shows the frequency roll-off for three different active areas. Theoretically, a -12 dB roll-off at frequencies >1 THz is expected using Equation 4.5. Although the 5 μm^2 active area has greater output power, the 11.3 μm^2 active area was used in the photomixer design as the minimum laser spot diameter was ~12 μm. The measurement of the laser spot size has been explained later in this chapter in Section 4.5.5.

Using Equation 4.2, the capacitance of the 5 μm^2, 11.3 μm^2 and 20 μm^2 active areas with electrode geometry of 200 nm wide and 1.6 μm gap was found to be 0.49 fF, 2.5 fF and 7.8 fF, respectively, using the relative permittivity of GaAs $\epsilon = 12.8$.

4.3 Fabrication of photomixers

Layer	**Material**	**Thickness (μm)**
1	SI-GaAs	500
2	$Al_{0.75}Ga_{0.25}As$	0.4
3	LTG-GaAs	2

Table 4.1: MBE layer structure of wafer L1148.

Photomixer emitters were fabricated using the same nanotechnology cleanroom facilities as mentioned in Chapter 2. The LTG-GaAs used in this work was grown on a 500 μm semi-insulating (SI) GaAs substrate, using the molecular beam epitaxy (MBE) technique. All the wafers were grown by Dr Lianhe H Li. The MBE layer growth structure of a typical wafer (L1148) used for this work has been provided by Dr Lianhe H. Li and is shown in Table 4.1.

LTG-GaAs was annealed ex-situ at temperatures ranging between 300–625° C. Broadband log-spiral antennas along with the interdigitated fingers were patterned using electron-beam lithography (EBL) and 5/100 nm Ti/Au was deposited using electron-beam evaporation. Optical lithography and e-beam evaporation was used to fabricate the contact pads. Finally the device was mounted on a printed circuit board (PCB) using silver conductive paint. A detailed explanation of the fabrication steps is described in the following sub-sections.

4.3.1 Sample cleaning and annealing

The maximum area covered by each log-spiral antenna was 2 mm x 1.7 mm. The LTG-GaAs wafer was diced into smaller substrate dimensions, depending upon the EBL window size used for patterning and the number devices patterned on a single substrate. The surface of the substrate was cleaned of contaminants and organic deposits by immersing it in a beaker of acetone placed in an ultra-sonic bath at 10% power for 10 minutes. It was then rinsed with IPA and blow dried using dry N_2 gas, followed by cleaning in a UV-ozone chamber for 10 minutes. After cleaning, the substrate was annealed at a desired temperature for 15 minutes using an AnnealSys rapid thermal annealer (RTA).

4.3.2 Electron-beam lithography and evaporation

After annealing, the substrate was once again cleaned of contaminants using acetone and IPA. The photomixer design was patterned using a JEOL JBX 6300FS EBL system. All processing extending from the pre-EBL sample preparation, to the post-EBL development of the sample was completed by Dr Mark C. Rosamond. Before loading the sample for EBL, it was coated with ZEP520A EB resist, spun at 4500 rpm for 40 seconds yielding a resist thickness of ~150 nm. It was then baked at 180° C for two minutes on a hotplate. The EBL for each sample took approximately ~40 minutes. After the EBL process, the sample was developed for one minute using ZED-N50 EB resist developer, rinsed with IPA and blow dried with dry N_2 gas. An optical microscope image of a sample after EBL and development is shown in Figure 4.4 (a). The orange-yellow coloured areas are resist covered, whereas the white area is the exposed substrate for metallisation.

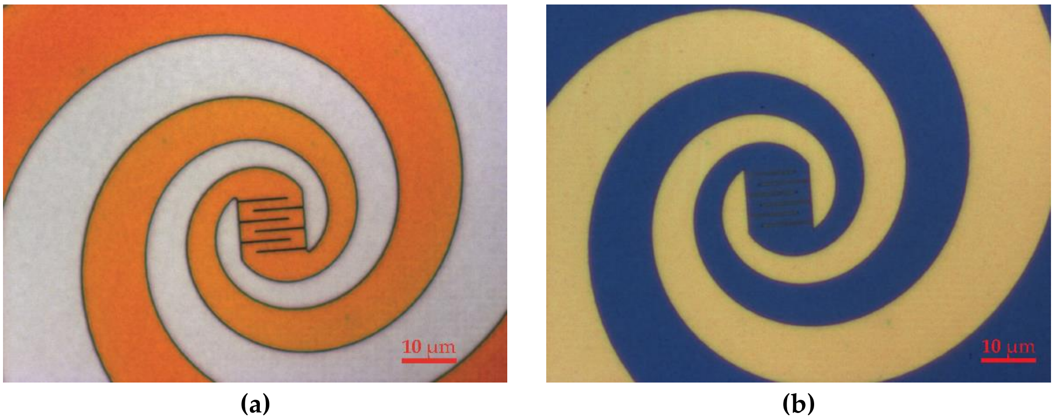

(a) (b)

Figure 4.4: Microscopy image of the sample after (a) e-beam lithography and development (orange area is unexposed resist) and (b) e-beam evaporation and lift-off (yellow is the metallised surface, LTG-GaAs substrate in dark-blueish colour).

The sample was metallised using an E-Beam evaporator to deposit 5 nm Ti and 100 nm Au. For lift-off, the sample was treated with Microposit remover 1165 heated at 75° C. Figure 4.4 (b) shows an optical microscopy image of a sample after lift-off.

4.3.3 Contact pad lithography and evaporation

After metallisation of the antenna and interdigitated fingers, the sample was cleaned using acetone in an ultra-sonic bath for one minute, rinsed with IPA and blow-dried using dry N_2 stream. The sample was coated with SHIPLEY® Microposit® S1813, a positive photoresist, spun at 5000 rpm for 30 seconds to obtain a resist thickness of ~1.2 μm and soft-baked at 115° C for one minute to evaporate excess solvents and harden the resist. The sample was exposed to UV radiation at 10 mW/cm^2 for three seconds using an optical mask aligner with a chrome-on-glass mask. It was then developed with SHIPLEY® Microposit® MF-319 for two minutes to define the contact pad region. E-beam evaporation was then used to deposit 5 nm Ti and 100 nm Au. The sample was then treated with acetone for lift-off. An optical image of sample is shown in Figure 4.5.

Figure 4.5: Optical image of the device with contact pads.

4.3.4 Mounting

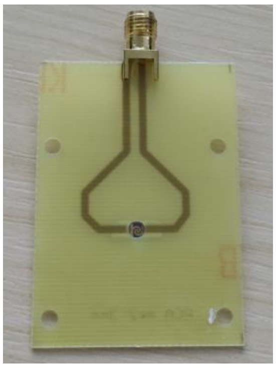

Figure 4.6: Optical image of a device mounted on a PCB with SMA connector.

The sample was cleaned with acetone and IPA before mounting face down on a PCB with copper tracks leading to an SMA connector and a 3 mm through-hole for optical illumination of the active area of the device. The contact pads were glued to the copper tracks using RS Silver Conductive Paint Adhesive. An optical image of a sample mounted on a PCB is shown in Figure 4.6.

4.4 Experimental configuration

State-of-the-art photomixers (emitters and receivers) based on GaAs were commercially purchased from TOPTICA Photonics. Response of emitters fabricated in-house was compared to the state-of-the-art TOPTICA emitter. The TOPTICA receiver was used throughout for coherent detection of signal. The experimental configuration used to characterise the in-house emitters were slightly different to the TOPTICA emitter as former was excited with free-space coupling of the radiation and latter was packaged as pigtailed fibre. The apparatus used in each case has been explained next.

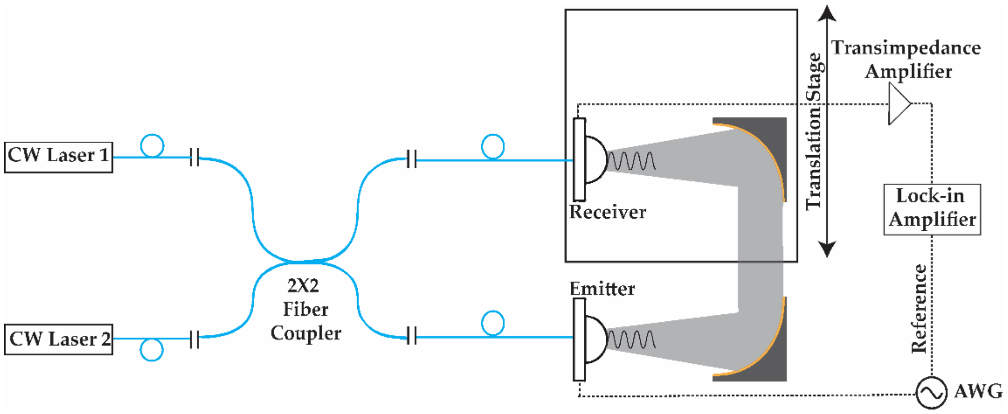

Figure 4.7: Schematic of TOPTICA photomixer characterisation apparatus. CW–continuous-wave, and AWG–arbitrary waveform generator. PM mating sleeves have been diagrammatically represented as two small parallel lines connecting fibres.

A schematic of the basic experimental configuration for characterisation of TOPTICA photomixers is shown in Figure 4.7. Two independent state of the art NEW FOCUS TLB-6700 Velocity continuous-wave external-cavity diode lasers (ECDLs), operating at a wavelength of ~780 nm were used as an optical excitation source. Each laser could be continuously tuned using a built-in DC motor and piezo-electric transducer within a range of ~16 nm. The DC motor allows course control of the emission wavelength, whereas the piezoelectric element was used for fine-tuning. Single mode (SM) Polarisation-Maintaining (PM) fibre was coupled to the laser output. Optical isolators and angled physical contact (APC) fibre connectors were built-in to avoid reflections into the laser cavity. The output power from the fibre connectors was measured using a THORLABS Fibre Optic Power Meter PM20CH. The optical power coupled out of the fibre was ~30 mW for each laser and linearly polarised.

The TOPTICA photomixers were designed for 780 nm excitation wavelength. They were packaged with a Si lens and FC/APC SM/PM pigtailed fibre. Radiation from both the ECDLs were mixed using a PM 2x2 fibre coupler with 50/50 output power ratio and the output ends, namely excitation and probe beams, were connected to the emitter and receiver respectively. The total optical power of each beam was ~20 mW. A pair of 3-inch-diameter gold-coated 90° off-axis parabolic mirrors were used for the collection, collimation and focusing of the generated CW-THz radiation from the emitter onto the receiver. The emitter was biased with a ±10 V 50% duty cycle square-wave modulated at 7.6 kHz using an Arbitrary Waveform Generator (AWG). As the commercial emitter was characterised by the manufacturer at 7.6 kHz, the same modulation frequency was chosen throughout all the experiments related with photomixers in this thesis. The output current from the TOPTICA receiver was amplified using an Electro-Optical Components, Inc. FEMTO DHPCA-100 variable gain high speed current amplifier. The output voltage signal was detected using a lock-in amplifier referenced at the emitter modulation frequency. The sinusoidal THz signal was sampled on the receiver by altering the time delay of the automated translation stage, effectively time delaying the incident

THz signal on the receiver relative to the probe beam. The unit of delay stage positions has been referred in terms of time rather than distance. This is the convention for TDS based systems. In CW systems, this simply sweeps the phase difference between the paths. The motion of the translation stage and data acquisition from the lock-in amplifier was controlled using a LabVIEW program courtesy of Dr Joshua. R. Freeman.

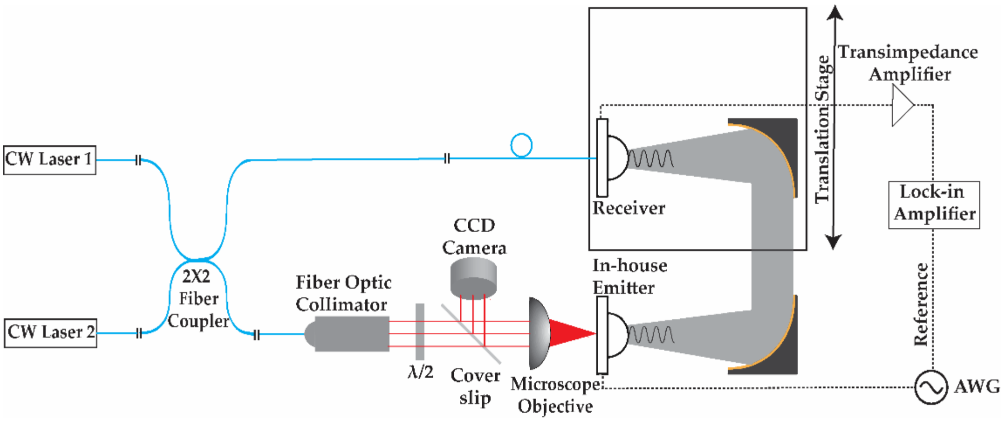

Figure 4.8: Modified photomixer characterisation apparatus used with the free-space 'in-house' emitters. $\lambda/2$–half-wave plate.

In the case of characterisation of the in-house photomixers, the experimental configuration was modified as shown in Figure 4.8. Unlike the fibre coupled TOPTICA emitter, the photomixers fabricated in-house were excited by optical beam in free-space. The TOPTICA emitter was replaced with the 'in-house' emitter, which was mounted on a PCB as explained in the previous section. The excitation beam was coupled through a 1 m PM PC/APC fibre optic patch cable designed for a centre wavelength of 780 nm. It was then connected to a THORLABS F220APC-780 fibre collimation package. The collimated excitation beam was focused onto the device active area using a 10x microscope objective lens with 0.25 numerical aperture, mounted on a translation stage to adjust the focal spot position. A half-wave plate was introduced in the path of the collimated beam to optimise its linear polarisation angle with respect to the device's active area geometry. Optimisation of incident beam polarisation has been mentioned further into this chapter in Section 4.6.1.2. The polarisation along the direction of electric field between the interdigitated fingers was found to generate maximum photocurrent and output signal amplitude. A CCD camera was used to align the focused optical beam onto the active area of the device. For this purpose, a cover slip was positioned at approximately 45° angle (see Figure 4.8) after the half-wave plate to allow the reflection from the device to be seen by the CCD sensor. An empty lens tube was mounted onto the camera to avoid ambient light saturating the sensor. An image of the device on the CCD camera is shown in Figure 4.9. A high resistivity hyper-hemispherical Si lens mounted on a two dimensional translating lens mount was placed behind the emitter to couple the generated radiation on the collection optics [196] and avoided total internal reflection of the emitted radiation from the semiconductor-air interface [197]. Both the parabolic mirrors, the probe beam and TOPTICA receiver, automated translation stage and the data acquisition electronics were the same as explained before.

Figure 4.9: CCD image of the device.

The TOPTICA emitter was simpler to align in comparison to 'in-house' emitters, as the fibre coupled excitation and Si lens positioning was already optimised within the package. Alignment of these photomixers was very time-consuming and tedious. In addition to the CCD device used for alignment, a Keithley 2400 series SourceMeter® unit (SMU) was used to apply a small DC bias and measure the photocurrent. The photocurrent was maximised by optimising the objective lens position and half-wave plate angle with respect to the device; the position of maximum photocurrent corresponded to optimum alignment with respect to the excitation beam. The device was connected to the AWG and the detected radiation amplitude was optimised by alignment of the hyper-hemispherical Si lens, sample position and receiver position. The Si lens was positioned to align its centre with the active area, enabling optimum out-coupling of the generated THz radiation. The sample was positioned as close to the focal spot of the parabolic mirror as possible to improve beam collimation. The receiver's position (including a built-in Si lens) was then finely adjusted to improve detection of the THz radiation. Initial alignment of the THz radiation was done at lower frequencies such as 100 GHz, before the frequency was gradually increased to optimize alignment for high frequencies. Optimisation was done by tweaking the emitter position in all the three dimensions and also fine adjusting the silicon lens for improved signal detection. Relatively high power and broad beam at lower frequencies eases the initial alignment the device. As the output beam get more directional at higher frequencies, fine tuning alignment is necessary for optimised detection of high frequency signals. The alignment procedure had to be repeated every time a device was placed in the system. All the characterisation measurements mentioned in this chapter, using either the TOPTICA emitter or in-house emitter, has been done under normal atmospheric conditions.

Small gaps in the active area design of the photomixers make them vulnerable to even the slightest amount of electrostatic discharge (ESD) across the terminals. Great care was therefore taken to avoid ESD while making electrical connections to the photomixers. Grounding straps were always worn before any physical contact was made with the device. For TOPTICA photomixers, the optical fibre connections were done before connecting them electrically. The reverse of the procedure was followed to disconnect the device. In this case, the electrical connection was replaced by a 50 Ω termination and then the optical fibre was disconnected. As mentioned earlier, these precautions were taken to avoid damage of the active area due to ESD.

4.5 Experimental considerations

Before characterising the photomixers, basic system parameters such as the laser's linewidth and frequency drift needed determining. In addition, the effect of the piezoelectric transducers on the emission wavelength of the combined diode laser radiation was measured. Measurements were also performed to help control the THz path length, in order to achieve zero path delay between the incident THz signal from the emitter and the optical beating on the receiver. For the in-house free-space photomixers, the spot-size of the optical beam was also characterised using a knife-edge technique.

4.5.1 Combined laser linewidth

As two independently running lasers were used to excite the photomixers, characterisation of their combined linewidth and frequency drift was important. Any frequency drift/jitter of the lasers would be directly reflected as drift in the frequency difference and therefore result in a change in the emission frequency of the emitter during measurements.

The experimental configuration used to characterise frequency drift in the lasers is shown in Figure 4.10 (a). A 2x2 fibre coupler was used to combine the CW-radiation from both diode lasers. Radiation was collimated through a fibre optic collimator (FOC) and was directed towards a THORLABS Si based photodiode using a microscope objective. The other unused output arm of the 2x2 fibre coupler was connected to a fibre optic light trap for safety and also to reduce any back reflections. The output from the photodiode was measured using an electrical spectrum analyser (ESA). A short 50 Ω coaxial cable was used to connect to the ESA along with a 50 Ω termination at the ESA input, as recommended by the manufacturer.

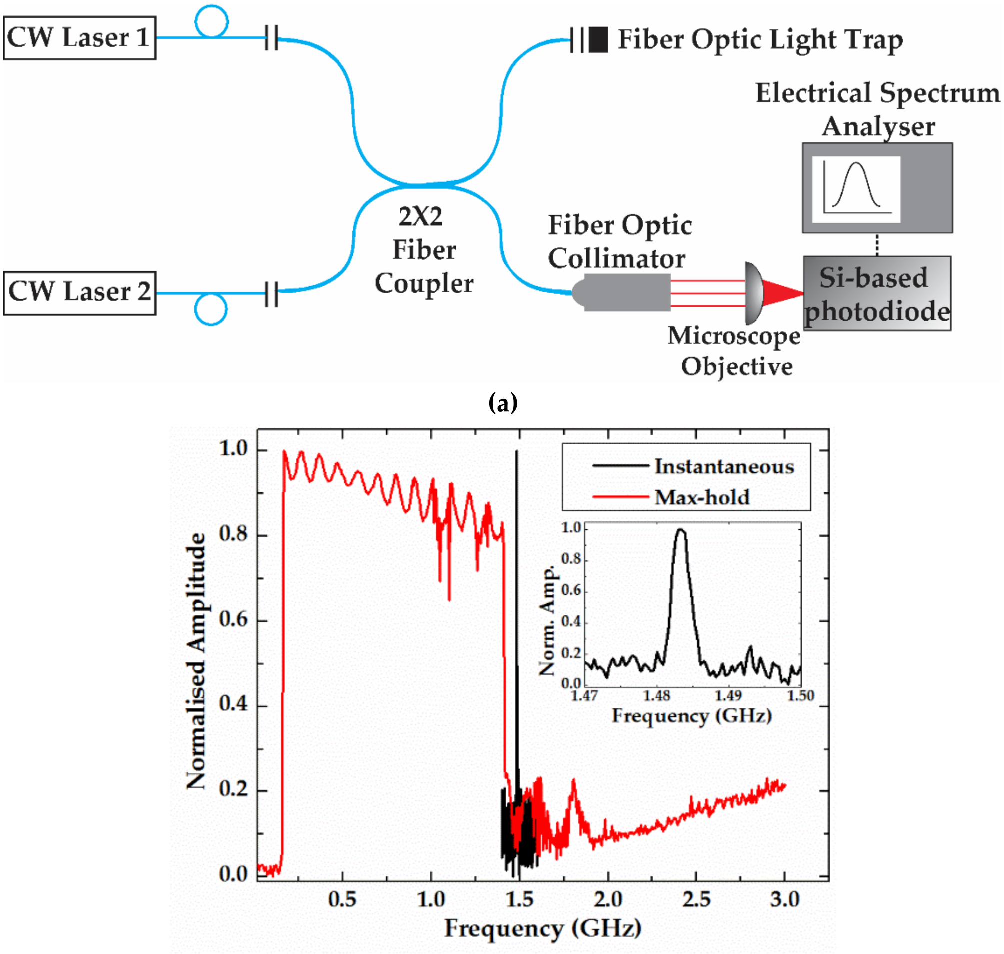

(a)

(b)

Figure 4.10: (a) Schematic of experimental apparatus to measure the combined linewidth of the two ~780 nm diode lasers. (b) Linewidth obtained by beating of the two laser diodes on a photodiode. Linewidth obtained using max-hold operation of the spectrum analyser for a duration of ~3 minutes shown in red (RBW: 6.5 MHz). A high resolution instantaneous linewidth shown in black (RBW: 430kHz). (Inset) Instantaneous linewidth with magnified frequency axis.

The bandwidth of the photodiode was 5 GHz but the measurement was limited by the 3 GHz bandwidth of the ESA. The difference in the laser frequency was carefully tuned close to 1.5 GHz, the full range centre frequency of the ESA. The recorded spectra was normalised and is shown in Figure 4.10 (b). Spectra obtained using the max-hold function of the ESA for approximately 3 minutes are shown in red, measured with a resolution bandwidth (RBW) of 6.5 MHz. A gradual drift of ~1.5 GHz was observed over a time duration of 3 minutes. This was due to the combined frequency drift of the lasers used. The frequency drift manifested in the lasers could be originating due to many reasons such as thermal or vibrational noise. The origin of oscillations in amplitude of the red curve is unknown and requires further investigation for precise determination. A high resolution (RBW: 430 kHz) instantaneous shot of the spectra is shown in black. The inset shows the instantaneous spectra enlarged. In this case, the FWHM of the instantaneous spectra was found to be 2.75±0.97 MHz. The instantaneous measurement was directly dependent on the linewidth of the individual lasers and hence provided much smaller frequency jitter.

As the lasers were used for emitter bandwidth characterisation, the frequency drift was not of a major concern as short scan duration (~1 minute) per frequency point was used with frequency steps as large as ~25 GHz.

4.5.2 Zero path delay

The combined path length of the excitation beam and the generated THz beam must be equal to that of the probe beam on the receiver, in order to achieve a zero phase difference between them. Since the detection system behaves like an interferometer, a finite path difference would cause quasi-sinusoidal oscillations of the signal amplitude on the receiver, as the heterodyne frequency changes [196] (see Equation 4.1).

To achieve a zero path delay, the heterodyne frequency was arbitrarily chosen away from the water absorption lines, and tuned from 500–520 GHz using the piezo-electric transducer of a laser and the signal from the lock-in amplifier was recorded. This was done at each delay stage position. The signal recorded as a function of heterodyne frequency at various delay positions is shown in Figure 4.11. The path difference can be calculated from the period of the oscillations shown in the frequency domain in Figure 4.11 [196]. The period of the oscillations increases as zero path difference is achieved (see blue curve in Figure 4.11).

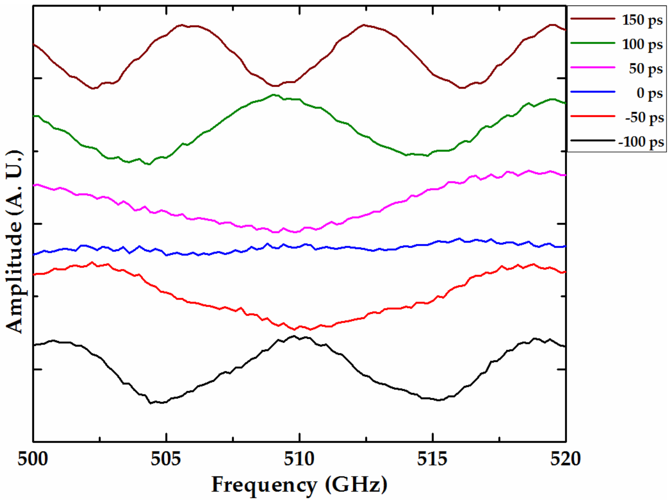

Figure 4.11: Detected signal against heterodyne frequency at different path delays. Zero path delay has been represented by 0 ps (blue line).

The lasers used in this work have finite linewidth and significant frequency noise. Hence having a non-zero path delay would directly translate the frequency jitter into amplitude noise detected on the receiver (see, for example, the oscillations in Figure 4.11 at non-zero path delay). Zero path delay was found in a similar way for all experiments mentioned in this thesis which used both emitter and receiver photomixers.

4.5.3 Laser stability scan

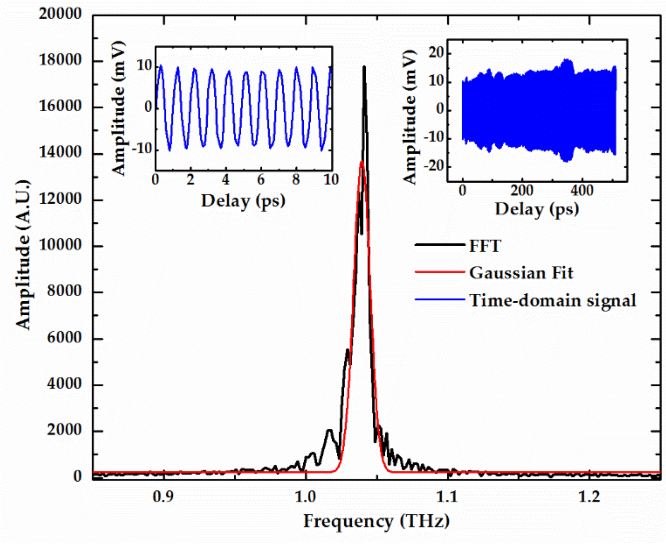

(a)

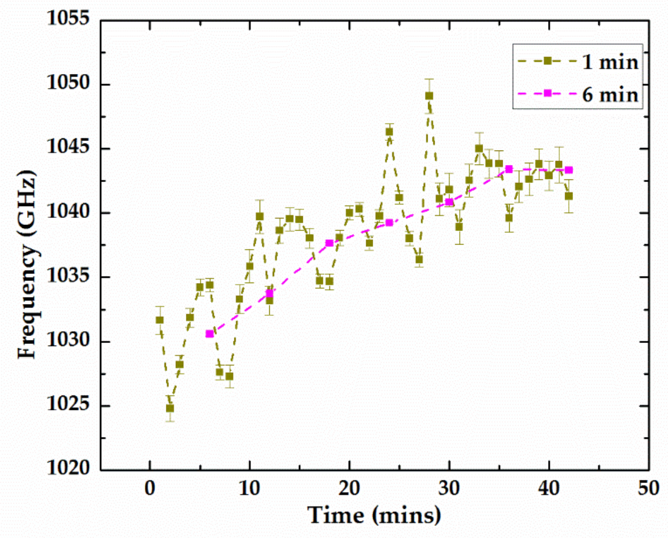

(b)

Figure 4.12: (a) FFT of ~500 ps long scan at ~1 THz heterodyne frequency (black), Gaussian fit to the FFT (red) has a FWHM of ~13.7 GHz. (Inset-right) Time domain scan of the THz emission over a range of 500 ps. (Inset left) A small section of the time-domain scan showing detected sinusoidal fringes. (b) Fitted frequency of 1 minute and 6 minutes slices of the 42 minutes long scan plotted against time.

Another experiment was performed using the TOPTICA emitter and receiver to measure the frequency drift of the diode lasers, achieved by mapping the emitted CW-THz for a significant period of time. For this experiment the heterodyne frequency was arbitrarily chosen close to 1 THz. The delay stage was scanned at a step of 100 fs over a range of 500 ps and the lock-in signal was recorded at each step, as shown in the right inset of Figure 4.12 (a). The total time taken for this scan was ~42 minutes. Figure 4.12 (a) shows the Fast Fourier Transform (FFT) of the signal. The peak of the FFT was close to 1 THz and a Gaussian fit (solid red line) had a FWHM of 13.7 GHz. This represented the frequency drift of the lasers over the time span of ~42 minutes. The continuous-wave emission detected over a shorter time duration is shown in the left inset of Figure 4.12 (a).

The 42 minutes long scan was sectioned into durations of 1 minute and 6 minutes. MATLAB was used to perform a single frequency sine fitting to each section. The fitted frequency as a function of time for both 1 minute (dark yellow) and 6 minute (magenta) sections is plotted in Figure 4.12 (b). The error bars represent 95% confidence bound of the fitted frequency. Slow drift in the heterodyne frequency of ~20 GHz can be observed over 42 minutes which agrees well with the combined laser frequency jitter of ~1.5 GHz over 3 minutes (see Section 4.5.1).

Such high combined laser frequency jitter would be a problem if reliable measurements were to be performed for longer time durations. For emitter bandwidth characterisation, ~25 GHz heterodyne frequency steps were used with short scanning range to minimise effect of the frequency jitter.

4.5.4 Piezo-electric voltage characterisation

A full range scan of the piezoelectric transducer was performed to characterise the fine frequency tuning range, using both the TOPTICA emitter and receiver. Since the measurement was done in an unpurged environment, the fine tuning range was determined by scanning across a known waterline as a reference. The dip in signal amplitude would correspond to the water absorption and the frequency tuning range of transducers could then be determined.

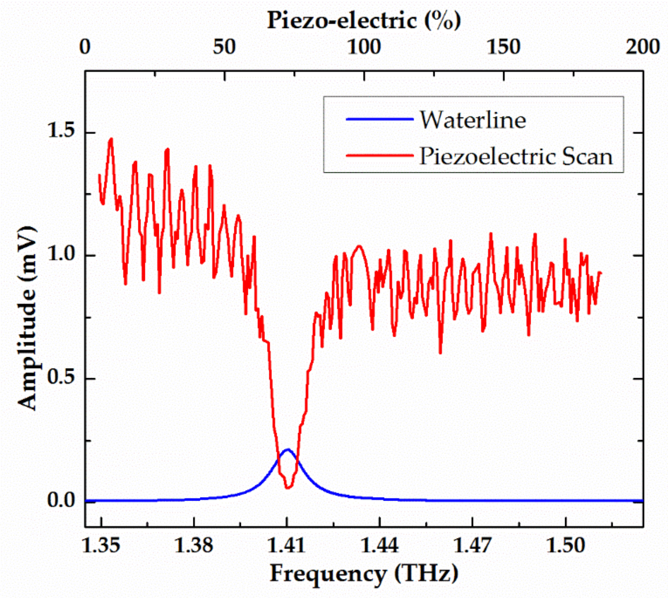

Figure 4.13: Fitted amplitude as function of piezo-electric scan has been shown as red line. Waterline at ~1.41 THz shown as blue line with scaled amplitude.

The heterodyne frequency was coarsely set close to a waterline at ~1.41 THz. The piezoelectric transducer was stepped at 0.7% of the full tuning range. At each step, the delay stage was scanned with a small range of ± 2.5 ps from the zero path delay position to sample the CW signal. This was done to minimise any effect of frequency drift due to instability of lasers as mentioned earlier. The fitted signal amplitude, plotted as a function of the piezoelectric scan (top axis), is shown as the solid red line in Figure 4.13. As two piezo-electric transducers were scanned across their full range, the piezo-electric axis is shown as 0–200%. The reference water absorption line has been marked in blue and its amplitude has been arbitrarily scaled to fit on the same amplitude axis. The water absorption data was taken from an online database HITRAN [215] and calculated by Dr Joshua. R. Freeman. To obtain the absolute heterodyne frequency for each step in full piezoelectric scan, the fitted frequency was determined for the first and last piezo-electric settings. The frequency axis was then scaled to fit the whole scan range and also to match the measured absorption dip to the waterline.

Almost 160 GHz of frequency tuning was possible from both the piezoelectric transducers of the two diode lasers. This was close to the expected tuning range as per the ECDL manufacture specifications. Scanning of waterlines around 2 THz also produced agreeable results.

4.5.5 Knife-edge measurement

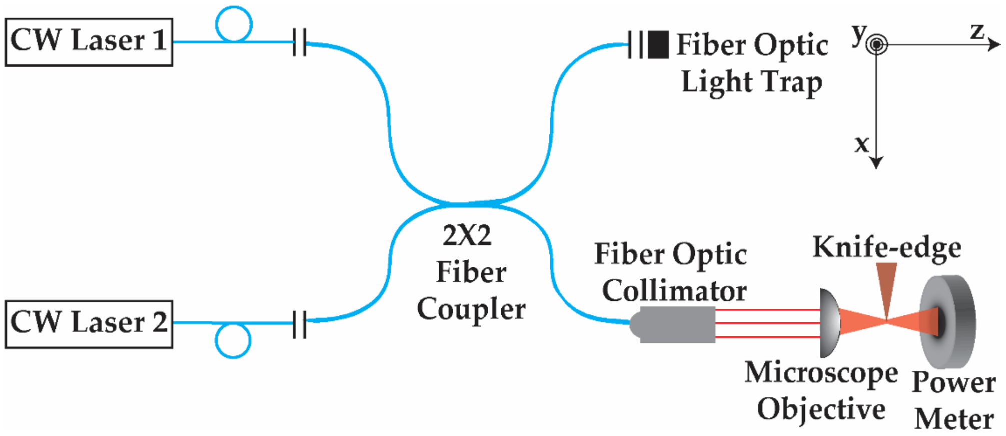

Figure 4.14: Schematic of focused beam waist measurement using knife-edge technique.

The focused spot size of the excitation beam was measured before characterising the free-space in-house photomixers. Focussing the optical radiation into the active area of the device would generate more photocarriers and hence higher output signal amplitude. Therefore, measurement of the optical spot size was necessary to make sure the spot is small to cover the active area. As mentioned earlier, a 10x microscope objective with a 0.25 numerical aperture was used to focus the collimated beam from the FOC. A surgical scalpel blade was used as a knife-edge and was mounted on a XYZ manual translation stage. A compact motorised actuator was used to scan through the beam at a step size of 30 μm. A power meter was placed directly behind the knife-edge to record the power at each actuator position. The experimental configuration is shown in Figure 4.14. In this case the probe arm was attenuated using a fibre optic light trap.

For a Gaussian shaped beam, a plot of measured power against knife-edge position would result in a curve known as Gauss error function [216]. A complimentary error function [217, 218], $P(x) = \frac{P_0}{2}\left\{1 - erf\left[\frac{\sqrt{2}(x-x_0)}{w_x}\right]\right\}$ can be used to fit the measured data, in which P_0, x_0 and w_x are the total absolute power, centre coordinate and $1/e^2$ half-widths of the beam respectively. The knife-edge position has been represented as x. A more rigorous mathematical derivation has been explained in Ref. [217]. Through fitting measured data to this function, the minimum spot size w_x can be determined by performing a knife-edge measurement at different z-positions.

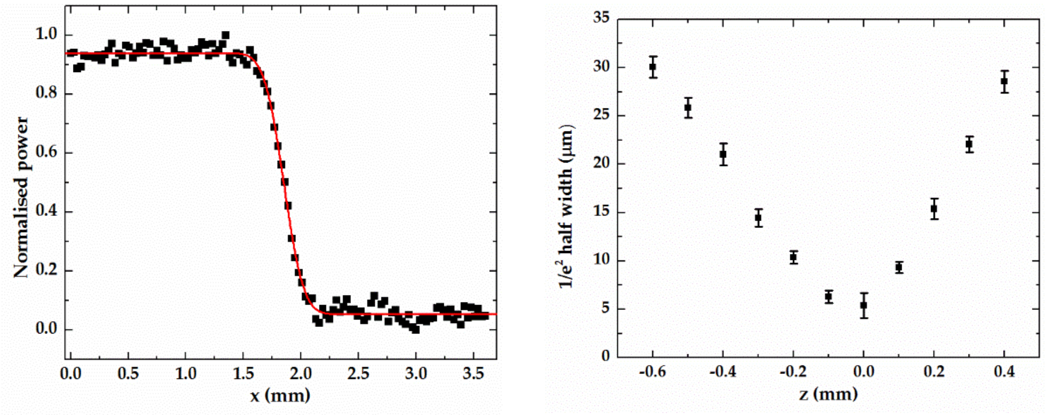

(a) **(b)**

Figure 4.15: (a) Normalised intensity profile of knife-edge measurement (dots) and fitted complimentary error function (red solid line) (b) Calculated $1/e^2$ half-width w_x against distance from the focal spot z. Error in fitting value w_x has been represented by error bars.

The total power of the beam P_0 was measured on the power meter by unblocking the beam completely. The normalised power measured as a function of knife-edge position along the x-direction, for one specific z-position, is shown in Figure 4.15 (a). Fitting of an adapted complimentary error function is shown as the solid red line. Parameters x_0 and w_x were obtained from the fit. A constant C was introduced to account for the non-zero measured power when the beam was completely blocked. The modified equation can be expressed as $P(x) = \frac{P_0}{2}\left\{1 - erf\left[\frac{\sqrt{2}(x-x_0)}{w_x}\right]\right\} + C$.

The knife-edge measurements were then repeated at a step of 0.1 mm along the z-direction to find the minimum spot size. The minimum spot size of the excitation beam in the x-direction was found to be w_x=5.4±1.3 µm as shown in Figure 4.15 (b). A similar measurement was carried out to determine the minimum spot size along the y-direction and it was found to be w_y=6.63±1.1 µm. The characterisation of beam spot sizes has been done several times within this thesis. A similar technique as mentioned here has been followed.

4.6 Study of annealing temperature

In low temperature growth of GaAs, excess arsenic causes formation of point defects. These point defects act as trap centres of conduction band electrons and causes reduction in carrier lifetime of the material to as low as 90 fs [79, 200]. This also causes low resistivity of the materials due to "hopping conduction" between the trap centres [219]. The growth temperature cannot be lowered invariably as too low temperature or too high arsenic pressure can cause stacking faults and pyramidal defects due to excess strain on the crystal lattice [220].

For too short carrier lifetimes, modulation of conductivity will not be possible due to low carrier density. Annealing of LTG-GaAs provides the thermal activation energy for reduction of point defects by forming metallic precipitates. This causes not only increase in carrier lifetime but also material resistivity. Increase in material resistivity allows higher bias voltage to be applied and hence increase in the output radiation from emitters. For a given annealing temperature, a thermal equilibrium is reached in defect concentration with time [200]. Annealing studies of LTG-GaAs have previously been reported to optimise the resistance and carrier-lifetime for photomixers [200, 219]. It should be noted that too high carrier lifetime (longer than beat period) is also not desirable as it was cause unnecessary heating of the device due to accumulation of electrons and hence huge drop in output power [200].

As annealing of LT-GaAs changes critical material parameters such as carrier-lifetime and resistivity, it eventually affects the bandwidth of the photomixers. In this section, material parameters such as dark resistance, photocurrent and photomixer bandwidth is studied for ex-situ annealing temperatures in the range of 500–625° C. At the annealing temperature optimised for highest bandwidth, photomixer frequency response was measured from three near identical LTG-GaAs wafers. The material with highest bandwidth is compared with the state-of-the-art emitter from TOPTICA Photonics.

4.6.1 In-house emitters

In the annealing study, samples from same LTG-GaAs wafer (wafer number L1148) were used to fabricate identical photomixer design. As already mentioned in the Section 4.3, the samples were first annealed at the desired temperature for 15 minutes under a nitrogen purged environment before carrying out further processing steps to fabricate the photomixer emitter.

4.6.1.1 Dark resistance and photocurrent

Initial characterisation of all the in-house fabricated photomixing emitters included measurements of current, with and without optical illumination, known as photo and dark current, respectively. The SMU was used to bias and measure the current flowing through the in-house emitters. They were not biased more than 5 V as it risked damaging the device.

Attempts made to measure resistance directly from a standard multimeter were unsuccessful as the process damaged the active area of the device. Most likely this was due to the high amount of current injected into the device from the multimeter terminals causing it to blow up. Dark currents from samples annealed at different temperatures were measured using SMU at a constant bias of 2 V. Therefore, the dark resistance was calculated and is shown as a function of annealing temperature in Figure 4.16 (a). As expected, the dark resistance increases with annealing temperature due to precipitation of the excess arsenic trapping centres. Devices annealed higher than 575° C does not show significant variation in the dark resistance as such high temperatures removes the point defects completely. In Ref. [200], similar observation of saturation in dark resistance was made but at a slightly lower annealing temperature of 550° C. The temperature difference could be due to the calibration issue of the RTA used for annealing.

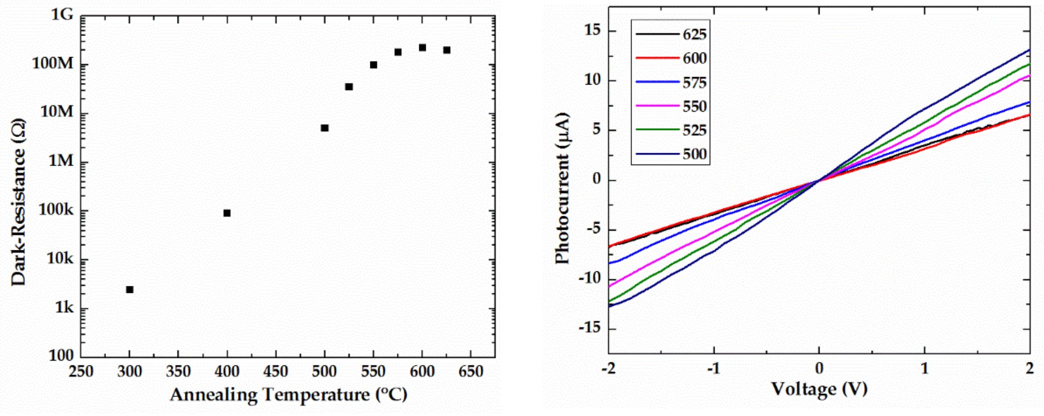

(a) **(b)**

Figure 4.16: (a) Dark resistance and (b) photocurrent-voltage sweeps of emitters at different ex-situ annealing temperature.

For photocurrent measurement, the optical excitation beam was aligned to the active area of the in-house emitters as already mentioned in Section4.4 (see experimental configuration in Figure 4.8). Under illumination, the photocurrent generated was dependent on the polarisation of the incident excitation beam. Polarisation dependence is further explained in the following subsection (see Section 4.6.1.2). For each device the photocurrent was maximised by optimising the polarisation angle of the excitation beam. The focus of the microscope objective was also tweaked to improve photocurrent. The total incident optical power was ~18.5 mW.

As samples annealed at 300° and 400° C had typically very low dark resistance, there wasn't significant difference between the measured dark and photocurrent values. Hence optimising the alignment of the excitation beam to the active area was very difficult. Attempts were made to align these samples by optimising the signal detected at low heterodyne frequency such as 100 GHz, but the signal was very noisy (0.1 mV). It was just above the noise floor of the system (~0.04 mV). No emission was observed at frequencies above 130 GHz. As a result, these samples were excluded from any further measurements due to very high background noise caused by the low material resistivity at such low annealing temperatures. Photocurrent-voltage sweeps for samples annealed between 500–625° C have been shown in Figure 4.16 (b). The decrease of photocurrent with an increase in annealing temperature is due to the increase in material resistance.

The active area of the photomixer was pairs of interdigitated fingers spaced at 1.6 μm having a width of 0.2 μm. Two iterations of the active area were fabricated, one with two pairs and the other with three pairs of interdigitated fingers with the same antenna design as shown in Figure 4.17 (a) and (b) respectively. Emitters with three pairs of electrodes performed better in terms of signal amplitude, bandwidth and photocurrent. The comparison of photocurrent and bandwidth from both two pairs (black line) and three pairs (blue line) electrode designs on LTG-GaAs wafer L1092 are shown in Figure 4.17 (c) and (d) respectively. Method used to measure bandwidth of the emitters has been explained later in Section 4.6.1.3. As a result the three pair electrode design was used for all the following measurements reported in this chapter using in-house emitters. For the dark resistance and photocurrent measurements shown previously in Figure 4.16, the three pair interdigitated photomixer design was used.

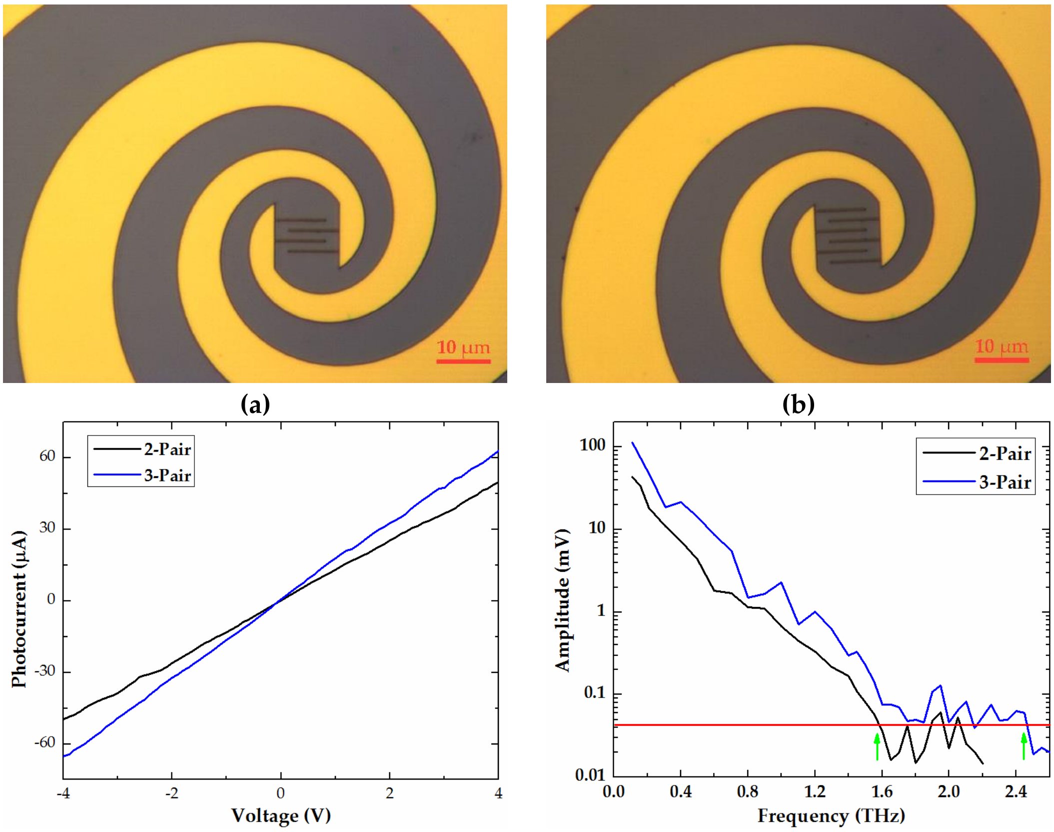

(a) (b)

(c) (d)

Figure 4.17: Microscope image of the active area of the photomixers fabricated with (a) two pair and (b) three pair of interdigitated electrodes and their (c) photocurrent and (d) bandwidth comparison.

4.6.1.2 Polarisation dependence

The measured photocurrent and emitted signal were dependent on the incident polarisation angle of the excitation light with respect to the electrode geometry. A half-wave plate was used to change the polarisation angle of the linearly polarised excitation beam.

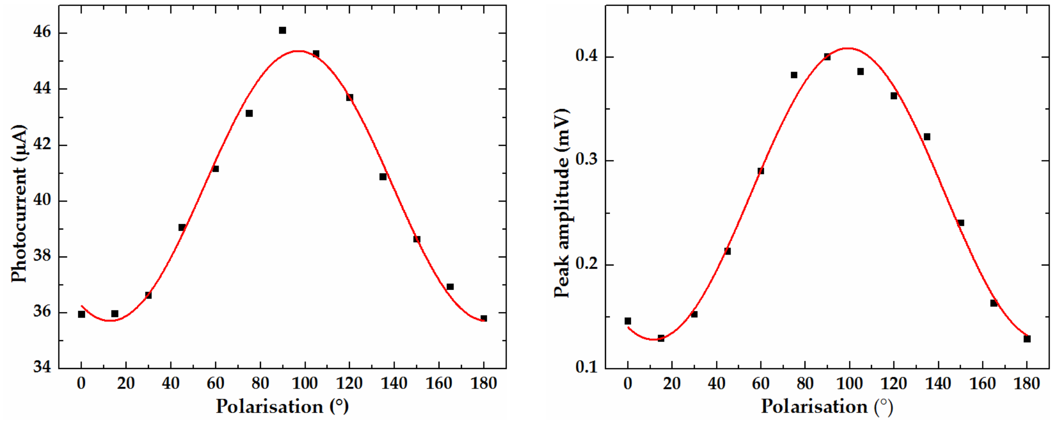

(a) **(b)**

Figure 4.18: (a) DC photocurrent measured at 5 V emitter bias as a function of half-wave plate angle. (b) Peak detected signal on the lock-in amplifier at 500 GHz as a function of half-wave plate angle. Polarisation of excitation beam parallel and orthogonal to electrode geometry has been represented as 0° and 90°, respectively. Sinusoidal fit has been represented as red line.

Polarisation dependence measurements were done at an arbitrarily chosen heterodyne frequency of 500 GHz using a three-pair electrode emitter fabricated on wafer L1092. Figure 4.18 (a) shows the change in photocurrent as the polarisation angle of the incident optical beam is changed in steps of 15° (black dots). To achieve this, the half-wave plate was turned with a step size of ~7.5°, which was equivalent to the 15° change in the polarisation angle. Polarisation parallel and normal to the electrode geometry has been marked as 0° and 90°, respectively. Figure 4.18 (b) shows the change in signal amplitude as a function of polarisation angle. The signal amplitude showed a similar dependence on polarisation angle as the photocurrent. In both cases, data was in good agreement with a sinusoidal fit (shown as red lines in Figure 4.18). The optical radiation is coupled more efficiently into the photoconductive material using perpendicular polarisation as compared to parallel polarisation. The dependence of polarisation on metal-semiconductor-metal structures have been reported in Ref. [221]. With the electrode finger dimensions comparable to optical wavelength, there exists resonance between the orthogonally polarised optical radiation and the MSM geometry. As a result of improved coupling and higher quantum efficiency, higher photocurrent and THz signal was measured for perpendicular polarised excitation radiation.

4.6.1.3 Bandwidth measurements

The experimental configuration used for measuring the bandwidth from the in-house emitters is already shown in Figure 4.8. For each measurement the heterodyne frequency was tuned in steps of 25 GHz unless otherwise stated. The TOPTICA receiver was used for coherent detection of the emission frequency. An automated translation stage was scanned close to the zero path delay at a step size of between 0.01–0.5 ps, depending upon the heterodyne frequency. The detected signal was amplified at a transimpedance gain of $10^7\ V/A$ with 1.8 MHz amplifier bandwidth. A 100 ms time constant within the lock-in amplifier was used to measure the signal at each translation stage position. Sine curve fitting was performed on the detected sinusoidal waveform using MATLAB. The frequency and amplitude were extracted as fitted parameters. Emitters were characterised in terms of their total bandwidth. The bandwidth was defined as the frequency at which the measured signal is just above the noise floor (NF) of the system. Emitters were biased with a 50% duty cycle square wave modulated at 7.6 kHz using the AWG.

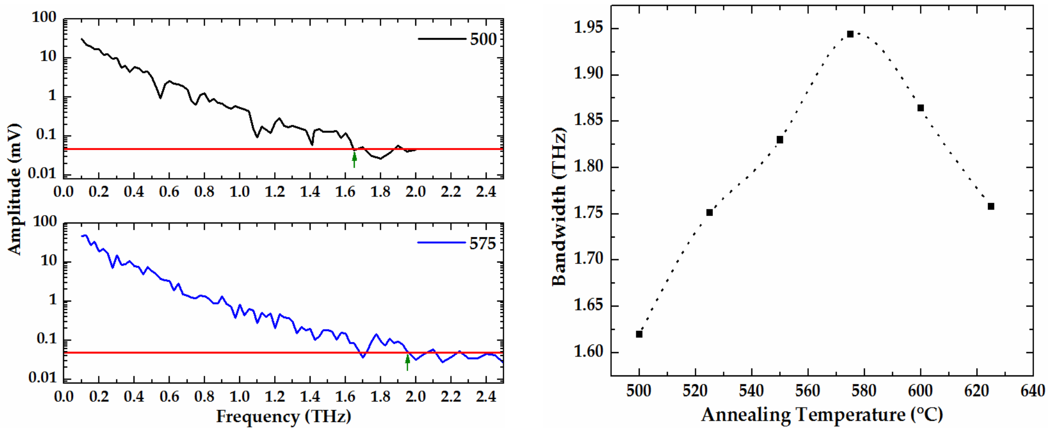

(a) (b)

Figure 4.19: (a) Comparison of fitted amplitude as a function of heterodyne frequency for 500° and 575° C annealed devices. Noise floor marked in red and maximum measured frequency marked with a green arrow. (b) Comparison of maximum bandwidth obtained at ex-situ annealing temperature ranging from 500–625° C. Image adapted from Ref. [222].

The emission bandwidth of the emitters at each annealing temperature was measured at a bias of 5 V. Exemplary frequency spectra from 500° and 575° C annealed emitters are shown in Figure 4.19 (a). The noise floor of the system was determined by measuring the lock-in value when the emitter was turned off. It was due to the noise from the receiver and was typically ~0.05 mV. For signals measured above the stated maximum bandwidth (green arrows mark the maximum bandwidth), the fitted frequencies were unrealistic values. In addition the FFT of those signals did not suggest the presence of any heterodyne frequency. The maximum measured bandwidth is plotted against annealing temperature in Figure 4.19 (b). As can be seen, devices annealed at 575° C exhibited the maximum bandwidth. With increase in annealing temperature, the material becomes more resistive and hence reduces the dark current. This effectively reduces the background noise which improves the photomixer performance. On the other hand, increase in annealing temperature also increases carrier lifetime of the material, leading to poor performance at higher frequencies. Hence, a 'sweet spot' on this curve was present due to a compromise between low background noise (dark current) and carrier-lifetime of the material. The measurement of carrier-lifetimes is explained in Section 4.7. Since these measurements were done at a constant 5 V bias, devices annealed at 600° and 625° C had photocurrents lower than that of 575° C, due to have greater resistivity. Therefore, the bandwidth of 600° and 625° C devices were also measured at same photocurrent value as that of the 575° C device at 5 V bias. However, there was no significant improvement in bandwidth.

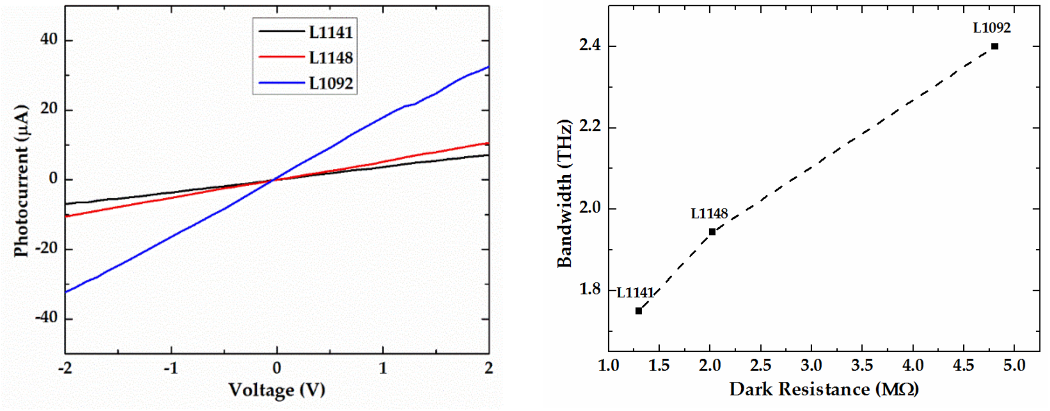

(a) (b)

Figure 4.20: (a) Comparison of photocurrent sweeps for wafers L1092, L1141 and L1148 annealed at 575° C under similar incident optical power of 18.5 mW. (b) Bandwidth comparison different materials.

Having optimised the ex-situ annealing temperature at 575° C, emitters were fabricated on nominally identical LTG-GaAs wafers grown using MBE and annealed at 575° C. Measured photocurrent as a function of applied bias for emitters fabricated on wafers L1141, L1148 and L1092 are shown in Figure 4.20 (a). L1148 was the wafer used for the annealing temperature study discussed above. Figure 4.20 (b) shows the maximum measured bandwidth against measured dark resistance for the emitters fabricated on different materials. The applied bias was kept constant at 5 V for all emitters. Clearly, wafer L1092 has better performance as compared to the others in terms of both photocurrent and bandwidth. It also has significantly higher dark resistance which leads to low background noise and hence improved bandwidth. The visible difference in these wafers was that L1141 and L1148 were grown on a double side polished SI-GaAs substrate whereas L1092 was grown on a single side polished SI-GaAs substrate. Therefore, there could be a significant temperature difference during the MBE growth of LTG-GaAs epilayers on the two different kind of substrates.

4.6.2 State-of-the-art TOPTICA emitter and comparison with in-house emitter

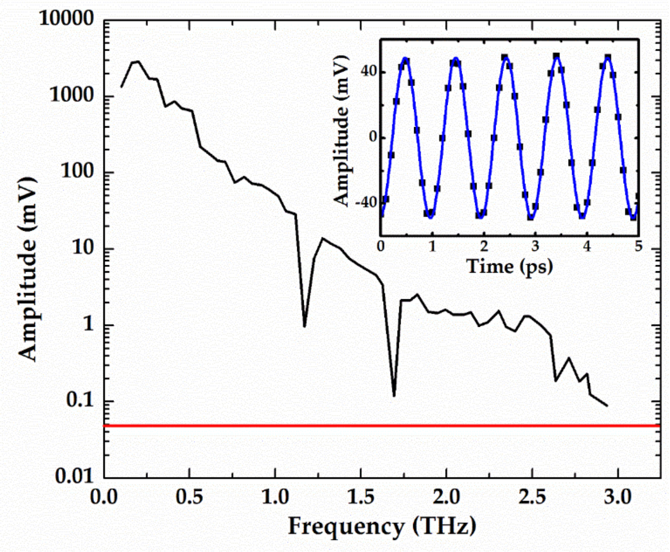

Figure 4.21: Fitted amplitude as a function of frequency for TOPTICA emitter biased at ±10 V and 20 mW optical excitation power. Noise floor shown in red. (Inset) Coherently detected time-domain photomixer response at 1 THz heterodyne frequency (black dots). Single frequency sinusoidal fit has been represented by blue line. Amplitude and frequency obtained as free fitting parameters.

The experimental configuration used to measure bandwidth from the TOPTICA emitter is already shown in Figure 4.7. The TOPTICA emitter was biased at ±10 V with an excitation beam power of ~20 mW. The measured sinusoidal waveform at a frequency of 1 THz is plotted as a function of delayed THz beam (black dots) in the inset of Figure 4.21. The fitted sine wave is shown in blue. The dependence of the fitted amplitude on measured frequency is plotted in Figure 4.21 as a solid black line. The NF of the system has been marked as a red line and was defined as the maximum lock-in signal with heterodyne frequency >6 THz. There was no significant change in the NF when measured with the emitter bias turned off. Any dips in the amplitude are a result of water absorption lines. Not all water lines were resolved, as the frequency was scanned in steps of 25 GHz. Also scanning a waterline with coarse frequency tuning was not possible due to the slow drift in the heterodyne frequency. The bandwidth of the TOPTICA emitter was found to be > 3 THz and is consistent with the manufacturer's specifications.

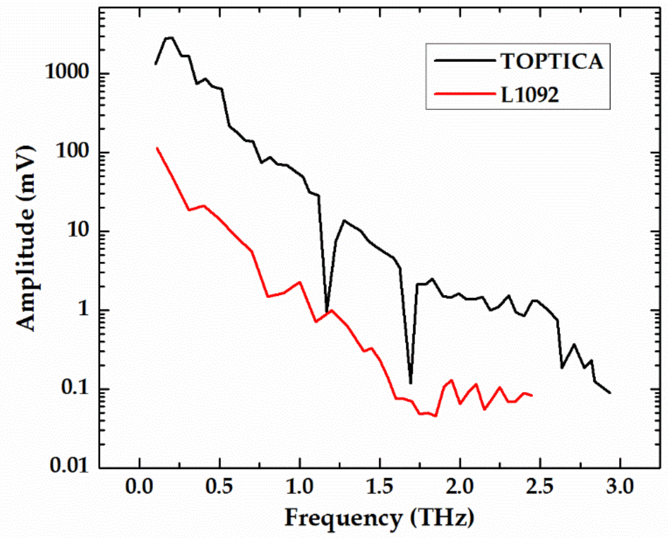

Figure 4.22: Bandwidth of TOPTICA emitter and L1092 emitter.

The frequency response of the emitter purchased from TOPTICA and the in-house emitter fabricated on L1092 has been compared. L1092 was chosen for comparison as it had better bandwidth as compared to devices fabricated on other materials. The fitted amplitude as a function of fitted frequency for the TOPTICA emitter (black line) and the L1092 in-house emitter (red line) are shown in Figure 4.22. A conservative bias of 5 V was applied to the in-house emitter for characterisation, whereas the TOPTICA emitter was biased at ±10 V. The photocurrents or dark currents cannot be directly compared as applying DC bias to the TOPTICA emitter was not recommended by the manufacturer. Under similar optical illumination power of ~18.5–20 mW, the emission bandwidth of the TOPTICA emitter was >3 THz, whereas the maximum bandwidth achieved for the in-house emitters was ~2.4 THz. The difference in amplitude was at least one order of magnitude for any given emission frequency.

Part of the motivation for optimising the photomixers was to use them as a source of CW-THz to injection lock a single mode THz-QCL operating in continuous-wave mode close to 2 THz. However, clearly the state-of-the-art photomixer from TOPTICA Photonics has a much higher overall signal. Eventually both the emitter and receiver from TOPTICA Photonics were used for spectroscopy measurement (see Section 4.8) and injection locking of THz QCLs (see Chapter 5) as explained later in the thesis.

4.7 Carrier-lifetime measurement

Photocurrent correlation technique was used to measure carrier lifetime [223]. The total photocurrent generated upon illumination of two consecutive high powered pulses would be lower than the pulses being illuminated separately. This is due to the sublinear characteristic of a photoconductor at high intensity illumination [223]. Hence by time delaying the second pulse, effect on the photoexcited carriers from the first pulse can be measured. The rate of decay of the measured photocurrent pulse can provide information on the carrier lifetime of the material [224].

The carrier lifetime of the photomixer devices fabricated on wafers L1141, L1148 and L1092 reported in the previous section was measured. Results based on the annealing temperature, the material resistance and maximum measured bandwidth are discussed, and related to the carrier lifetime obtained from these photocurrent correlation measurements.

4.7.1 Experimental configuration

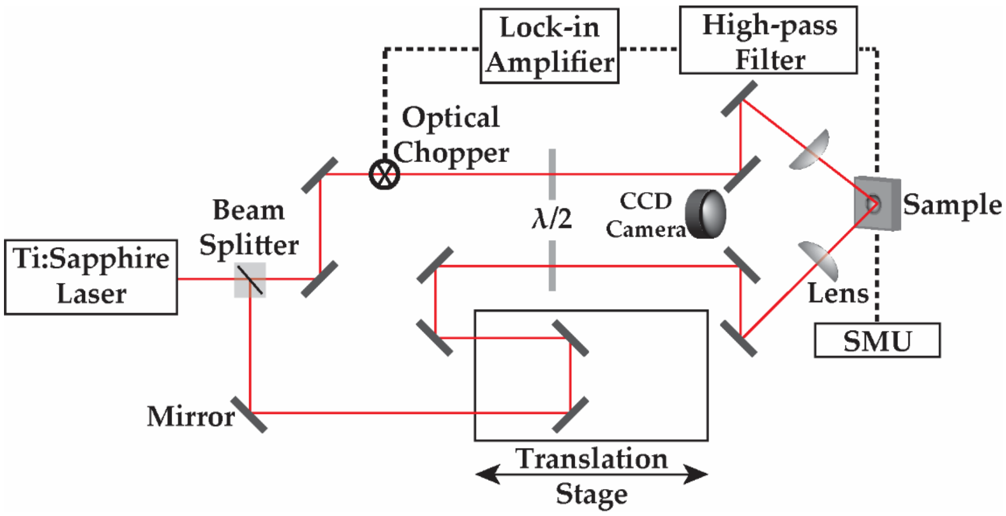

Figure 4.23: Schematic representation of experimental apparatus for photocurrent correlation measurement.

An illustration of the experimental configuration for photocurrent correlation measurement is shown in Figure 4.23. Femtosecond pulses with a centre wavelength of 800 nm, a 110 fs pulse width and a repetition rate of 80 MHz were generated by pumping a Spectra Physics Tsunami titanium-sapphire laser with a solid state diode laser Spectra Physics Millennia XS operating at 532 nm wavelength. The optical beam was split into pump and probe beams using a beam splitter. The beams were reflected through several fixed mirrors and focused using a 10 cm focal length lens onto the sample at the same spot. The probe beam was time delayed using a mechanical translation stage and optically chopped at 2.8 kHz for conventional lock-in detection, before being focused onto the sample. The power in each beam was attenuated to an average of 10 mW using neutral density filters. Half-wave plates were placed to control the polarisation of each beam individually.

The device was biased using the SMU. A lock-in amplifier was connected to monitor the SMU modulated at the chopper frequency. A high pass filter was placed between the lock-in and the device to filter out any DC offset. This was also important as the signal channel on the lock-in amplifier had a current limit of 3 μA. The probe beam was delayed with respect to the pump beam using the translation stage with a step size of 0.01 ps, while the signal was recorded at each step using a LabVIEW programme courtesy of Dr Nicholas Hunter and Dr Christopher Wood. Any offset in the signal was balanced by the auto offset function of the lock-in to avoid saturation in the measured photocurrent correlation pulse. The recorded signal was an average of four repeated scans. This was done to improve the signal-to-noise ratio (SNR) of the measurement.

4.7.2 Polarisation dependence

Measurement of the photocurrent correlation pulses were dependent on the relative polarisation between the pump and probe beam. Figure 4.24 (a) shows a photocurrent correlation pulse recorded for the two beams in both parallel (black) and orthogonal (blue) polarisations with respect to each other. This is plotted against time delay between them. The amplitude of each signal has been normalised to its peak in order to show the difference between the two signals clearly. For parallel polarisation, coherent interaction between the two beams causes a sharp spike at zero time delay. The hump at the bottom was due to carrier trapping. This phenomenon has previously been reported in Refs. [225-227]. It has been attributed to the "short carrier–carrier scattering time present at high carrier concentration". Figure 4.24 (b) shows just the spike due to the coherent interaction (black dots), in which the amplitude has been normalised. The coherence time was expected to last the duration of the laser pulse [225]. A Gaussian fit (red line) to the coherence peak has a FWHM of $111.9 \pm 1.6\,fs$ and this agrees with the FWHM of the laser pulses. The coherent interaction of the laser pulses were avoided as they were not a feature due to the carrier lifetime. Hence, the two beams were orthogonally polarised to reduce the effect of this coherent interaction as shown by the blue line in Figure 4.24 (a).

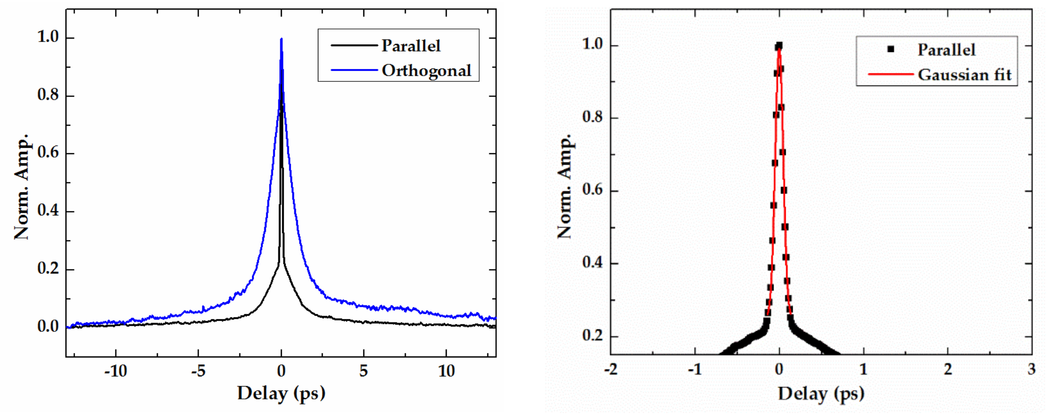

(a) **(b)**

Figure 4.24: (a) Photocurrent measurement at 5 V bias with parallel (black) and orthogonal (blue) polarised pump and probe beam with 10 mW optical power on each. (b) Gaussian fit to spike of photocurrent correlation measurement with parallel polarisation has FWHM of $111.9 \pm 1.6\,fs$.

4.7.3 Results

Orthogonally polarised pump and probe beams with 10 mW average power, as measured on a power meter, were used to obtain the results presented in this section. Photocurrent correlation peaks, obtained with biases between 1–5 V are shown in Figure 4.25 (a). For each photocurrent correlation measurement an exponential curve was fitted to the data using the equation $J(t) = \delta e^{(-|t/\tau_c|)} + (1-\delta)e^{(-t^2 \ln 2/T_G^2)}$, to obtain the carrier capture time (τ_c) where t represents real time, $J(t)$ is the photocurrent, δ the ratio coefficient and T_G the FWHM of the femtosecond laser pulse. The equation has been modelled using Frenkel–Poole effect and field enhanced thermal ionisation as reported in Ref. [227]. An exponential fit corresponding to the first term of the equation (red line) was used to fit the data (black line) as shown in Figure 4.25 (b). Since the two beams were orthogonally polarised, the second term in the equation was avoided as it represented the coherent interaction of the two beams.

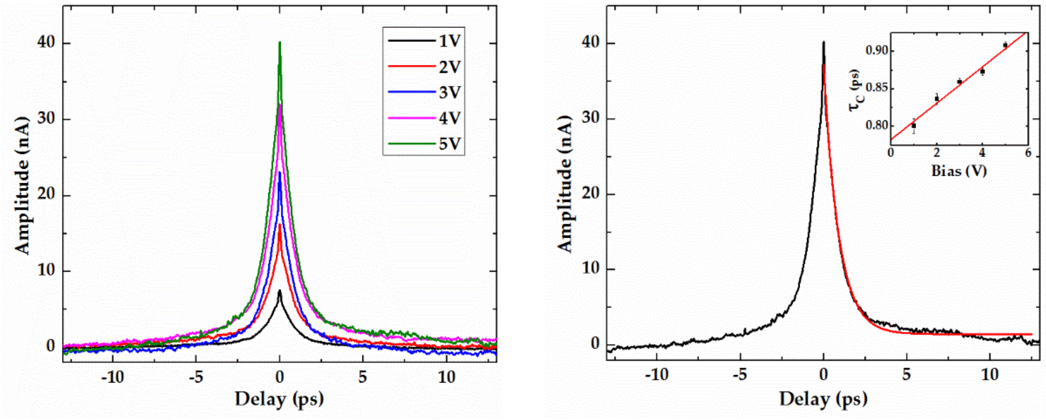

(a) **(b)**

Figure 4.25: (a) Photocurrent correlation measurement at 10 mW orthogonal polarised pump and probe beam for 1–5 V bias. (b) Exponential fit (red line) to a photocurrent correlation pulse (black line) to obtain photo-correlation lifetime. (Inset) Photo-correlation lifetime as a function of applied bias (black dots). Linear fit to the data has been represented as red line.

The inset in Figure 4.25 (b) shows the linear dependence of photocurrent correlation lifetime on the applied bias where black dots and red line represents τ_c values for the range of applied bias and a linear fit respectively. Similar bias dependence has also been observed in Ref. [227, 228]. The photocurrent correlation lifetime increased with electric field due to combined outcome of the Frenkel–Poole effect and field-enhanced thermal ionization [227, 229-231]. The reduction in the required energy for an electron to jump into the conduction band under the influence of a high electric field is known as Frenkel–Pool effect. This reduces the carrier capture cross section and effectively increases the lifetime. The field-enhanced thermal ionization can be described as an increased probability of collision ionization due to increased electron momentum from the applied electric field. This energy gets transferred to increase the electron density in the conduction band and hence increase the overall photocurrent correlation lifetime of the material.

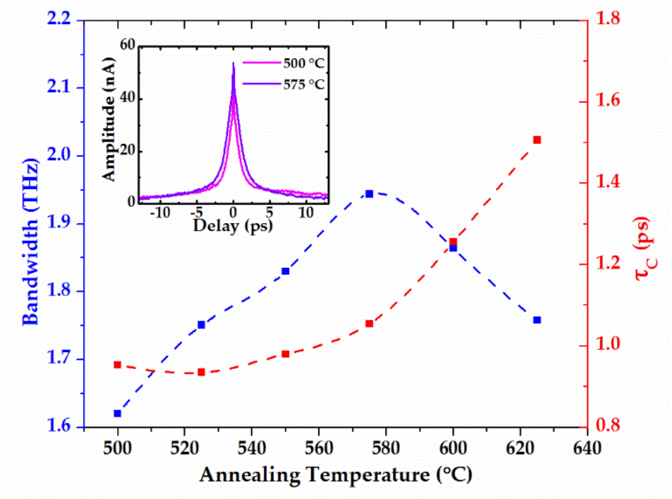

Figure 4.26: Photo-correlation lifetime (red dots) and bandwidth (blue dots) as a function of ex-situ annealing temperatures. (Inset) Photocurrent correlation pulse from devices annealed at 500° and 575° C. Image adapted from Ref. [222].

The carrier lifetime at 5 V bias was measured for devices used in the annealing temperature study in the previous section. The measured values for τ_c as a function of annealing temperature (red dots) are shown in Figure 4.26 along with bandwidth dependence (blue dots) shown previously in Figure 4.19 (c). The measured lifetime does not change significantly between 500–575° C, while the increase in bandwidth in the same range can be safely assumed to be due to increase in material resistance, leading to reduction in background noise. As the measured lifetime rises sharply after 575° C, the maximum measured bandwidth reduces, as would be expected. There was not a significant increase in material resistance at temperatures above 575° C (see Figure 4.16). The inset in Figure 4.26 shows photocurrent correlation pulses for 500 and 575° C annealed devices.

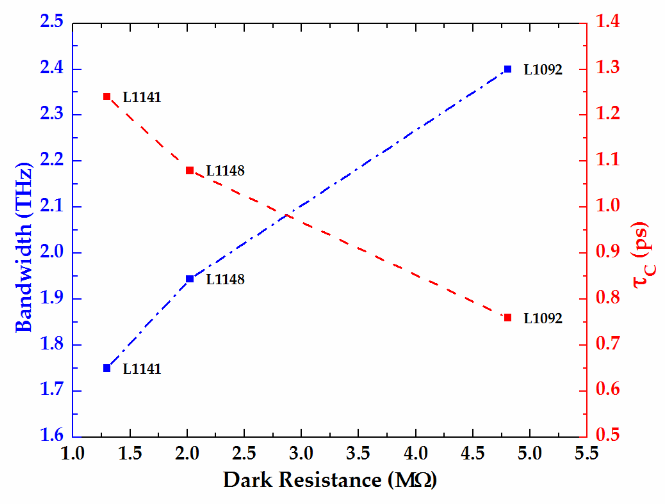

Figure 4.27: Photo-correlation lifetime (red dots) and bandwidth (blue dots) as a function of material dark resistance at 575 °C ex-situ annealing temperature. Wafer numbers have been labelled next to the data point. Image adapted from Ref. [222].

The lifetime was also measured for devices fabricated from wafer L1141 and L1092, both annealed at 575° C. Figure 4.27 compares the lifetime (red dots) of L1141, L1148 and L1092 wafers against their respective dark resistance. The maximum measured bandwidth of the materials (blue dots) as shown previously in Figure 4.20 (b) has also been included in the plot. Wafer L1092 has much lower carrier lifetime as compared with the other two materials, as well as possessing higher resistance. As a result, a significantly improved bandwidth was measured. Conversely the device from wafer L1141 not only had higher carrier lifetime but also lower resistance as compared to L1148, overall resulting in reduced bandwidth.

Overall it can be concluded that although optimising the annealing temperature does improve the bandwidth of the material, a bigger difference in bandwidth was achieved by improved material growth. Under similar annealing conditions, significant improvement in bandwidth was measured from materials having higher dark resistance and a much lower photocurrent correlation lifetime.

4.8 Continuous-wave (CW) terahertz spectroscopy

The TOPTICA emitter and receiver were used to measure high resolution absorption features of a $LiYF_4$-Ho crystal, using CW terahertz transmission spectroscopy. The sample was provided by Dr Joshua Freeman.

4.8.1 Reference time-domain spectroscopy measurements

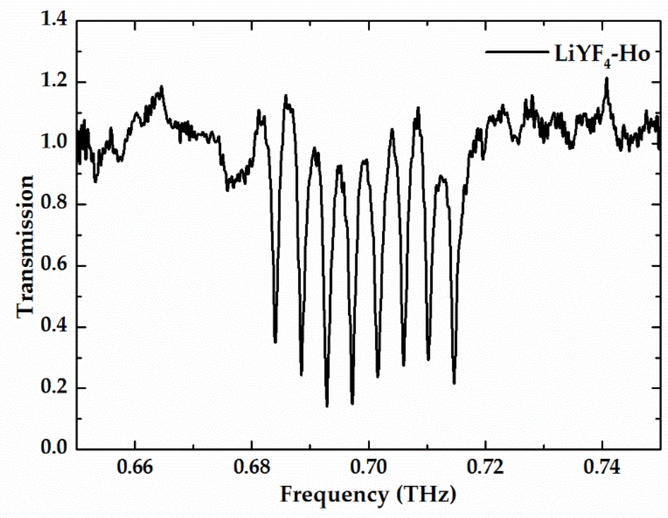

Figure 4.28: Time domain spectra of the $LiYF_4$-Ho sample. Image courtesy of Dr Joshua R. Freeman.

The transmission measurement of a $LiYF_4$-Ho sample was done using THz-TDS. The measurement was carried out with the sample cooled to 4 K using a continuous flow liquid helium cryostat. A THz-TDS transmission spectrum of the crystal is shown in Figure 4.28 and was done by Dr Joshua. R. Freeman. Eight hyperfine absorption features equally spaced at 4 GHz were observed with a frequency resolution limited to 0.5 GHz due to the finite travel length of the translation stage in this measurement. This spectra was used as a reference to measure the same spectral signatures with higher resolution using CW-spectroscopy.

4.8.2 Experimental configuration

The configuration of the CW-THz spectroscopy system is illustrated in Figure 4.29. The TOPTICA emitter and receiver were used and their optical connections were similar to the characterisation apparatus mentioned in Section 4.4. The CW-THz free space optics was changed from two parabolics to four parabolic mirrors. An additional 0.3 m fibre was added on the probe beam arm to compensate for the resulting increase in THz path length.

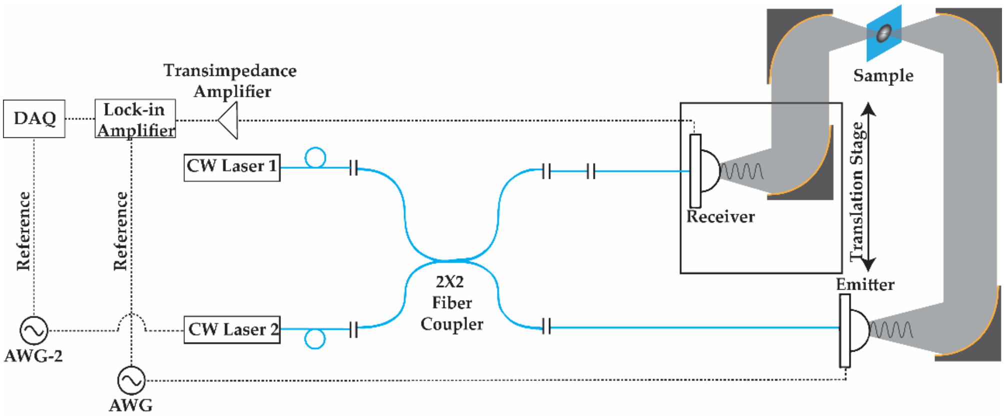

Figure 4.29: Schematic representation of the experimental apparatus of continuous-wave terahertz spectroscopy using TOPTICA emitter and receiver.

The sample was mounted on the cold finger of Oxford Instruments MicrostatHe and placed in the focal spot between the second and third parabolic mirrors. The cryostat was pumped down to pressure < $5\text{x}10^{-6}$ mbar and cooled using a continuous flow of liquid helium. The heatsink temperature was monitored and controlled using a temperature controller. The zero delay path difference was found in exactly the same way as already explained in Section 4.5.2, but with the THz radiation transmitted through the sample.

The emitter was biased at ±10 V with a 7.6 kHz square-wave, while the output of the receiver was connected to a lock-in amplifier, referenced at the emitter modulation frequency through a 10^7 gain transimpedance amplifier. The full range of the piezoelectric transducers were modulated using a triangular-wave generated from a second AWG. These were then connected to the frequency modulation input of laser controller connected to 'Laser2'. The frequency modulation input for 'Laser1' was terminated using a 50 Ω termination. The data recorded from the lock-in amplifier was connected to the input of a basic Data Acquisition (DAQ) board from National Instruments. A TTL signal from the second AWG served as reference for the DAQ board. The data was processed in near real-time using a LabVIEW script written by Dr Joshua. R. Freeman. This way the heterodyne frequency could be modulated over the range of a single piezoelectric transducer scan while the transmission spectra of the samples could be displayed on the computer monitor in near real-time. The entire apparatus from emitter to receiver was purged with dry air below 5% humidity to minimise the effects of water absorption.

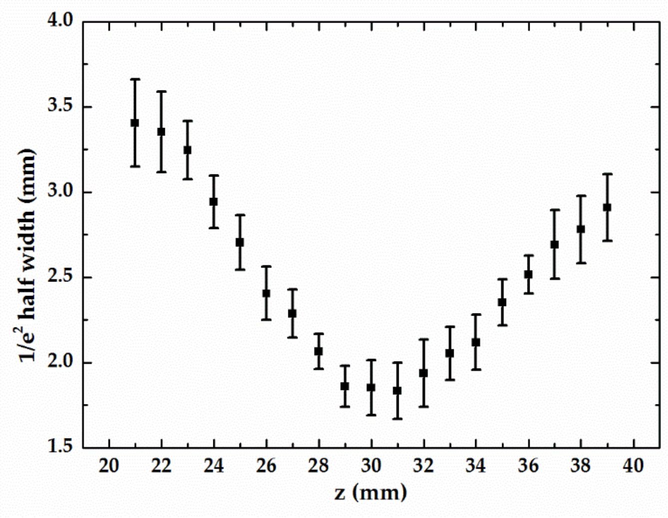

Figure 4.30: $1/e^2$ half-width of the radiation spot from the TOPTICA 780 nm emitter as a function of distance from the focal spot.

The THz beam spot size at the sample position was characterised using the 'knife-edge' measurement technique already mentioned in Section 4.5.5. Figure 4.30

shows the 1/e^2 half-width of the spot size as a function of the distance from the focal position at z=30mm. The minimum measured THz beam spot size was 1.83±0.17 mm at the emission frequency of 1 THz. The same emitter has been reported to have a produce a shallow beam focus of size ~2.5 mm, measured at 300 GHz emission frequency and at a distance of approximately 40 mm from the emitter [232]. A 'Knife-edge' close to the emitter measured a THz beam spot size of 1.41±0.13 mm at 1 THz emission frequency, which agrees with the reported spot size.

4.8.3 Results and comparison with THz TDS

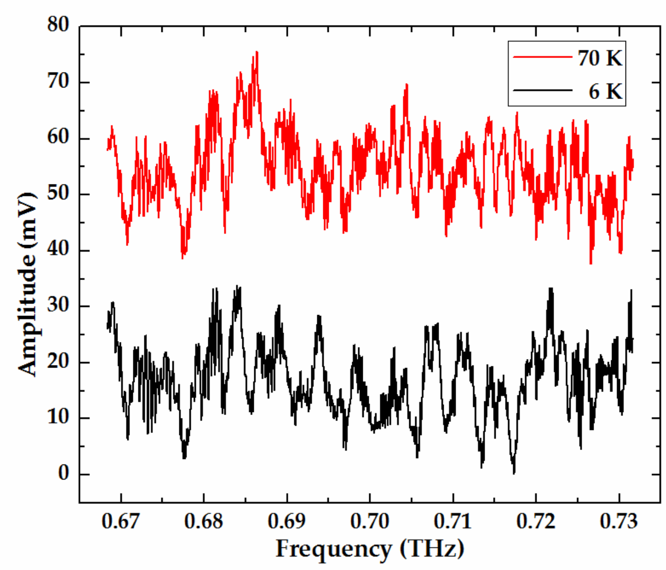

Figure 4.31: Continuous-wave spectra of $LiYF_4$-Ho sample at 6 K (black) and 70 K (red) heatsink temperature.

The heterodyne frequency was tuned to 700 GHz, the sample was cooled to 6 K heatsink temperature and transmission scans were taken by modulating the piezoelectric transducers with a 5 V peak-to-peak ramp at 0.2 Hz modulation frequency with 1 ms lock-in time constant. The effective frequency resolution of the system was ~38 MHz over a ~66 GHz frequency span. Each scan time was ~5 seconds. 20 scans were averaged to improve the SNR.

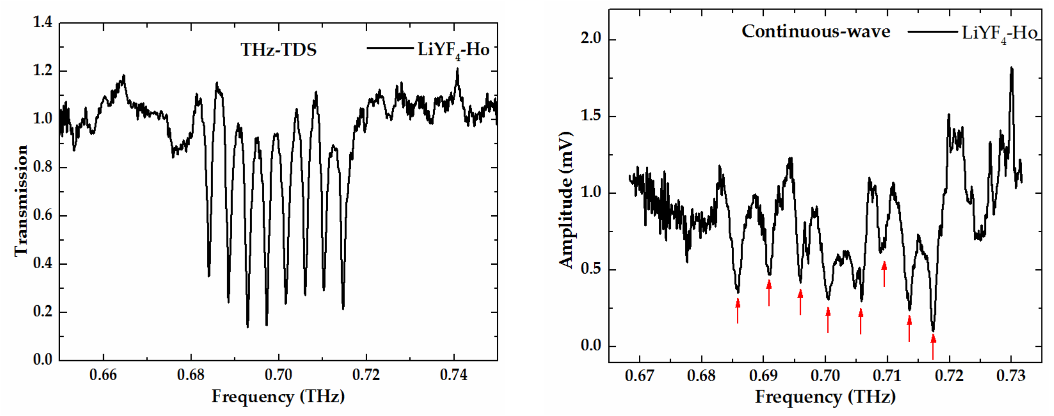

(a) **(b)**

Figure 4.32: Transmission features of LiYF4-Ho sample at 6 K heatsink temperature and around 700 GHz using (a) THz-TDS and (b) CW-THz spectroscopy techniques (marked with red arrows).

With the THz-TDS measurement it was observed that the hyperfine features disappeared above 70 K heatsink temperature (later referred to as a reference). Figure 4.31 shows a CW-transmission measurement through the sample at 6 K heatsink temperature (black line). The raw plot at 6 K does not reveal the expected hyperfine features as a lot of oscillations were present in the spectra. Certain dips from the spectra were observed to disappear gradually as the heatsink temperature increased to 70 K. Other oscillations in the spectra were still present. As these oscillations are temperature independent and are seen at different heterodyne frequencies, they can be assumed to be artefacts from the emitter-receiver cavity, the system in general or the lasers. Investigation of these features were beyond the scope of this work. This effect could be seen in real-time due to the fast and high resolution frequency scanning technique used. A spectra obtained at 70 K heatsink temperature (red line) is shown in Figure 4.31. To minimise the other oscillations present in the scans, the 6 K scan spectra was divided by the 70 K scan spectra (assumed as reference). The resultant transmission spectrum is shown in Figure 4.32 (b). The eight hyperfine features equally spaced at ~4 GHz were distinguishable (marked with red arrows) and in good agreement with the THz-TDS scans shown again in Figure 4.32 (a). The FWHM of Gaussian fit to the hyperfine features was 1.0±0.3 GHz.

4.9 Summary

In this chapter the basic concepts of THz photomixing were introduced. The steps used for fabrication of a THz photomixer emitter with broadband log-spiral antenna centred with interdigitated fingers on LTG-GaAs substrate was discussed. Epilayers of LTG-GaAs were grown using MBE. Fabrication steps included annealing, electron-beam lithography and evaporation.

The experimental configuration used for characterisation of state-of-the-art photomixers from TOPTICA Photonics and in-house photomixers was explained. Experimental considerations such as zero path delay, characterisation of the ECDLs including frequency stability and tuning range of the piezoelectric transducers, and the knife-edge measurement of the excitation beam spot for in-house emitters was also presented.

The effect of annealing temperature on the emission bandwidth of emitters was studied. The annealing temperature influences material parameters such as dark resistance and carrier lifetime. These parameters were measured and found to be increasing with annealing temperature. Device bandwidth improves by increasing the material's dark resistance but an increase in carrier lifetime deteriorates the bandwidth. An annealing temperature of 575° C was found to provide optimised bandwidth performance of ~1.95 THz. Apart from the annealing temperature, the growth quality of materials plays a more significant role in the bandwidth of devices. Three materials grown nominally under identical conditions showed bandwidths ranging from ~1.75–2.4 THz at identical ex-situ annealing conditions. Materials with the highest bandwidth not only had highest dark resistance but also had lowest measured photocorrelation carrier lifetime.

A state-of-the-art TOPTICA emitter was found to have better frequency response than all the emitters measured, and was therefore used for subsequent continuous-wave spectroscopy measurements of a $LiYF_4$-Ho crystal. Eight hyperfine features around 700 GHz, which were already observed in THz-TDS measurements, were resolved with a higher frequency resolution of 38 MHz over a 66 GHz frequency span in almost real-time.

Chapter 5

Injection locking of continuous-wave terahertz quantum cascade laser

5.1 Background

There are numerous potential applications of terahertz sources. THz QCLs are solid state high power (tens of milliwatts) compact sources, and gaining access to their frequency and phase information simultaneously can unlock further potential applications in fields such as molecular gas spectroscopy [32], far-infrared astronomy [233], atmospheric sensing, coherent imaging and wireless communications [39, 234]. A THz QCL can have an intrinsic quantum-limited linewidth as low as 110 Hz [235], but a free running THz QCL's linewidth is broadened due to extrinsic noise factors such as temperature, bias current noise and mechanical oscillations [235]. Hence, there is a need to stabilise frequency and phase by reducing the effects of these noise.

Frequency locking refers to stabilising the jitter in the frequency of a laser to that of a stable external source. This does not guarantee identical phase between the two sources. On the other hand, phase locking refers to synchronisation of phase of the free running laser to that of an external stable reference. Phase locking ensures frequency lock but the converse may not be true.

So far various approaches have been explored to stabilise the phase or frequency of THz QCLs and the measured jitter in most configurations is limited by the experimental apparatus. An overview of different locking techniques implemented to date are described in the following subsections. A review of some of the locking techniques used so far to lock THz QCLs have been discussed in detail in Ref. [236].

5.1.1 Locking of Fabry–Pérot spectrum

Locking of the beat frequency between two Fabry–Pérot modes of a THz QCL is fundamentally different than locking the frequency to a stable external source. In beat frequency locking, the frequency difference between the modes is locked to an external stable source. This does not stabilise the overall drift/jitter in frequency

Although locking the beat frequency of two Fabry–Pérot modes to an external source does not stabilise the frequency drift of the laser, it does enable a measurement of the individual linewidths of the modes. In one demonstration, two lateral modes of a ~2.7 THz QCL were mixed on a hot electron bolometer (HEB) and the beat frequency was stabilised to an external microwave source using conventional phase-lock loop [237]. In a separate work, a microwave-synthesiser was used to injection lock a multi-mode 2.3 THz QCL operating in CW regime [238]. The device was electrically injected with an RF signal close to Fabry–Pérot mode spacing with varied amplitude to achieve mode pulling and locking. The locking range of the oscillators was ~225 MHz, determined using Adler's equation [239].

5.1.2 Locking to a stable THz source

THz QCLs have been phase locked to many different stable frequency sources. In 2005 the first ever frequency and phase locking of a THz QCL was reported using a far-infrared gas laser line at 3.105 THz as a stable reference source [240]. The frequency was stabilized indefinitely using conventional phase lock loop. The beat signal had a full-width-half-maximum (FWHM) of 65 kHz, which was larger than the linewidth of the gas laser. The beat signal stability was further improved to 3–4 kHz using a similar concept [241]. Frequency locking of a THz QCL has also been done by locking to a commercial stable solid state frequency multiplier [242]; and harmonic of a microwave synthesiser source [243]. In these experiments, superconducting HEBs were used as mixers to generate intermediate frequency (IF). Although very stable IF FWHM were achieved, cryogens were required not only to cool the THz QCL but also the HEBs. In most of the locking configurations, frequency multiplier sources (used as local oscillators) were used and they intrinsically suffer from extremely low power outputs at high frequencies. THz QCL frequency has also been locked using a room temperature operating Schottky diode balanced mixer and microwave synthesiser [244].

5.1.3 Locking to a molecular absorption lines

For all the frequency locking of THz QCLs using molecular transition lines reported so far, methanol gas has been used. In 2010, the first demonstration of locking a THz QCL to a 2.55 THz absorption line was reported [245] and the frequency jitter was further stabilised to 18 kHz using third-order distributed feedback single mode THz QCLs lasing at 3.5 THz [246]. The same group reported an additional amplitude stabilisation of the same THz QCL using swing-arm voice coil actuator, along with frequency stabilisation using the same technique [247]. Gas absorption linewidths are intrinsically in the MHz range, and thus achieving relatively narrow (in 10's of kHz) IF FWHM requires use of cryogenically cooled HEBs as they are very sensitive and fast response detectors [244]. Apart from using cryogens for detectors, this technique requires the frequency of the lasing source to match an absorption line, restricting any frequency tunability. It also makes phase locking the source impossible.

5.1.4 Locking to a femtosecond laser

A 2.7 THz QCL was completely phase-locked to a harmonic of 90 MHz repetition rate of a mode-locked erbium-doped fibre laser [248]. The beat signal generated by mixing the THz QCL and the fibre laser on a ZnTe crystal, achieved a very high SNR of 80 dB with 1.5 MHz bandwidth. A THz QCL operating at 2.32 THz was also reported to be phase-locked to a frequency comb generated using a photomixer and a femtosecond fibre laser [249]. Although these techniques allows phase-locking of THz QCLs within the bandwidth of the femtosecond lasers and does not require cryogenically cooled HEBs, its application is limited by use of expensive and bulky femtosecond lasers.

5.1.5 Injection seeding

Injection locking and injection seeding are two different phenomenon. The former refers to an injection of a weak monochromatic signal into a free running oscillator within its locking range. The injected signal then dictates the oscillator's output [250]. Injection seeding or pulsed injection locking is more commonly termed when a weak signal, also known as 'seed', is injected into a pulsed oscillator operating at higher output power during its turn on period. The injected signal might not necessarily be within the locking range of pulsed oscillator or too weak to lock the oscillator output but it does influence the initial cavity conditions before lasing. Hence, the seed has some control of the lasing action initiated after the injection [250].

Phase-locking of a THz QCL has been reported by seeding the laser cavity with a THz pulses of fixed phase [251]. This work demonstrated injection seeding of THz QCL in pulsed mode. Instead of QCL emission phase being dominated by a random spontaneous emission, it was fixed to the phase of the injected THz seed electric field generated from a photoconductive material. Hence, it allowed detection of the electric field of THz pulses from the QCL using electro optic detection technique.

Although the injection seeding technique demonstrated does not require any frequency stabilisation or active feedback electronics to maintain phase synchronisation, they still use bulky and expensive femtosecond pulse sources and/or complicated and bulky RF electronics.

5.2 Outlook

The prime objective of this chapter is to demonstrate injection-locking of a 2 THz QCL using state-of-the-art photomixers and diode lasers. These components are commercially available, relatively cheap and portable. Although photomixers suffer from low emission power at high frequencies, coherent detection of signal achieves high SNR.

The first part of this chapter discusses the attempts to injection lock CW-THz QCLs using the 780 nm TOPTICA photomixers. Experiments were also done to directly mix the optical beams on the THz QCL to detect locked signal. Measurements to record beating of the THz QCL on the photomixer receiver was also carried out. Overall results at ~780 nm photomixers were not successful and the system was changed to the telecommunications wavelength region of 1550 nm. In addition to this, a narrowband free-space injection seeding measurement of a THz QCL was also undertaken in a collaborative work at Ruhr-Universität Bochum, Germany.

In the second half, the wavelength was changed to 1550 nm and TOPTICA 1550 nm emitters and receivers, and lasers from RIO and SANTEC were used to try and injection lock THz QCL in continuous wave mode. Experimental configuration and results from the first successful CW-injection locking of a CW-THz QCL are described. Finally, an attempt was made to measure spectra of the injection locked THz QCL.

5.3 Injection locking with 780 nm photomixers

5.3.1 Experimental configuration

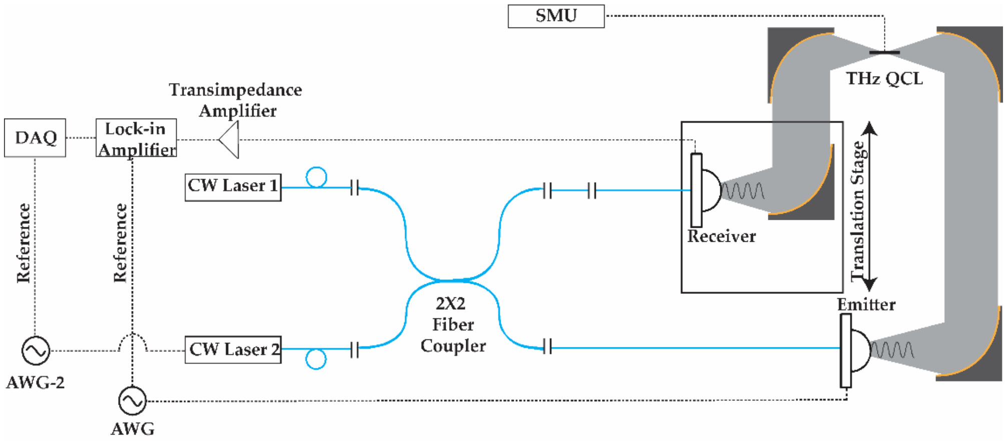

Figure 5.1: Schematic of injection locking of THz QCL using 780 nm ECDLs and TOPTICA emitter and receiver.

The experimental setup used was very similar to the one explained in Section 4.8.2 for CW-THz spectroscopy. LiYF$_4$-Ho sample was replaced with a THz QCL mounted on a cold finger of a Janis ST-100 continuous flow cryostat. Cryostat was mounted on a XYZ manual translation stage and the device was cooled using liquid helium. The heatsink temperature was controlled at ~15 K throughout the measurement. Emission from the emitter was focused onto the front facet of the THz QCL. A small aperture ~1 mm in diameter was carefully glued with Ge varnish in front of the front facet of the THz QCL. It helped in the alignment of the THz beam from the emitter onto the QCL facet. Radiation from the other facet was collimated and focused onto the receiver. The system was boxed and purged with dry air. The experimental configuration is illustrated in Figure 5.1. Electrical and optical connections to the emitter and receiver, and the detection technique with modulation of the piezoelectric transducer of 'Laser2' were unchanged.

5.3.2 THz QCL characterisation

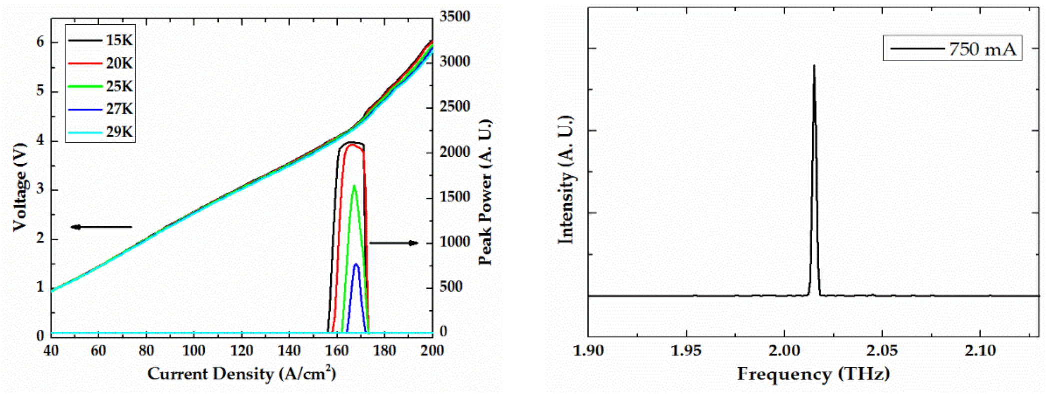

(a) (b)

Figure 5.2: (a) LIV obtained from the THz QCL at range of heatsink temperature in CW mode. Data courtesy of Reshma A. Mohandas. (b) Spectra of the THz QCL operating at 750 mA DC current and 15 K heatsink temperature (resolution ~280 MHz).

The THz QCL used for this work was grown by Dr Lianhe H. Li, wafer number L1071, fabricated and characterised by Miss Reshma A. Mohandas. The laser was a bound-to-continuum design, semi-insulating surface plasmon waveguide with 2.5 mm long, 200 μm wide and 14.6 μm high ridge. The LIV performance at a range of heat sink temperature with device operating at constant current mode is shown in Figure 5.2 (a). The device was essentially lasing in single mode at 2.015 THz under constant current of 750 mA and 15 K heat sink temperature, and the spectra is shown in Figure 5.2 (b). The frequency resolution of the spectra was ~280 MHz. The expected Fabry–Pérot mode spacing for this device is close to ~16 GHz.

5.3.3 Initial results and discussion

The THz QCL operating at 750 mA of constant current was close to its peak emission power. The minimum spot size of the THz radiation focused on to the QCL facet from the photomixer was ~1.41 mm (see Section 4.8.2). Even after the QCL was positioned at the focus along with the ~1 mm aperture in front of it, some signal was going around the QCL and could be detected on the emitter. To get close to the focal point, the signal on the receiver was maximized by changing the device position along the beam path direction.

The heterodyne frequency was set close to 2.015 THz, the operating frequency of the THz QCL. Translation stage was scanned across a long range and the sinusoidal fringes were measured. The FFT of the detected signal and also a sinusoidal curve fitting confirmed the emission frequency was within 10 GHz of the required frequency. The translation stage was positioned at zero path delay position. The piezoelectric transducers were modulated using a triangular-wave and signal was recorded in the same way as done for CW-spectroscopy in Section 4.8. If the THz QCL was injection locked to the emitter radiation, a peak was expected at the operating frequency of the THz QCL when the piezoelectric transducer was swept. The increase in detected amplitude would be due to the radiation from the QCL being phase synchronised with the injected CW-THz and detected on the receiver. Unfortunately, there was no sign of injection locked signal from the THz QCL in the frequency scans performed. The scan resolutions tried were as high as 0.5 MHz over a range of 13 GHz by decreasing the modulating frequency and voltage to the piezoelectric transducer. All attempts to detect any injection locked signal of the THz

QCL was unsuccessful.

Assuming the spot to be perfectly circular with a radius of 1.41 mm and its perfect alignment to the THz QCL, only ~0.03% of the radiation was coupled into the active area of the laser. It was concluded that not enough signal from the emitter was getting coupled into THz QCL due to significantly large spot size of the THz radiation.

5.3.4 Other configurations

5.3.4.1 Narrowband optical injection

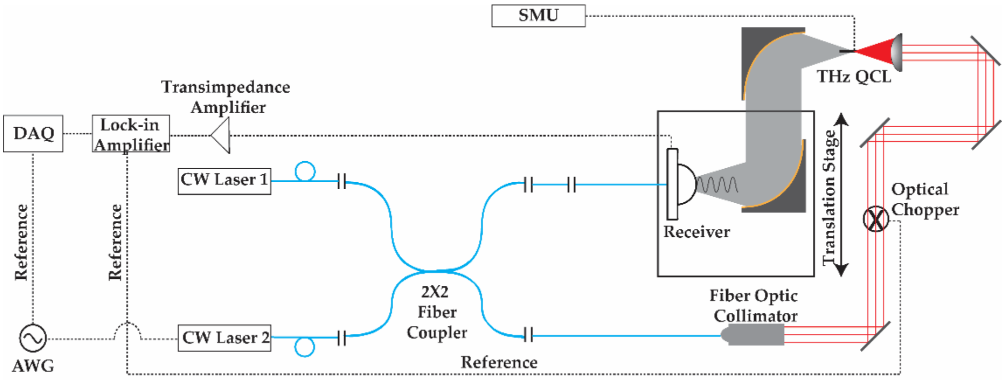

Figure 5.3: Experimental setup for mixing of two 780 nm lasers onto the QCL facet.

So far radiation generated by mixing two ECDLs on photomixer was used to try and injection lock a THz QCL. An attempt was made to directly mix of the two optical beams from the ECDLs on the facet of the THz QCL. It was expected that the THz emission from the QCL would be phase matched with the injected beat frequency of the optical beams. The experimental setup used is shown in Figure 5.3. The 20 mW output of the excitation beam was coupled into free space using fibre collimation package. It was focused onto the QCL facet using MITUTOYO 10X NIR 0.26 numerical aperture microscope objective mounted on a manual translation stage to adjust the focal position. The minimum spot size was measured to be ~20 μm using ‘knife-edge’ technique.

Similar to the previous experiment, a 15 K heatsink temperature was set, the THz QCL was biased with 750 mA of DC current and the setup was purged with dry air. Output from the other facet of the THz QCL was coupled into the receiver using two parabolic mirrors. Signal from the receiver was amplified by transimpedance amplifier. Excitation beam was mechanically chopped at 1.3 kHz for conventional lock-in detection technique. The resistance of THz QCL dropped by ~10% with the optical beam focused onto the facet. Unfortunately, no signal from the THz QCL was observed on the receiver photomixer with the frequency scan technique mentioned earlier. The noise level detected on the lock-in amplifier was ~6 mV.

5.3.4.2 Beating on photomixer receiver

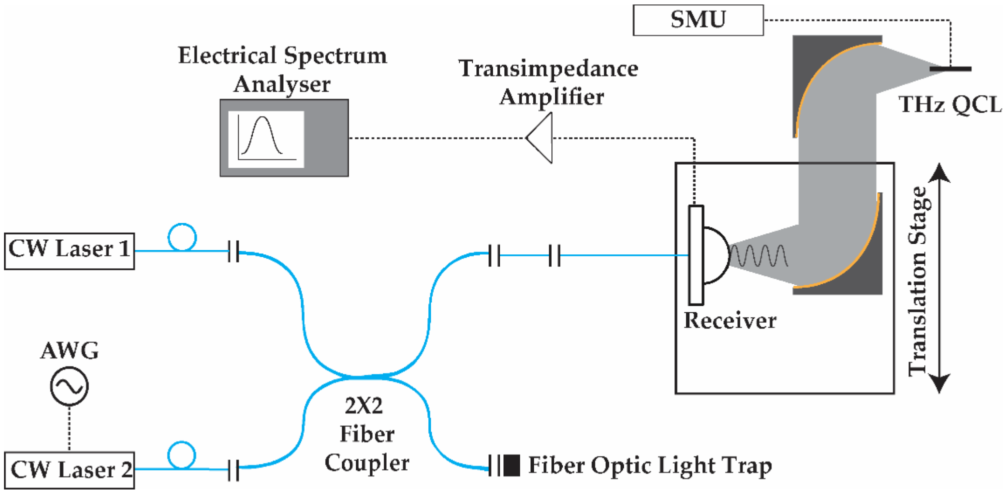

Figure 5.4: Experimental setup of beating of free running QCL on the emitter.

Another experiment was carried out by directly beating the THz QCL emission on the receiver and measuring it on an electrical spectrum analyser (ESA). The experimental setup is shown in Figure 5.4. THz QCL was biased at peak emission power and operation was not perturbed by any external means. Similar to the previous experiments, the output of the THz QCL was directly coupled into the receiver using two parabolic mirrors. The output of the receiver was connected to ESA via a transimpedance amplifier.

The heterodyne frequency was set close to 2.015 THz. Bandwidth of the ESA was 3 GHz. At the usual 10^7 low noise gain the bandwidth of transimpedance amplifier was just 220 kHz. Instead, the transimpedance amplifier bandwidth was switched to its maximum (200 MHz) with a low noise gain of 10^2. Number of steps to cover the full frequency tuning range (~80 GHz with ±3 V bias) of the piezo electric transducer was 80/0.2 ≈ 400 steps. The piezoelectric was biased at a step size of 6/400 ≈ 0.015 V and the frequency response on the ESA was saved. Any signal within 200 MHz of the heterodyne frequency could be detected. Unfortunately, no signal on the ESA was detected.

The noise floor of the ESA was −80 dBm at low noise gain of 10^2. The peak power measured using helium cooled Si-bolometer from the TOPTICA emitter at 2 THz emission frequency and from the THz QCL used was 10 nW and 1 mW respectively. Peak amplitude of the 2 THz emission from the TOPTICA emitter detected by the receiver was 1 mV on the lock-in amplifier with a transimpedance gain of 10^7. Hence the expected signal from the THz QCL at 10^2 gain would be ~3 μV (-100 dBm) on the lock-in amplifier, which is well below the noise floor of the ESA. This could explain why no signal was detected. The piezo was rescanned with 10^3 gain on the transimpedance amplifier. Yet again no signal was detected on the ESA. At these setting the noise floor of the ESA was increased to −60 dBm and the expected signal was still below the noise floor at −80 dBm.

5.3.4.3 Narrowband free-space injection seeding

An attempt was made to injection seed a THz QCL with a narrowband free-space optical beat from a tuneable CW dual mode external cavity diode laser (DM-ECDL) operating at ~800 nm. The optical beat frequency close to the THz QCL Fabry–Pérot mode was generated by tuning the two modes of the DM-ECDL and was used as a seed for the THz QCL cavity. It is believed that, with the gain of the THz QCL switched by RF pulses, the lasing action would be dominated by the seed since the electric field of the seed should be greater than the spontaneous emission. This uses a similar arrangement to the phase-seeding of a THz QCL with broadband THz pulses as reported in Ref. [251]. The injection seeding was monitored by changing the seed frequency to match modes of the THz QCL and recording spectra of the output modes.

The work described in this subsection was carried out during a three week research visit to the *Lehrstuhl Für Angewandte Festkörperphysik*, Ruhr-Universität Bochum, Germany and led by Prof. Andreas D. Wieck and Dr Nathan Jukam. The THz QCL used for this work was grown by Dr Lianhe Li, fabricated by Miss Reshma A. Mohandas (University of Leeds) and packaged by Dr Hanond Nong (Ruhr-Universität Bochum). The DM-ECDL was provided by the Engineering Department in Ruhr-Universität Bochum. The work was carried out with collaborated efforts of Dr Nathan Jukam, Dr Shuvon Pal and Miss Hekmat Negar from Ruhr-Universität Bochum, and Mr. David Bacon from University of Leeds.

5.3.4.3.1 Experimental configuration

The experimental configuration used is shown in Figure 5.5. A tuneable CW DM-ECDL with peak output power >1 W used as a source to generate the seed signal. The seed signal intensity was attenuated to ~20 mW. The free space output from the back facet was aligned to the external cavity of the laser. The two diffraction gratings were used to change the optical feedback into the laser cavity and hence tune the emission lines. The two emission lines used in this work were ~808 nm and ~815 nm. These wavelengths were chosen due to their close proximity to the effective bandgap (~812 nm) of the GaAs/AlGaAs THz QCL. Ref. [252] reports a resonant nonlinearity close to the effective bandgap in a similar THz QCL device. This allowed a higher conversion efficiency of ~0.13% for the mixing between the NIR and THz fields. A small part of the DM-ECDL output emission was split and coupled into a multimode fibre connected to a compact spectrometer. The emission lines were measured using a software package provided with the spectrometer. Mounting of the THz QCL on the cryostat, cooling down and temperature control was done in a similar way as already mentioned for experimental configuration in Section 5.3.1. The heatsink temperature was controlled at 20 K throughout the measurements. Optical radiation was focussed onto one of the QCL facet using couple of cylindrical lens. This was done to control the beam shape in both X-Y directions which allowed the beam to be focused in a rectangular shape, similar to the QCL facet shape. It was thought to improve the coupling. The FWHM of the spot was measured to be 240 μm by 260 μm. Output from the other facet was directed towards a Michelson Interferometer and measured using pyroelectric detector.

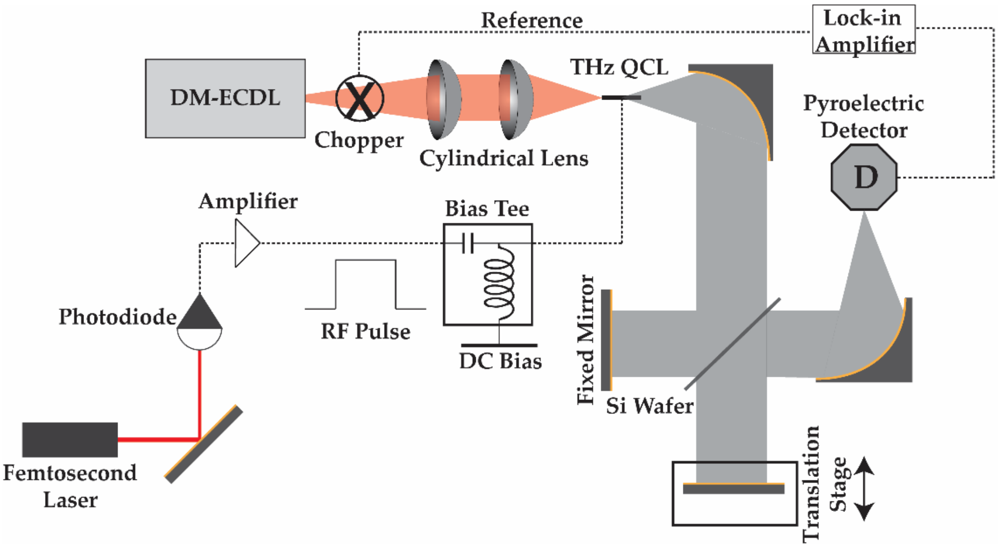

Figure 5.5: Experimental configuration for free-space injection seeding.

A bias-tee was used to bias the THz QCL below threshold using quasi DC signal of a 10% duty cycle square-wave modulated at 10 kHz and RF voltage pulses.

These pulses were generated by illuminating a fast photodiode with femtosecond laser source with a repetition rate of 80 MHz. Each pulse duration was 2 ns and was amplified to ~200 mV. The RF pulses were generated in a similar way to that reported in Ref. [251]. The optical beam was mechanically chopped at 10 Hz for lock-in detection. This modulation frequency was limited by the response speed of the pyroelectric detector.

5.3.4.3.2 THz QCL characterisation

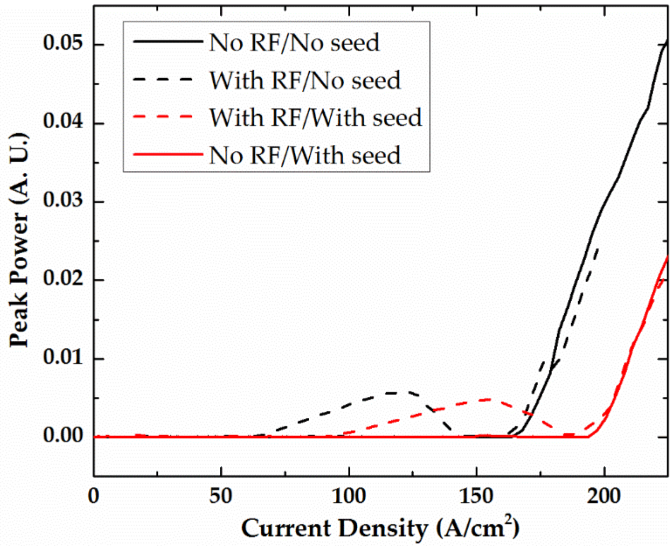

Figure 5.6: THz QCL L-J measured without RF and seed (solid black), only RF (dotted black), both RF and seed (dotted red) and only seed (solid red). The current density only measures the quasi-DC current, not the current from the RF pulse.

The THz QCL used was a bound-to-continuum active region design with semi-insulating surface plasmon waveguide, fabricated from wafer L1152. The laser ridge was 2.15 mm long, 150 μm wide and 14 μm high. The light-current density (L-J) measurement of the THz QCL with various combinations of RF pulses and optical seed signal is shown in Figure 5.6. In these measurements, L-J was not measured throughout the dynamic range of the THz QCL as threshold region was of interest to observe a local minima when RF pulses are applied. The solid black line shows the

L-J of the THz QCL without any RF pulse. As soon as the RF pulses are applied, a local maxima is observed below the lasing threshold as shown by dotted black line. The RF pulses turns on the THz QCL even when the DC offset is below threshold (the current in Figure 5.6 only measures the quasi-DC current). Similar L-J were measured with and without RF pulses in the presence of the optical seed signal focussed onto the THz QCL facet and is shown as dotted red line and solid red line, respectively. In the presence of the optical radiation, the threshold current density shifts higher. This possibly suggests thermal heating of the QCL due to the optical radiation.

5.3.4.3.3 Results

The output spectra of the THz QCL without the optical seed signal measured at a quasi-DC bias set at the peak of local maxima (black dotted line in Figure 5.6) is shown in Figure 5.7 as black solid line. The laser was multimode laser with ~3.4 THz having the highest intensity. The spectra represented by a solid red line was taken with beat frequency of the optical seed very close to ~3.4 THz. Unfortunately, the spectra obtained in presence of optical seed was not dependent on the beat frequency of the optical seed; emission of the Fabry–Pérot mode corresponding to the beat frequency of seed signal and the suppression of other modes was not observed. To study the effect of optical injection but without a beat frequency, the feedback of ~815 nm emission wavelength was blocked in the external cavity of the DM-ECDL so that only ~808 nm wavelength is present. The spectra with only ~808 nm optical radiation focussed on the facet of the THz QCL is shown as solid blue line in Figure 5.7. This spectra is also similar to the spectra with beat frequency of the optical signal close to ~3.4 THz, again suggesting that the change was due to the presence of optical radiation rather than the resonant beat frequency. Although the spectral resolution is 7.5 GHz, different modes of the THz QCL were not resolved properly. This is due to a combination of the noise in the pyroelectric detector and also poor alignment of the interferometer.

It is possible that the seeded electric field was not large enough to dominate the spontaneous emission. For this reason spectra was also taken with increased incident optical power of ~150 mW, but the results qualitatively the same. As the DC offset was fixed, heating of the THz QCL due to the presence of optical radiation caused the threshold to increase as already shown in Figure 5.6 (compare black and red dotted lines). Therefore, the peak amplitude in the presence of optical seed is lower.

Another possibility for the failure of this experiment could be instabilities in the ECDL. It is possible that the ECDL was switching between the lasing modes faster than the spectrometer could respond. Unfortunately, due to lack of time in Germany further investigations could not be carried out.

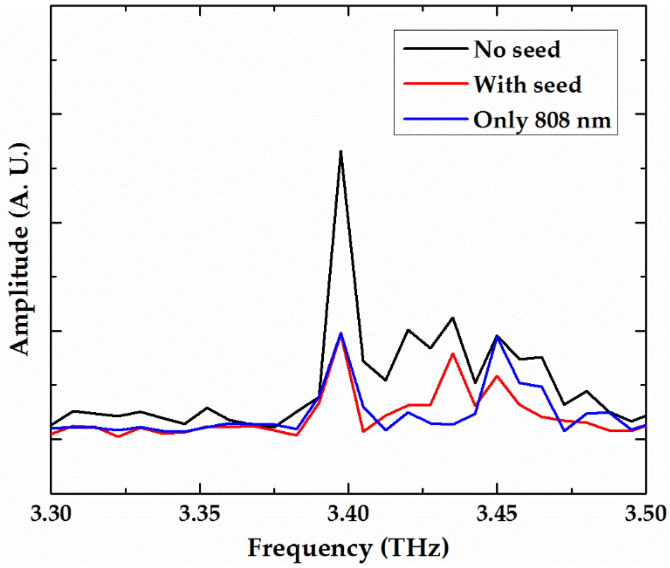

Figure 5.7: THz QCL spectra without CW seeding in black and with CW seeding at different beat frequencies.at 7.5 GHz spectral resolution.

5.4 1550 nm photomixers

The excitation wavelength was changed from 780 nm to the more developed telecoms wavelength region of 1550 nm. Photomixers (both emitter and receiver) operating at 1550 nm were purchased from TOPTICA Photonics. These photomixers were designed on InGaAs substrate with bow-tie antenna structure. They were packaged with an integrated Si lens and pigtailed PM fibre. A second attempt was made to injection lock the THz QCL.

5.4.1 Experimental configuration

The experimental apparatus used is illustrated in Figure 5.8. The detection technique was similar to the one used in photomixer characterisation (see Section 4.4). The TOPTICA 780 nm photomixers were replaced with TOPTICA 1550 nm photomixers. A RIO Orion Laser Module and a SANTEC TSL-710 lasers were used as the optical source for the photomixers. The wavelength and output power of the RIO laser was fixed to 1554.969 nm and 10 mW respectively. The external cavity SANTEC laser was tuned close to the RIO laser wavelength to achieve desirable heterodyne frequency with maximum variable output power of 20 mW. Polarisation of the each laser output was controlled with manual fibre polarisation controller (PC). Erbium-doped fibre amplifier (EDFA) was used to amplify the combined output of the two lasers and excite each photomixer with 30 mW optical power using 2X2 fibre optic coupler designed for 1550 nm centre wavelength. Optical spectrum analyser (OSA) was used to monitor the wavelength and amplitude from the two CW-lasers. A set of PCs were placed before emitter and receiver to control the polarisation of the incident light, improving the emission/detection power of the system.

The emitter was biased at −2 V–0.5 V square-wave modulated at 7.6 kHz using an AWG. The THz QCL used for this work was the same device which was used for the 780 nm injection locking measurement (see section 5.3.2) and was positioned in the same place as before. The device was biased using a SMU with a constant current of 750 mA at 15 K heatsink temperature. A second lock-in amplifier was connected to monitor the SMU at emitter modulation frequency. It helped in aligning the THz spot onto the QCL's facet and has been further explained in Section 5.4.3.

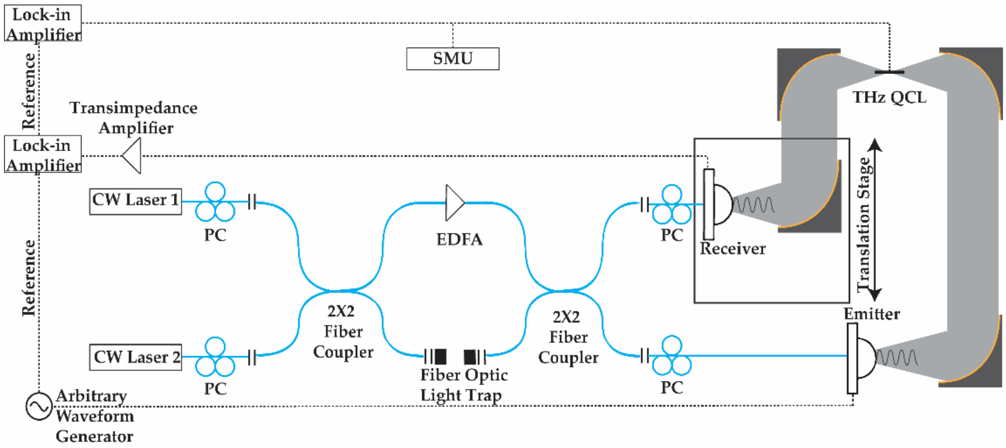

Figure 5.8: Schematic of injection locking of THz QCL with 1550 nm diode lasers and TOPTICA emitter and receiver operating at 1550 nm.

5.4.2 System characterisation

System characterisations done at 780 nm excitation wavelength (see Section 4.5) were again carried out for the 1550 nm experimental setup. Combined linewidth of the lasers, measurements of the spot size of the incident emission from the emitter onto the THz QCL and bandwidth of the TOPTICA 1550 nm emitter and receiver were measured in similar way as already mentioned in the previous chapter.

5.4.2.1 Combined laser linewidth

The setup was almost identical to Figure 4.10 (a). The combined output of both the lasers were coupled into an InGaAs based photodiode instead of a Si based photodiode. Output of the photodiode was measured on ESA. Figure 5.9 shows the instantaneous screen capture (black line) and the linewidth measured using max-hold function of the ESA over a time of 3 minutes. The combined linewidth of the 1550 nm lasers were much more stable than the 780 nm ECDLs measured earlier. The drift in beat frequency over time was within a very narrow range of not more than 25 MHz as compared to almost 1.5 GHz for 780 nm ECDLs (see Figure 4.10 (b)).

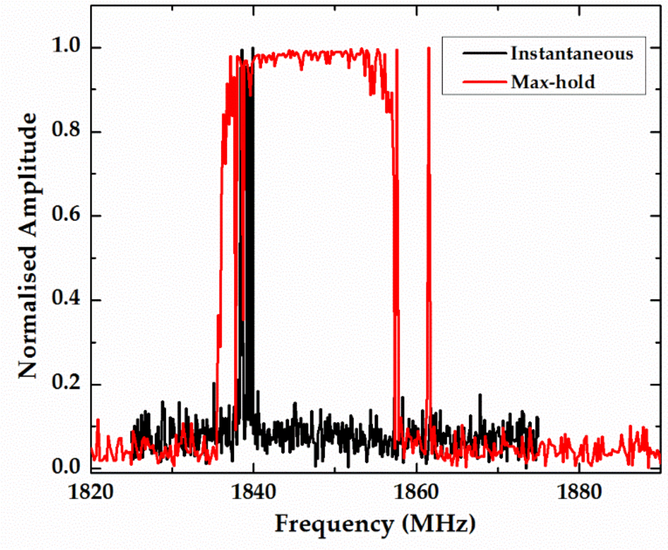

Figure 5.9: Instantaneous linewidth of beating the 1550 nm lasers on InGaAs based photodiode shown in black (RBW: 110 kHz). Linewidth measured over a time of 3 minutes using max-hold function of the ESA shown in red (RBW: 220 kHz).

5.4.2.2 Knife-edge measurement of THz spot size

Spot size of the radiation from the emitter focused onto the THz QCL was measured using the ‘knife-edge’ technique. The heterodyne frequency was set to 1 THz. Figure 5.10 shows the measured spot size as a function of distance from the focal point. The minimum $1/e^2$ half-width size obtained was 0.24±0.01 mm. The spot size was significantly smaller than 1.41±0.13 mm obtained with the TOPTICA emitter designed for 780 nm excitation at the same heterodyne frequency. The same parabolic mirrors were used in both setups to focus the THz radiation generated from the emitters. The decrease in spot size in the 1550 nm setup was likely due to the difference in the Si lens integrated with the emitters.

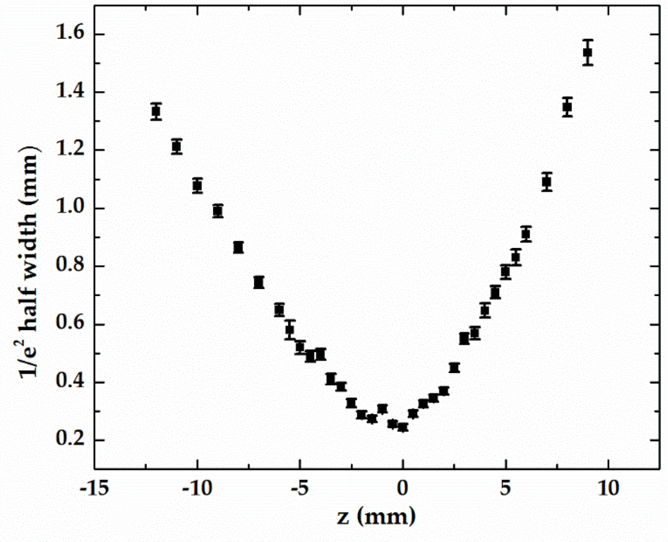

Figure 5.10: 1/e^2 half-width of the radiation spot from the TOPTICA 1550 nm emitter as a function of distance from the focal point.

5.4.2.3 Bandwidth measurement

The experimental apparatus shown in Figure 5.8 (but without the THz QCL), was used to measure the frequency response of the 1550 nm TOPTICA emitter and receiver. The system was purged with dry air to a humidity level < 5% to remove any artefacts due to water absorption. The heterodyne frequency was tuned from 50 GHz to 2.5 THz at a step size of 10 GHz. Frequency and amplitude was obtained from sine function fitting of the lock-in amplifier detected signal. Figure 5.11 (a) shows the fitted amplitude as a function of the heterodyne frequency for 1550 nm TOPTICA emitter and receiver. Figure 5.11 (b) shows the time-domain CW signal detected at 2 THz heterodyne frequency as black dots. Red solid line represents sinusoidal fit to the data. Detected signal amplitude close to 2 THz was similar for both 780 nm and 1550 nm photomixers.

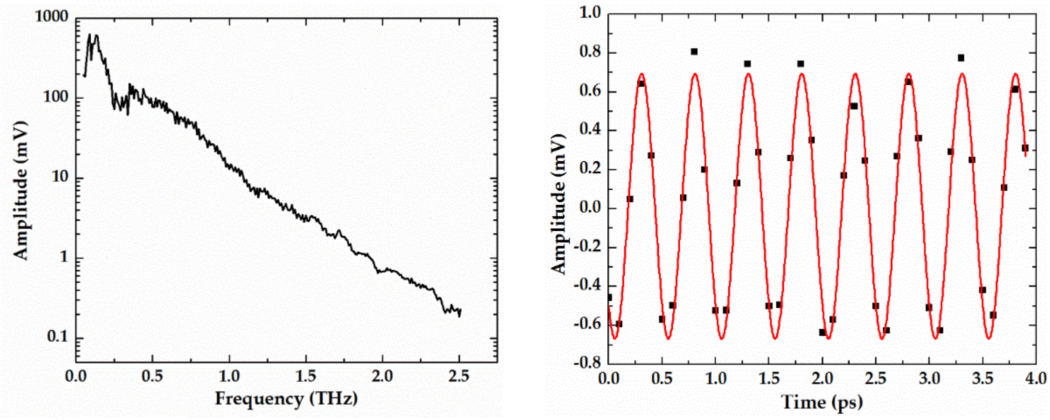

(a) **(b)**

Figure 5.11: (a) The dependence of fitted amplitude on the heterodyne frequency of 1550 nm TOPTICA emitter and receiver. (b) Coherently detected time-domain response at 2 THz heterodyne frequency (black dots). Single frequency sinusoidal fit shown as solid red line.

5.4.3 Results

In the 780 nm experimental apparatus, the spot size of the focussed CW-THz radiation from the emitter was much bigger than the aperture in front of the THz QCL. The smaller spot size measured here is close to the mode size of the QCL and should result in much better coupling.

5.4.3.1 QCL voltage modulation due to emitter

The voltage of the QCL was measured using a lock-in amplifier with the SMU in constant current mode. The modulation frequency was that of the emitter. Any perturbation in the device bias due to the emitter could be measured and would be helpful in aligning the facet to the incident radiation. In order to align the device, first the radiation going through the aperture and detected by the receiver was maximised by aligning the cryostat in XYZ direction using manual micrometers. This ensured that the device was close to focal plane. The cryostat was then very careful aligned to focus the CW-THz radiation from the emitter onto the THz QCL facet. A strong signal on the lock-in amplifier connected to the QCL power supply was detected. QCL position was adjusted to maximise this signal on the lock-in amplifier.

As this signal was modulated at the emitter modulation frequency, it has been referred to as the QCL voltage modulation signal. This signal was very sensitive to the alignment between the THz QCL and the emitter. It is believed that the THz QCL emission gets reflected from the emitter and perturbs the laser cavity causing effects similar to self-mixing in THz QCLs [253, 254]. In self-mixing the laser light reflected back into the laser cavity from an object causes perturbation in its threshold gain, power, voltage and spectrum. It is hypothesised that the reflected THz QCL emission was modulated due to change in surface reflectivity of the emitter. Aligning the THz QCL to the voltage modulation signal was effectively aligning the emitter radiation spot onto the facet of the THz QCL.

Although the voltage modulation signal was independent of the heterodyne frequency, it was strongly dependent on the emitter modulation frequency. The amplitude of the QCL voltage modulation increased with decrease in the emitter modulation frequency as reflected signal perturbed the laser cavity for longer time period. Figure 5.12 shows the QCL voltage modulation signal measured as the emitter modulation frequency was changed. The error bar represents the fluctuations in the measured signal. This strong dependence of signal on modulation frequency suggests that the effect may be thermal in origin. The instability of the voltage modulation signal increased at lower emitter modulation frequencies. 7.6 kHz emitter modulation frequency was used to carry out all further measurements.

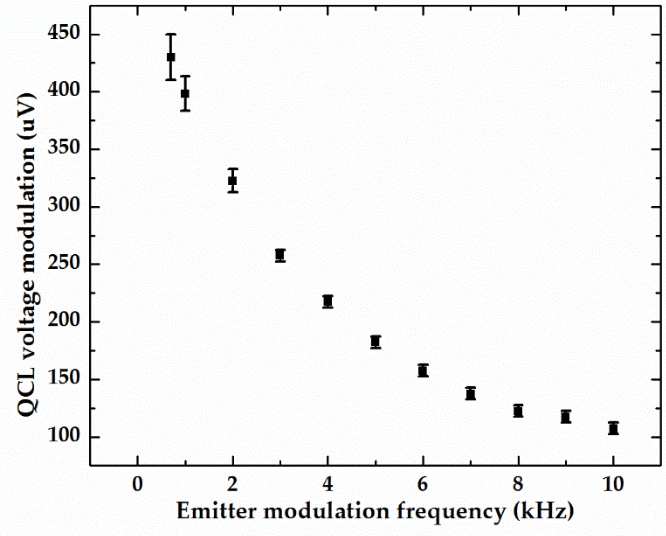

Figure 5.12: Voltage modulation of the THz QCL as function of emitter modulation frequency. Fluctuations in the lock-in signal represented as error bars.

5.4.3.2 Coherent detection with TOPTICA receiver

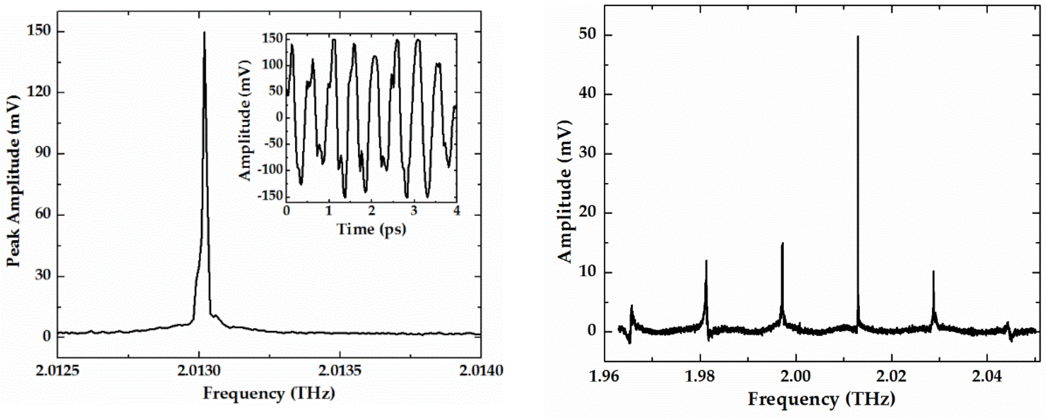

(a) **(b)**

Figure 5.13: (a) Injection locked peak amplitude as function of heterodyne frequency. (Inset) Coherently detected time-domain signal at 2.013 THz heterodyne frequency with the QCL switched on. (b) Fabry–Pérot modes of the THz QCL detected by changing the frequency of the injected CW radiation.

Having aligned the THz QCL to the focussed emitter radiation, the heterodyne frequency was stepped at 10 MHz close to the THz QCL's primary emission frequency and the signal on the receiver was monitored. THz QCL emission line was detected similar to the one shown in Figure 5.13 (a). The detected signal amplitude was improved by further fine aligning the THz QCL. At this point, it is worth mentioning that the signal amplitude was very sensitive to even a gentle touch on the micrometers of the QCL cryostat stage. The receiver was then translated for a short distance close to the zero path delay position to obtain fringes at each step of heterodyne frequency. The peak amplitude detected at each heterodyne frequency step with the THz QCL biased with 750 mA of constant current is shown in Figure 5.13 (a). The inset in the figure shows the time-domain trace of the signal detected on the receiver at 2.013 THz heterodyne frequency with the QCL switched on. The time-domain signal with QCL switched on is much larger in amplitude as compared to the time-domain signal without the QCL as already shown in Figure 5.11 (b). The signal disappeared when the emitter bias was turned off or the emitter radiation was blocked. Hence, the sharp peak close to the THz QCL emission line shows that the device was injection locked to the phase of the emitter radiation. The peak signal detected on the lock-in amplifier was >150 mV. The absolute value of the heterodyne frequency might deviate by couple of GHz as the measured centre frequency of the free running THz QCL was close to 2.015 THz (see Figure 5.2 (b)) as compared to the peak at 2.01302 THz heterodyne frequency (see Figure 5.13 (a)). The frequency difference could also be due to slight change in ambient air temperature.

To estimate the fraction of QCL power locked, the QCL and the TOPTICA emitter (at 2 THz) power measured directly on a helium cooled bolometer was 8.97 V and 1.63 mV respectively. The ratio of powers is close to 5053. Therefore ratio of expected electric field would be $\sqrt{5053} \approx 71$. The emitter field measured on the receiver was 2 mV, hence the expected field measured from the QCL would be 71*2=142 mV approximately. This value was in agreement to the field measured from the injection locked THz QCL as shown in Figure 5.13 (a).

The heterodyne frequency was swept from 1.963 THz to 2.050 THz in steps of 10 MHz (minimum tuning step of SANTEC laser) and the signal on the receiver was monitored. The plot of the detected signal with heterodyne frequency is shown in Figure 5.13 (b). Six Fabry–Pérot modes of the THz QCL spaced at ~16 GHz was observed. The mode spacing is in good agreement with the calculated value. It does suggest that injected radiation at Fabry–Pérot mode spacing initiated lasing phase locked to the incident CW radiation. In this scan the amplitude of the primary mode was less than 150 mV because of the phase of the CW signal being detected. Translating the delay stage with heterodyne frequency at the primary QCL mode confirmed higher detected amplitude.

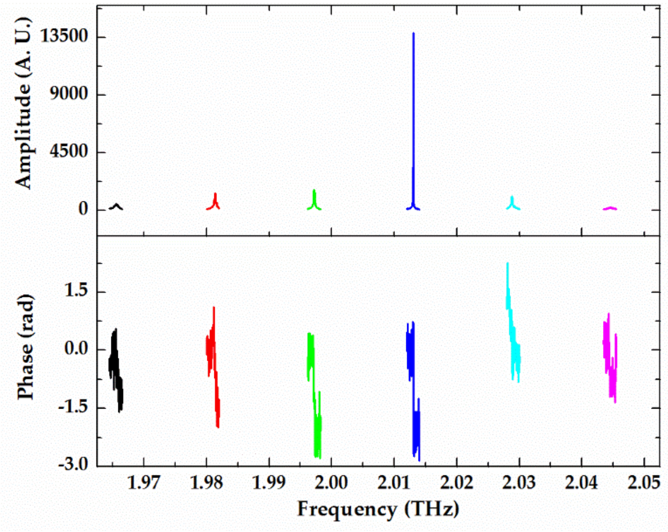

Figure 5.14: Amplitude and phase obtained at each Fabry–Pérot modes from injection locked THz QCL.

A phase-resolved scan of each of the Fabry–Pérot modes was performed to obtain the CW sinusoidal fringes. The heterodyne frequency was scanned over a close range encompassing each mode at a step of 10 MHz. At each heterodyne frequency step, the emitter was translated over a short distance, signal was recorded and Fast Fourier Transformed. Amplitude and phase of the FFT at the six different modes is plotted in Figure 5.14. For each mode the signal phase changes significantly as the heterodyne frequency sweeps across it.

The QCL voltage modulation signal was also measured close to the primary emission mode. The heterodyne frequency was tuned across primary mode of the THz QCL in a range of 1 GHz at step of 10 MHz. Three identical scans of the QCL voltage modulation was performed and is shown in Figure 5.15. As the heterodyne frequency hits the QCL emission frequency there is a sharp change in the modulation voltage. At this point, the voltage modulation was no longer independent of the heterodyne frequency as the incident radiation from the emitter interacted with the laser dynamics. Away from the mode, voltage modulation was independent of the heterodyne frequency as already mentioned earlier.

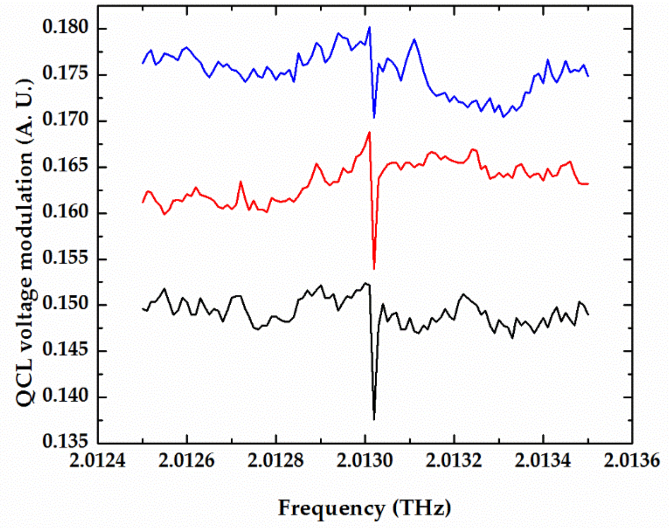

Figure 5.15: Three repeated scans of QCL voltage modulation signal measured with heterodyne frequency scanned close to the primary lasing mode.

5.4.4 Discussion

For a completely injection locked laser, the output power is fixed to the overall gain of the laser cavity and laser frequency (ω_0) is dominated by the injected signal frequency (ω_1) within the 'locking-range' of the injection locked laser [250]. This is true for an injected signal weaker than the laser output. Hence, in a plot of locked output power as a function of frequency, a 'flat top' is expected when ω_1 is detuned with the locking range of the injection locked laser and is illustrated as solid blue lines in Figure 5.16. Injected signal frequency outside the locking range does not interact the laser cavity and the output is that of the free running laser as shown by solid pink lines in Figure 5.16.

In this work, locking range of the THz QCL could not be determined as the coherently detected signals had a sharp peak (see Figure 5.13 (a) and (b), and Figure 5.14). It is believed that inability to determine locking range is due to the ~25 MHz frequency jitter in the combined output of the 1550 nm lasers used (see Figure 5.9). As the locking range cannot be determined, THz QCL cannot be assumed to be fully locked to the injected signal from the photomixer. As previously mentioned, the calculations of expected THz QCL signal on the receiver shows that almost all the power was being detected. Hence, the frequency jitter could be close to the locking range of the THz QCL used. To map out the 'flat top' within the locking range, there is a need to reduce the frequency jitter from the source. In the next chapter, this has been proposed as the future work of this project. Finally, the locking range (ω_{range}) could be increased by increasing the injected power (P_{inj}) as suggested by Alder's equation [250]: $\omega_{range} \propto \sqrt{\frac{P_{inj}}{P_{osc}}}$, where P_{osc} is the THz QCL output power.

Within the locking range regime, the injection locked laser's output frequency will follow any frequency change in the injected signal. In doing so, the output phase of the cavity changes with respect to the injected signal phase, to compensate for the change in lasing frequency. The phase change accommodated by the cavity across the locking range is π radians [250]. In an ideal injection locked oscillator, the phase response ($\phi(\omega_1)$) by detuning the injection frequency across the locking range is expected to follow an arcsine function as described by the equation [250] $\phi(\omega_1) = \sin^{-1}\left(\frac{\omega_0-\omega_1}{\omega_m}\right)$, where ω_m is the half locking range. This is shown as solid red line in Figure 5.16. This condition is valid for weak injection signals.

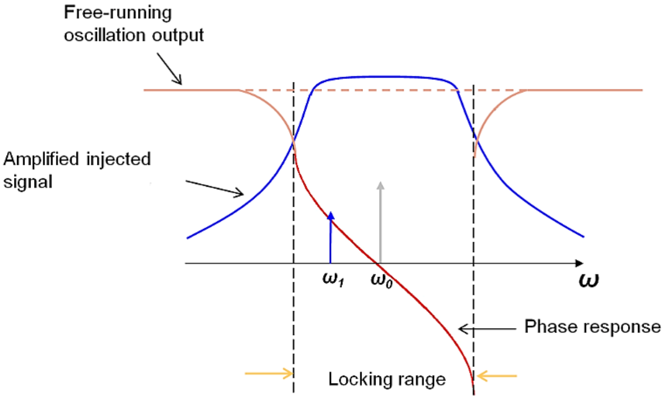

Figure 5.16: Response of injection locked laser within and outside its locking range. Image modified from Ref. [250].

The phase response measured in this work has already been shown in Figure 5.14. As the injected signal could not sample enough points across the locking range, the expected phase characteristics could not be measured. But a sudden change in phase of the laser cavity when the injected frequency was locked is evident from the plot for each of the Fabry–Pérot modes coherently detected.

5.4.5 Spectra under THz injection-locking

The results so far do not reveal the entire spectra of the device when injection locked to one of the modes because only those phase-locked are detectable. The experimental configuration was modified to include a Michelson Interferometer to measure the output spectra of the device. Radiation from the TOPTICA emitter was injected onto a facet of the THz QCL and the output from the other facet was detected through the interferometer using a helium cooled Si bolometer. The experimental setup is shown in Figure 5.17.

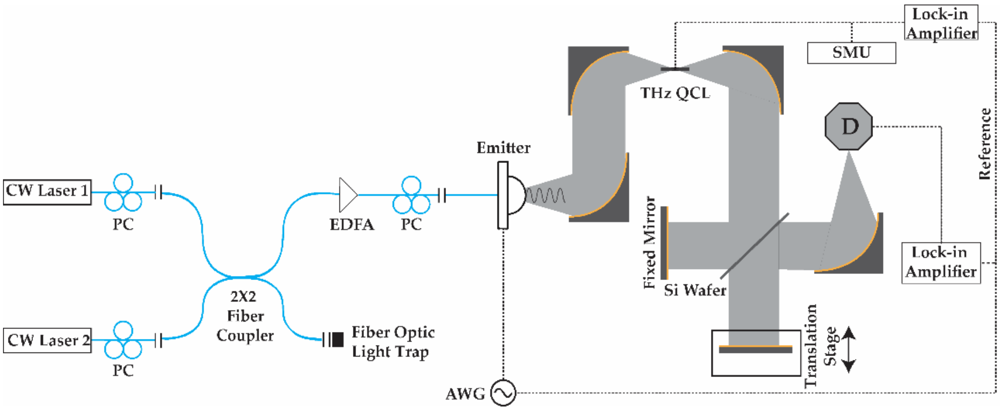

Figure 5.17: Schematic of injection locked THz QCL to measure spectra.

The THz QCL biased at 750 mA of constant current was first aligned to the interferometer. The radiation from TOPTICA emitter was then focussed onto the other facet and aligned by maximising the QCL voltage modulation signal as done previously. The interferogram was obtained by translating the moving mirror in the interferometer over a long distance (1.08 m, ~3600 ps) and recording the output from the bolometer. The FFT frequency resolution of the interferogram was ~280 MHz.

With the emitter turned off, the centre frequency of the free running THz QCL was measured to be 2.01504 THz. With the emitter turned on, the heterodyne frequency was scanned across a Fabry–Pérot mode ~16 GHz lower than primary mode of the laser. The scan range was from 1996.8 GHz to 1997.4 GHz in steps of 10 MHz. The range was determined from the injection locking scan done previously (see Figure 5.13 (b)). At each heterodyne frequency the interferogram was recorded. A number of spectra at various heterodyne frequency within the given scan range is shown in Figure 5.18. The laser's primary lasing mode switched to the lower Fabry–Pérot mode and then reverted back. The FFT scans suggests that the cavity was successfully locked to the lower Fabry–Pérot lasing mode (1.99921 THz) over a range of ~150 MHz.

Unfortunately, these scans were not very repeatable. Similar effects could not always be observed in heterodyne scans of other Fabry–Pérot modes. It is most likely due to the very challenging alignment of the injected CW-THz from the emitter to the facet of the THz QCL. Previously, the presence of the receiver allowed alignment through coherent detection of injection locked signal. In this setup, there was no way to measure and improve the alignment of injection locked signal.

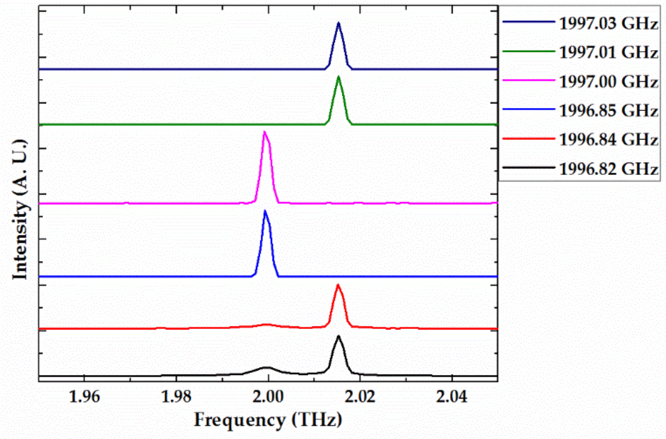

Figure 5.18: Hopping of the THz QCL emission frequency as it injection locks to a Fabry–Pérot mode.

5.5 Summary

CW-injection locking of a bound-to-continuum THz QCL was attempted using the TOPTICA 780 nm photomixers. Locking was unsuccessful due to large spot size of the incident CW-THz radiation from the emitter onto the facet of the THz QCL and the large jitter of the 780 nm lasers. The two 780 nm optical beams were directly mixed onto the facet of the laser but locking could not be achieved. Free running THz QCL was focused onto the receiver and beating was monitored on an electrical spectrum analyser. Again, no signal could be detected on the ESA. Unfortunately, the noise of the system was too high to detect any signal from the THz QCL. Narrowband CW optical injection seeding was also performed at Ruhr-Universität Bochum, Germany. Although heating effects of the optical radiation could be observed, emission frequency of the THz QCL could not be tuned with seed frequency.

Finally, photomixers and optical lasers at 780 nm were replaced with the ones operating at 1550 nm. The focussed CW-THz spot size and the combined linewidth of the diode lasers was much smaller than the 780 nm setup. A voltage across the THz QCL modulated at the emitter bias frequency was detected while aligning the laser to the focus of CW-THz radiation from the emitter. It was due to the effect similar to self-mixing in THz QCLs. The heterodyne frequency scan close to the THz QCL emission mode resulted in detection of Fabry–Pérot modes of the laser. A Change in detected signal phase and QCL voltage modulation signal at the injection locked modes was observed. Output frequency spectra of CW-injection locked THz QCL was measured. Although mode hoping from primary lasing mode to a Fabry–Pérot mode was measured, but the scans were not repeatable possibly due to poor alignment of the CW-injected radiation.

Chapter 6

Conclusions and future work

6.1 Conclusions

In this thesis, it was shown that THz QCLs can be used to construct a diffuse reflectance imaging system using bolometric detection (Section 6.1.1). Unfortunately this incoherent detection scheme does not enable the direct recovery of amplitude and phase information. Hence, an alternative approach was investigated in which the generation of continuous-wave THz radiation using photomixing was optimized (Section 6.1.2), and then used to injection lock a THz QCL (Section 6.1.3). This opens up the possibility of coherent detection of radiation from a THz QCL, and the chapter concludes by considering future prospects for this injection locked system (Section 6.2).

6.1.1 Diffuse reflectance imaging

An electrically, frequency-tuneable, THz QCL was used as a source to measure diffuse reflectance from a range of powdered samples, with a helium-cooled Si bolometer being used as the detector. A new 'effective-optical-path-length (EOPL)', and the well-known Kubelka–Munk (KM), model were used to infer absorption coefficients from the relative strengths of the diffuse reflectance data. The inferred absorption coefficients were then compared with the Beer–Lambert absorption coefficients of the samples obtained from the well-established technique of THz time-domain spectroscopy (TDS). Although the basic assumptions of the EOPL model could arguably be considered as flawed, as it doesn't consider the THz radiation as a field incident on the powdered sample, but as a ray of light reflection/refracting from surface, the trends were consistent with those expected from a Beer–Lambert model of the absorption coefficient. The KM model gave good agreement with the Beer–Lambert absorption coefficient within a range of 2–10 mm^{-1} through using a scaling factor associated with each specific material.

This work could be extended in the future to determine the effect of parameters such as the polarisation and incident angle of the THz radiation on the relative diffuse reflectance of the samples. It should be noted that measurements of very highly absorbing samples cannot be achieved using THz TDS in a transmission geometry. However, diffuse reflectance imaging *can* be used to measure the reflectance signature of these samples (as demonstrated in this thesis for ammonium nitrate).

The system could also be optimised for an improved focus of the THz radiation, enabling determination of powder distribution and segregation within a sample. THz QCLs based on discrete Vernier tuning [255], external cavities [256] or aperiodic gratings [257] would also enable tuning of the frequency for the diffuse reflectance imaging system over a far greater range. However, the technique of self-mixing using THz QCL was demonstrated in 2011 [254], and was subsequently shown to allow three-dimensional imaging of samples [123]. Here, the THz QCL not only acts like a source but also a very sensitive (coherent) detector, and it seems likely that future reflection imaging work with QCLs will focus on using this approach.

6.1.2 Photomixing

Continuous-wave THz radiation was generated and detected using commercially-purchased external cavity diode lasers, and photomixers operating at ~780 nm. A maximum emission bandwidth of >3 THz was obtained when using TOPTICA photomixers as the source and detector. Log-spiral antennas with interdigitated electrodes were also designed and fabricated in-house on an LTG-GaAs substrate, and used as photomixers. The effect on bandwidth of the emitter for a range of ex-situ annealing temperatures was studied, and photocurrent correlation technique used to measure carrier lifetimes. The same photomixer design was also fabricated on near identical LTG-GaAs wafers grown under similar MBE conditions but at different times. The quality of growth was found to have a much more significant impact on the material's bandwidth and carrier lifetime than the annealing temperature. The hyperfine absorption features of $LiYF_4$-Ho crystal were then measured around 700 GHz using, for the first time, a photomixing approach.

Apart from optimising further the electrode and antenna designs, transfer of the photoconductive material (LTG-GaAs in this case) onto a quartz substrate could significantly reduce the dark current. This reduction would lead to low background noise and potentially allow higher bias to be applied. This could enable an increase in the emitted THz power and overall bandwidth of the system.

6.1.3 Injection locking of a THz QCL

Having investigated imaging and spectroscopy systems based on THz QCLs and photomixing, research then focused on injection-locking a THz QCL with CW THz radiation. Initially, the 780 nm TOPTICA photomixers were used with a semi-insulating surface plasmon (SISP) waveguide THz QCL operating single mode at ~2 THz. No injection locking was seen, probably because the $1/e^2$ half-width of the focussed THz spot size was ~1.83 mm compared to the 14 μm x 150 μm facet of the QCL. The 780 nm experimental configuration was replaced with apparatus operating at a 1550 nm telecommunications wavelength. The frequency jitter in the lasers were found to be much less than the 780 nm lasers, and the focused THz spot size was also ~0.24 mm. The same THz QCL was used, and an injection locked signal was detected. Six different Fabry–Pérot modes of the THz QCL were coherently detected by tuning the beat frequency. It was calculated that close to 100% of the THz QCL emission was injection locked to the radiation from the emitter. An attempt was also made to understand the spectral characteristics of the THz QCL during injection locking. The CW THz signal was injected in one facet, and radiation from the other facet was monitored using an FTIR system. Unfortunately, the results were not conclusive. This probably arose from the difficulty of aligning the THz spot on the facet of the QCL, and into the FTIR.

The future possibilities for improving and further developing the injection locking of THz QCLs is discussed in the next section.

6.2 Further work on injection locking of THz QCLs

Although, in the work described in this thesis, 5–6 injection locked Fabry–Pérot modes were coherently detected, the study could not confirm the spectra of the THz QCL when it was injection locked to a particular mode. Spectra taken so far demonstrate hopping of the primary emission mode to an injection locked Fabry–Pérot mode, but these results were not fully repeatable and similar hopping could not be verified for other injection locked modes. A specific problem was that the experimental configuration used did not allow simultaneous coherent detection of the THz QCL signal as there was no photoconductive receiver in the system (see Figure 5.17). As a result, the injected THz beam could only be aligned using the selfmixed THz QCL voltage modulation signal and further fine alignment using the coherently-detected injection-locked signal was not possible. The configuration can, however, be modified to include the TOPTICA photomixer receiver for coherent detection as shown in Figure 6.1. The THz QCL radiation directed towards the FTIR section is split and focused onto the photomixer receiver. Thus, the signal from THz QCL can be coherently detected for alignment, and precise measurement of the output spectra can be performed. This forms the immediate next step in studying this injection-locking approach.

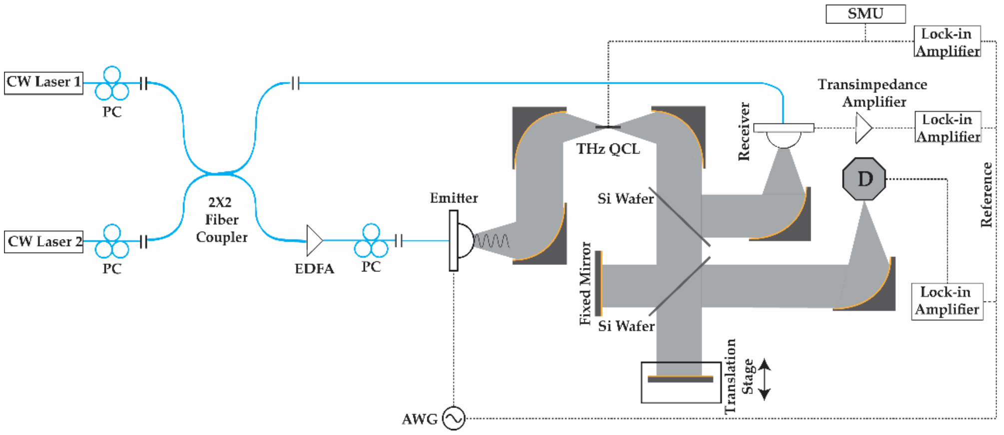

Figure 6.1: Schematic showing measurement of the spectra from an injection-locked THz QCL, including coherent detection using a photomixer receiver.

A further difficulty with the work to date has been that two free running diode lasers operating at ~1550 nm have been used. The combined frequency jitter was ~25 MHz (see Figure 6.2 (a)). Reducing this jitter would stabilise locking and increase the spectral resolution for spectroscopy applications Optical frequency comb generation techniques are one route to reducing this frequency jitter [258].

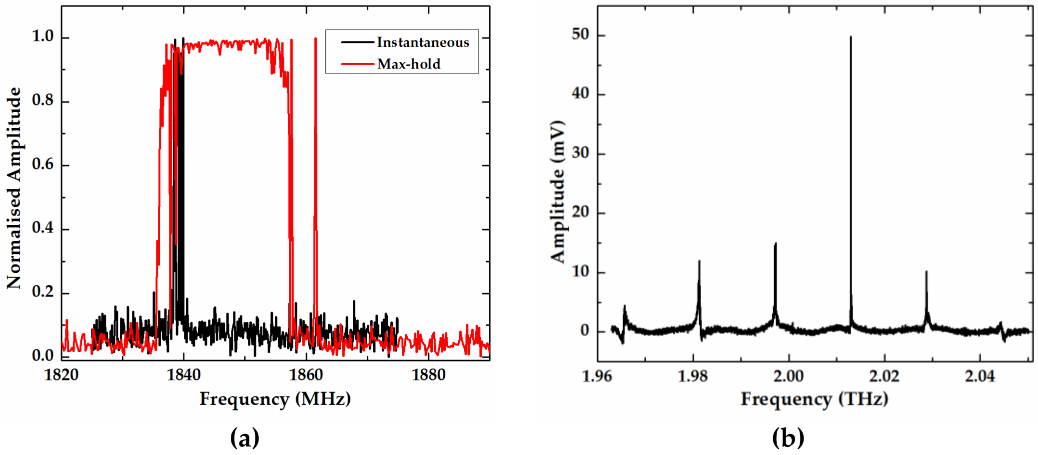

Figure 6.2: (a) Instantaneous linewidth of beating the 1550 nm lasers on InGaAs based photodiode shown in black (RBW: 110 kHz). Linewidth measured over a time of 3 minutes using max-hold function of the ESA shown in red (RBW: 220 kHz). Replicated from Figure 5.9. (b) Fabry–Pérot modes of the THz QCL detected by changing the frequency of the injected CW radiation. Replicated from Figure 5.13 (b).

In terms of applications, it would be desirable to have THz QCLs with a higher operating temperature, and a broader frequency tuning range. Operating temperature above 77 K (the liquid nitrogen boiling point) would reduce the system's operational cost, but at present the CW output powers >77 K are typically too low for practical use, especially when utilising single-plasmon waveguides, and this is an important area for future development.

An increased frequency tuning range is extremely beneficial for achieving spectroscopy over a broad range of materials. The THz QCL used in this work could be discretely injection locked over a frequency range of approximately 80 GHz (see Figure 6.2 (b)). This was intrinsically limited by the gain bandwidth of the THz QCL, which used a SISP waveguide. Double metal THz QCL waveguide geometries not only offer the best temperature performance [2], but also offer ultra-broadband emission frequency, with > ~1 THz demonstrated in both continuous-wave and pulsed mode. [259]. By incorporating a double-metal waveguide QCL into the injection-locking system, a greatly improved performance would be expected, albeit with greater difficulty in achieving alignment. However, in Ref. [260], the authors integrated a terahertz seeding section within the THz QCL cavity. Femtosecond laser pulses focussed on the seeding section generated THz pulses which injection seeded the THz QCL active region. This method avoids alignment of THz pulses from a photoconductive switch onto the facet of THz QCL for injection seeding [251], and would be highly desirable, provided highly-efficient photomixing could be obtained on the facet. In a similar way, a THz QCL integrated with a fiber coupled photomixing section would make the injection locking setup more robust. Combined with a double-metal waveguide geometry, integrated injection locked THz QCLs could then be developed with improved temperature and emission bandwidth.

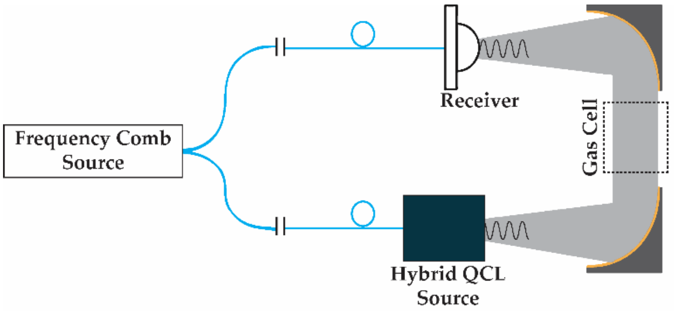

Figure 6.3: Schematic showing an integrated injection locked THz QCL being used for spectroscopy, and locked to a frequency comb.

Bibliography

[1] A. G. Davies, E. H. Linfield, and M. Davies, "Preface," *Philosophical Transactions of the Royal Society of London. Series A: Mathematical, Physical and Engineering Sciences,* vol. 362, p. 197, 2004.

[2] B. S. Williams, "Terahertz quantum-cascade lasers," *Nature Photonics,* vol. 1, pp. 517-525, 2007.

[3] C. Sirtori, "Applied physics: Bridge for the terahertz gap," *Nature,* vol. 417, pp. 132-133, 2002.

[4] H. Rubens and E. F. Nichols, "Heat Rays Of Great Wave Length," *Physical Review (Series I),* vol. 4, pp. 314-323, 1897.

[5] J. M. Chamberlain, "Where optics meets electronics: recent progress in decreasing the terahertz gap," *Philosophical Transactions of the Royal Society of London. Series A: Mathematical, Physical and Engineering Sciences,* vol. 362, pp. 199-213, 2004.

[6] A. G. Davies, E. H. Linfield, and M. B. Johnston, "The development of terahertz sources and their applications," *Physics in Medicine and Biology,* vol. 47, pp. 3679-3689, 2002.

[7] C. Kulesa, "Terahertz spectroscopy for astronomy: from comets to cosmology," *IEEE Transactions on Terahertz Science and Technology,* vol. 1, pp. 232-40, 2011.

[8] A. G. Davies, A. D. Burnett, W. Fan, E. H. Linfield, and J. E. Cunningham, "Terahertz spectroscopy of explosives and drugs," *Materials Today,* vol. 11, pp. 18–26, 2008.

[9] K. Kawase, Y. Ogawa, Y. Watanabe, and H. Inoue, "Non-destructive terahertz imaging of illicit drugs using spectral fingerprints," *Opt. Express,* vol. 11, pp. 2549-2554, 2003.

[10] P. F. Taday, "Applications of terahertz spectroscopy to pharmaceutical sciences," *Philosophical Transactions of the Royal Society of London A: Mathematical, Physical and Engineering Sciences,* vol. 362, pp. 351-364, 2004.

[11] A. D. Burnett, W. Fan, P. C. Upadhya, J. E. Cunningham, M. D. Hargreaves, T. Munshi, *et al.*, "Broadband terahertz time-domain spectroscopy of drugs-of-abuse and the use of principal component analysis," *Analyst,* vol. 134, pp. 1658-1668, 2009.

[12] X. Wang, D. J. Hilton, L. Ren, D. M. Mittleman, J. Kono, and J. L. Reno, "Terahertz time-domain magnetospectroscopy of a high-mobility two-dimensional electron gas," *Optics Letters,* vol. 32, pp. 1845-1847, 2007.

[13] P. Haring Bolívar, M. Nagel, F. Richter, M. Brucherseifer, H. Kurz, A. Bosserhoff, *et al.*, "Label–free THz sensing of genetic sequences: towards 'THz biochips'," *Philosophical Transactions of the Royal Society of London A: Mathematical, Physical and Engineering Sciences,* vol. 362, pp. 323-335, 2004.

[14] B. B. Hu and M. C. Nuss, "Imaging with terahertz waves," *Opt. Lett.,* vol. 20, pp. 1716-1718, 1995.

[15] R. M. Woodward, V. P. Wallace, R. J. Pye, B. E. Cole, D. D. Arnone, E. H. Linfield, *et al.*, "Terahertz pulse imaging of ex vivo basal cell carcinoma," *J. Investig. Dermatol.,* vol. 120, pp. 72–78, 2003.

[16] V. P. Wallace, A. J. Fitzgerald, S. Shankar, N. Flanagan, R. Pye, J. Cluff, *et al.*, "Terahertz pulsed imaging of basal cell carcinoma ex vivo and in vivo," *British Journal of Dermatology,* vol. 151, pp. 424–432, 2004.

[17] A. J. Fitzgerald, V. P. Wallace, M. Jimenez-Linan, L. Bobrow, R. J. Pye, A. D. Purushotham, *et al.*, "Terahertz pulsed imaging of human breast tumors," *Radiology,* vol. 239, pp. 533-540, 2006.

[18] B. Karagoz, H. Altan, and K. Kamburoglu, "Terahertz pulsed imaging study of dental caries," 2015, pp. 95420N-95420N-8.

[19] S. Ho-Jin and T. Nagatsuma, "Present and Future of Terahertz Communications," *Terahertz Science and Technology, IEEE Transactions on,* vol. 1, pp. 256-263, 2011.

[20] J. Federici and L. Moeller, "Review of terahertz and subterahertz wireless communications," *Journal of Applied Physics,* vol. 107, p. 111101, 2010.

[21] P. H. Siegel, "THz for space: The golden age," in *Microwave Symposium Digest (MTT), 2010 IEEE MTT-S International*, 2010, pp. 816-819.

[22] H.-J. Song and T. Nagatsuma, *Handbook of terahertz technologies: devices and applications*. Boca Raton, FL: CRC Press LLC, 2015.

[23] M. Perenzoni and D. J. Paul, *Physics and Applications of Terahertz Radiation*: Springer Science+Business Media Dordrecht, 2014.

[24] R. A. Lewis, *Terahertz Physics*: Cambridge University Press, 2013.

[25] D. Saeedkia, *Handbook of Terahertz Technology for Imaging, Sensing and Communications*: Woodhead Publishing, 2013.

[26] E. Bründermann, H.-W. Hübers, and M. F. Kimmitt, *Terahertz Techniques*: Springer-Verlag Berlin Heidelberg, 2012.

[27] X.-C. Zhang and J. Xu, *Introduction to THz Wave Photonics*: Springer US, 2010.

[28] Y.-S. Lee, *Principles of Terahertz Science and Technology*: Springer US, 2009.

[29] S. L. Dexheimer, *Terahertz Spectroscopy: Principles and Applications*: CRC Press, 2007.

[30] S. Ganichev and W. Prettl, *Intense Terahertz Excitation of Semiconductors*: Oxford University Press, 2006.

[31] K. Sakai, *Terahertz Optoelectronics*: Springer Berlin Heidelberg, 2005.

[32] P. D. Mittleman, *Sensing with Terahertz Radiation*: Springer Berlin Heidelberg, 2003.

[33] M. S. Vitiello, G. Scalari, B. Williams, and P. De Natale, "Quantum cascade lasers: 20 years of challenges," *Optics Express,* vol. 23, pp. 5167-5182, 2015.

[34] P. Dean, A. Valavanis, J. Keeley, K. Bertling, Y. L. Lim, R. Alhathlool, *et al.*, "Terahertz imaging using quantum cascade lasers—a review of systems and applications," *Journal of Physics D: Applied Physics,* vol. 47, p. 374008, 2014.

[35] S. Bartalini, M. S. Vitiello, and P. D. Natale, "Quantum cascade lasers: a versatile source for precise measurements in the mid/far-infrared range," *Measurement Science and Technology,* vol. 25, p. 012001, 2014.

[36] R. A. Lewis, "A review of terahertz sources," *Journal of Physics D: Applied Physics,* vol. 47, p. 374001, 2014.

[37] B. Ferguson and X.-C. Zhang, "Materials for terahertz science and technology," *Nat Mater,* vol. 1, pp. 26-33, 2002.

[38] P. H. Siegel, "Terahertz technology," *Microwave Theory and Techniques, IEEE Transactions on,* vol. 50, pp. 910-928, 2002.

[39] M. Tonouchi, "Cutting-edge terahertz technology," *Nat Photon,* vol. 1, pp. 97-105, 2007.

[40] C. A. Schmuttenmaer, "Exploring Dynamics in the Far-Infrared with Terahertz Spectroscopy," *Chemical Reviews,* vol. 104, pp. 1759-1780, 2004.

[41] P. H. Siegel, "Terahertz technology in biology and medicine," in *Microwave Symposium Digest, 2004 IEEE MTT-S International*, 2004, pp. 1575-1578 Vol.3.

[42] M. G. Krishna, S. D. Kshirsagar, and S. P. Tewari, *Terahertz Emitters, Detectors and Sensors: Current Status and Future Prospects*: InTech, 2012.

[43] J. A. Zeitler, P. F. Taday, D. A. Newnham, M. Pepper, K. C. Gordon, and T. Rades, "Terahertz pulsed spectroscopy and imaging in the pharmaceutical setting — a review," *Journal of Pharmacy and Pharmacology,* vol. 59, pp. 209–223, 2007.

[44] C. Wai Lam, D. Jason, and M. M. Daniel, "Imaging with terahertz radiation," *Reports on Progress in Physics,* vol. 70, p. 1325, 2007.

[45] E. Nichols and J. Tear, "Joining the infra-red and electric wave spectra," *The Astrophysical Journal,* vol. 61, pp. 17-37, 1925.

[46] M. Feiginov, H. Kanaya, S. Suzuki, and M. Asada, "Operation of resonant-tunneling diodes with strong back injection from the collector at frequencies up to 1.46 THz," *Applied Physics Letters,* vol. 104, p. 243509, 2014.

[47] A. Khalid, G. M. Dunn, R. F. Macpherson, S. Thoms, D. Macintyre, C. Li*, et al.*, "Terahertz oscillations in an In0.53Ga0.47As submicron planar Gunn diode," *Journal of Applied Physics,* vol. 115, p. 114502, 2014.

[48] L. N. Kurbatov, A. Britov, S. Karavaev, S. Sivachenko, S. Maksimovskii, I. Ovchinnikov, *et al.*, "Far-IR heterojunction lasers tunable to 46.2 microns," *JEPT Letters,* vol. 37, pp. 499-502, 1983.

[49] E. R. Brown, K. A. McIntosh, K. B. Nichols, and C. L. Dennis, "Photomixing up to 3.8 THz in low-temperature-grown GaAs," *Applied Physics Letters,* vol. 66, pp. 285-287, 1995.

[50] T. Masahiko, M. Osamu, M. Shuji, and H. Masanori, "Generation of terahertz radiation by photomixing with dual- and multiple-mode lasers," *Semiconductor Science and Technology,* vol. 20, p. S151, 2005.

[51] M. Beck, H. Schäfer, G. Klatt, J. Demsar, S. Winnerl, M. Helm, *et al.*, "Impulsive terahertz radiation with high electric fields from an amplifier-driven large-area photoconductive antenna," *Optics Express,* vol. 18, pp. 9251-9257, 2010.

[52] J. Zhang, Y. Hong, S. L. Braunstein, and K. A. Shore, "Terahertz pulse generation and detection with LT-GaAs photoconductive antenna," *Optoelectronics, IEE Proceedings -,* vol. 151, pp. 98-101, 2004.

[53] Y. J. Ding, "Progress in terahertz sources based on difference-frequency generation [Invited]," *Journal of the Optical Society of America B,* vol. 31, pp. 2696-2711, 2014.

[54] G. D. Boyd, T. J. Bridges, C. K. N. Patel, and E. Buehler, "Phase-matched submillimeter wave generation by difference-frequency mixing in ZnGeP2," *Applied Physics Letters,* vol. 21, pp. 553-555, 1972.

[55] W. Shi and Y. J. Ding, "Continuously tunable and coherent terahertz radiation by means of phase-matched difference-frequency generation in zinc germanium phosphide," *Applied Physics Letters,* vol. 83, pp. 848-850, 2003.

[56] J.-i. Shikata, K. Kawase, K. Karino, T. Taniuchi, and H. Ito, "Tunable terahertz-wave parametric oscillators using LiNbO₃ and MgO:LiNbO₃ crystals," *Microwave Theory and Techniques, IEEE Transactions on,* vol. 48, pp. 653-661, 2000.

[57] K. Radhanpura, S. Hargreaves, R. A. Lewis, L. Sirbu, and I. M. Tiginyanu, "Heavy noble gas (Kr, Xe) irradiated (111) InP nanoporous honeycomb membranes with enhanced ultrafast all-optical terahertz emission," *Applied Physics Letters,* vol. 97, p. 181921, 2010.

[58] S. Hargreaves, K. Radhanpura, and R. A. Lewis, "Generation of terahertz radiation by bulk and surface optical rectification from crystal planes of arbitrary orientation," *Physical Review B,* vol. 80, p. 195323, 2009.

[59] J. H. Booske, R. J. Dobbs, C. D. Joye, C. L. Kory, G. R. Neil, P. Gun-Sik, *et al.*, "Vacuum Electronic High Power Terahertz Sources," *Terahertz Science and Technology, IEEE Transactions on,* vol. 1, pp. 54-75, 2011.

[60] T. Y. Chang, T. J. Bridges, and E. G. Burkhardt, "CW submillimeter laser action in optically pumped methyl fluoride, methyl alcohol, and vinyl chloride gases," *Applied Physics Letters,* vol. 17, pp. 249-251, 1970.

[61] T. Y. Chang, "Optically Pumped Submillimeter-Wave Sources," *Microwave Theory and Techniques, IEEE Transactions on,* vol. 22, pp. 983-988, 1974.

[62] R. Haug, *Advances in Solid State Physics 47* vol. 47: Springer-Verlag Berlin Heidelberg, 2008.

[63] R. Kohler, A. Tredicucci, F. Beltram, H. E. Beere, E. H. Linfield, A. G. Davies, *et al.*, "Terahertz semiconductor-heterostructure laser," *Nature,* vol. 417, pp. 156-9, 2002.

[64] A. Bergner, U. Heugen, E. Bründermann, G. Schwaab, M. Havenith, D. R. Chamberlin, *et al.*, "New p-Ge THz laser spectrometer for the study of solutions: THz absorption spectroscopy of water," *Review of Scientific Instruments,* vol. 76, p. 063110, 2005.

[65] S. Fathololoumi, E. Dupont, I. C. Chan, Z. R. Wasilewski, S. R. Laframboise, D. Ban, *et al.*, "199.5 K Operation of THz Quantum Cascade Lasers," in *Conference on Lasers and Electro-Optics 2012*, San Jose, California, 2012, p. CTu2B.1.

[66] D. H. Auston, "Picosecond optoelectronic switching and gating in silicon," *Applied Physics Letters,* vol. 26, pp. 101-103, 1975.

[67] D. H. Auston, K. P. Cheung, and P. R. Smith, "Picosecond photoconducting Hertzian dipoles," *Applied Physics Letters,* vol. 45, pp. 284-286, 1984.

[68] D. H. Auston, A. M. Johnson, P. R. Smith, and J. C. Bean, "Picosecond optoelectronic detection, sampling, and correlation measurements in amorphous semiconductors," *Applied Physics Letters,* vol. 37, pp. 371-373, 1980.

[69] D. E. Spence, P. N. Kean, and W. Sibbett, "60-fsec pulse generation from a self-mode-locked Ti:sapphire laser," *Optics Letters,* vol. 16, pp. 42-44, 1991.

[70] X. C. Zhang, B. B. Hu, J. T. Darrow, and D. H. Auston, "Generation of femtosecond electromagnetic pulses from semiconductor surfaces," *Applied Physics Letters,* vol. 56, pp. 1011-1013, 1990.

[71] K. H. Yang, P. L. Richards, and Y. R. Shen, "Generation of Far-Infrared Radiation by Picosecond Light Pulses in LiNbO3," *Applied Physics Letters,* vol. 19, pp. 320-323, 1971.

[72] X. C. Zhang, X. F. Ma, Y. Jin, T. M. Lu, E. P. Boden, P. D. Phelps, *et al.*, "Terahertz optical rectification from a nonlinear organic crystal," *Applied Physics Letters,* vol. 61, pp. 3080-3082, 1992.

[73] A. Schneider, M. Neis, M. Stillhart, B. Ruiz, R. U. A. Khan, and P. Günter, "Generation of terahertz pulses through optical rectification in organic DAST crystals: theory and experiment," *Journal of the Optical Society of America B,* vol. 23, pp. 1822-1835, 2006.

[74] P. Gu, M. Tani, S. Kono, K. Sakai, and X.-C. Zhang, "Study of terahertz radiation from InAs and InSb," *Journal of Applied Physics,* vol. 91, pp. 5533-5537, 2002.

[75] K. Leo, J. Shah, E. O. Göbel, T. C. Damen, S. Schmitt-Rink, W. Schäfer, *et al.*, "Coherent oscillations of a wave packet in a semiconductor double-quantum-well structure," *Physical review letters,* vol. 66, p. 201, 1991.

[76] C. Waschke, H. G. Roskos, R. Schwedler, K. Leo, H. Kurz, and K. Köhler, "Coherent submillimeter-wave emission from Bloch oscillations in a semiconductor superlattice," *Physical review letters,* vol. 70, p. 3319, 1993.

[77] T. Dekorsy, H. Auer, C. Waschke, H. J. Bakker, H. G. Roskos, H. Kurz, *et al.*, "Emission of submillimeter electromagnetic waves by coherent phonons," *Physical review letters,* vol. 74, p. 738, 1995.

[78] M. Martin and E. R. Brown, "Critical comparison of GaAs and InGaAs THz photoconductors," in *Proc. SPIE 8261 Terahertz Technology and Applications V*, 2012, pp. 826102-826102-7.

[79] K. A. McIntosh, K. B. Nichols, S. Verghese, and E. R. Brown, "Investigation of ultrashort photocarrier relaxation times in low-temperature-grown GaAs," *Applied Physics Letters,* vol. 70, pp. 354-356, 1997.

[80] S. Gupta, M. Y. Frankel, J. A. Valdmanis, J. F. Whitaker, G. A. Mourou, F. W. Smith*, et al.*, "Subpicosecond carrier lifetime in GaAs grown by molecular beam epitaxy at low temperatures," *Applied Physics Letters,* vol. 59, pp. 3276-3278, 1991.

[81] P. R. Smith, D. H. Auston, and M. C. Nuss, "Subpicosecond photoconducting dipole antennas," *Quantum Electronics, IEEE Journal of,* vol. 24, pp. 255-260, 1988.

[82] Q. Wu and X.-C. Zhang, "7 terahertz broadband GaP electro-optic sensor," *Applied Physics Letters,* vol. 70, pp. 1784-1786, 1997.

[83] A. Leitenstorfer, S. Hunsche, J. Shah, M. C. Nuss, and W. H. Knox, "Detectors and sources for ultrabroadband electro-optic sampling: Experiment and theory," *Applied Physics Letters,* vol. 74, pp. 1516-1518, 1999.

[84] Y. C. Shen, P. C. Upadhya, E. H. Linfield, H. E. Beere, and A. G. Davies, "Ultrabroadband terahertz radiation from low-temperature-grown GaAs photoconductive emitters," *Applied Physics Letters,* vol. 83, pp. 3117-3119, 2003.

[85] A. D. Burnett, J. Kendrick, J. E. Cunningham, M. D. Hargreaves, T. Munshi, H. G. M. Edwards, *et al.*, "Calculation and measurement of terahertz active normal modes in crystalline PETN," *ChemPhysChem,* vol. 11, pp. 368-78, 2010.

[86] A. Tomasino, A. Parisi, S. Stivala, P. Livreri, A. C. Cino, A. C. Busacca, *et al.*, "Wideband THz Time Domain Spectroscopy based on Optical Rectification and Electro-Optic Sampling," *Sci. Rep.,* vol. 3, 2013.

[87] W. Zouaghi, M. D. Thomson, K. Rabia, R. Hahn, V. Blank, and H. G. Roskos, "Broadband terahertz spectroscopy: principles, fundamental research and potential for industrial applications," *European Journal of Physics,* vol. 34, p. S179, 2013.

[88] G. Mouret, S. Matton, R. Bocquet, F. Hindle, E. Peytavit, J. F. Lampin, *et al.*, "Far-infrared cw difference-frequency generation using vertically integrated and planar low temperature grown GaAs photomixers: application to H2S rotational spectrum up to 3 THz," *Applied Physics B,* vol. 79, pp. 725-729, 2004.

[89] I. C. Mayorga, A. Schmitz, T. Klein, C. Leinz, and R. Gusten, "First In-Field Application of a Full Photonic Local Oscillator to Terahertz Astronomy," *Terahertz Science and Technology, IEEE Transactions on,* vol. 2, pp. 393-399, 2012.

[90] L. P. Schmidt, S. Biber, G. Rehm, and K. Huber, "THz measurement technologies and applications," in *Microwaves, Radar and Wireless Communications, 2002. MIKON-2002. 14th International Conference on*, 2002, pp. 581-587 vol.2.

[91] M. Inguscio, G. Moruzzi, K. M. Evenson, and D. A. Jennings, "A review of frequency measurements of optically pumped lasers from 0.1 to 8 THz," *Journal of Applied Physics,* vol. 60, pp. R161-R192, 1986.

[92] K. Y. Kim, A. J. Taylor, J. H. Glownia, and RodriguezG, "Coherent control of terahertz supercontinuum generation in ultrafast laser-gas interactions," *Nat Photon,* vol. 2, pp. 605-609, 2008.

[93] E. R. Brown, J. R. Soderstrom, C. D. Parker, L. J. Mahoney, K. M. Molvar, and T. C. McGill, "Oscillations up to 712 GHz in InAs/AlSb resonant-tunneling diodes," *Applied Physics Letters,* vol. 58, pp. 2291-3, 1991.

[94] J. Ward, E. Schlecht, G. Chattopadhyay, A. Maestrini, J. Gill, F. Maiwald, *et al.*, "Capability of THz sources based on Schottky diode frequency multiplier chains," in *Microwave Symposium Digest, 2004 IEEE MTT-S International*, 2004, pp. 1587-1590 Vol.3.

[95] S. Barbieri, J. Alton, S. S. Dhillon, H. E. Beere, M. Evans, E. H. Linfield, *et al.*, "Continuous-wave operation of terahertz quantum-cascade lasers," *Quantum Electronics, IEEE Journal of,* vol. 39, pp. 586-591, 2003.

[96] Y. J. DING and W. SHI, "Widely-tunable, monochromatic, and high-power terahertz sources and their applications," *Journal of Nonlinear Optical Physics & Materials,* vol. 12, pp. 557-585, 2003.

[97] S. Verghese, K. A. McIntosh, S. Calawa, W. F. Dinatale, E. K. Duerr, and K. A. Molvar, "Generation and detection of coherent terahertz waves using two photomixers," *Applied Physics Letters,* vol. 73, pp. 3824-6, 1998.

[98] H. Tanoto, J. H. Teng, Q. Y. Wu, M. Sun, Z. N. Chen, S. A. Maier, *et al.*, "Nano-antenna in a photoconductive photomixer for highly efficient continuous wave terahertz emission," *Sci. Rep.,* vol. 3, 2013.

[99] C. W. Berry, M. R. Hashemi, S. Preu, H. Lu, A. C. Gossard, and M. Jarrahi, "Plasmonics enhanced photomixing for generating quasi-continuous-wave frequency-tunable terahertz radiation," *Optics Letters,* vol. 39, pp. 4522-4524, 2014.

[100] C. W. Berry, M. R. Hashemi, S. Preu, H. Lu, A. C. Gossard, and M. Jarrahi, "High power terahertz generation using 1550 nm plasmonic photomixers," *Applied Physics Letters,* vol. 105, p. 011121, 2014.

[101] H.-C. Ryu, "Folded dipole antenna for power enhancement of a terahertz photomixer," *Journal of the Korean Physical Society,* vol. 64, pp. 1556-1560, 2014.

[102] K. A. McIntosh, E. R. Brown, K. B. Nichols, O. B. McMahon, W. F. DiNatale, and T. M. Lyszczarz, "Terahertz photomixing with diode lasers in low-temperature-grown GaAs," *Applied Physics Letters,* vol. 67, pp. 3844-3846, 1995.

[103] R. F. Kazarinov and R. A. Suris, "Possibility of the amplification of electromagnetic waves in a semiconductor with a superlattice," *Fiz. Tekh. Poluprov.,* vol. 5, pp. 797-800, 1971.

[104] L. Esaki and R. Tsu, "Superlattice and Negative Differential Conductivity in Semiconductors," *IBM Journal of Research and Development,* vol. 14, pp. 61-65, 1970.

[105] J. Faist, F. Capasso, D. L. Sivco, C. Sirtori, A. L. Hutchinson, and A. Y. Cho, "Quantum Cascade Laser," *Science,* vol. 264, pp. 553-556, 1994.

[106] J. Faist, F. Capasso, C. Sirtori, D. L. Sivco, A. L. Hutchinson, and A. Y. Cho, "Continuous wave operation of a vertical transition quantum cascade laser above T=80 K," *Applied Physics Letters,* vol. 67, pp. 3057-3059, 1995.

[107] J. Faist, F. Capasso, C. Sirtori, D. L. Sivco, J. N. Baillargeon, A. L. Hutchinson, *et al.*, "High power mid-infrared (λ~5 μm) quantum cascade lasers operating above room temperature," *Applied Physics Letters,* vol. 68, pp. 3680-3682, 1996.

[108] Y. Yao, A. J. Hoffman, and C. F. Gmachl, "Mid-infrared quantum cascade lasers," *Nat Photon,* vol. 6, pp. 432-439, 2012.

[109] C. Gmachl, F. Capasso, D. L. Sivco, and A. Y. Cho, "Recent progress in quantum cascade lasers and applications," *Reports on Progress in Physics,* vol. 64, pp. 1533-601, 2001.

[110] L. Ajili, G. Scalari, D. Hofstetter, M. Beck, J. Faist, H. Beere, *et al.*, "Continuous-wave operation of far-infrared quantum cascade lasers," *Electronics Letters,* vol. 38, pp. 1675-6, 2002.

[111] C. Walther, M. Fischer, G. Scalari, R. Terazzi, N. Hoyler, and J. Faist, "Quantum cascade lasers operating from 1.2 to 1.6 THz," *Applied Physics Letters,* vol. 91, pp. 1-3, 2007.

[112] C. W. I. Chan, Q. Hu, and J. L. Reno, "Ground state terahertz quantum cascade lasers," *Applied Physics Letters,* vol. 101, p. 151108, 2012.

[113] M. Wienold, B. Röben, L. Schrottke, R. Sharma, A. Tahraoui, K. Biermann, *et al.*, "High-temperature, continuous-wave operation of terahertz quantum-cascade lasers with metal-metal waveguides and third-order distributed feedback," *Optics Express,* vol. 22, pp. 3334-3348, 2014.

[114] L. Lianhe, C. Li, Z. Jingxuan, J. Freeman, P. Dean, A. Valavanis, *et al.*, "Terahertz quantum cascade lasers with >1 W output powers," *Electronics Letters,* vol. 50, pp. 309-311, 2014.

[115] B. S. Williams, S. Kumar, Q. Hu, and J. L. Reno, "High-power terahertz quantum-cascade lasers," *Electronics Letters,* vol. 42, pp. 89–91, 2006.

[116] A. Wade, G. Fedorov, D. Smirnov, S. Kumar, B. S. Williams, Q. Hu, *et al.*, "Magnetic-field-assisted terahertz quantum cascade laser operating up to 225 K," *Nat Photon,* vol. 3, pp. 41-45, 2009.

[117] M. Fischer, G. Scalari, K. Celebi, M. Amanti, C. Walther, M. Beck, *et al.*, "Scattering processes in terahertz InGaAs/InAlAs quantum cascade lasers,"

Applied Physics Letters, vol. 97, p. 221114, 2010.

[118] C. Deutsch, M. Krall, M. Brandstetter, H. Detz, A. M. Andrews, P. Klang, *et al.*, "High performance InGaAs/GaAsSb terahertz quantum cascade lasers operating up to 142 K," *Applied Physics Letters,* vol. 101, p. 211117, 2012.

[119] V. Federico, S. Giacomo, O. Keita, B. Mattias, and F. Jérôme, "InGaAs/AlInGaAs THz quantum cascade lasers operating up to 195 K in strong magnetic field," *New Journal of Physics,* vol. 17, p. 023050, 2015.

[120] K. Ohtani, M. Fischer, G. Scalari, M. Beck, and J. Faist, "Terahertz intersubband electroluminescence from InAs quantum cascade light emitting structures," *Applied Physics Letters,* vol. 102, p. 141113, 2013.

[121] Q. Y. Lu, N. Bandyopadhyay, S. Slivken, Y. Bai, and M. Razeghi, "Room temperature single-mode terahertz sources based on intracavity difference-frequency generation in quantum cascade lasers," *Applied Physics Letters,* vol. 99, p. 131106, 2011.

[122] M. A. Belkin, F. Capasso, F. Xie, A. Belyanin, M. Fischer, A. Wittmann, *et al.*, "Room temperature terahertz quantum cascade laser source based on intracavity difference-frequency generation," *Applied Physics Letters,* vol. 92, p. 201101, 2008.

[123] P. Dean, A. Valavanis, J. Keeley, K. Bertling, Y. Leng Lim, R. Alhathlool, *et al.*, "Coherent three-dimensional terahertz imaging through self-mixing in a quantum cascade laser," *Applied Physics Letters,* vol. 103, p. 181112, 2013.

[124] J. Keeley, P. Dean, A. Valavanis, K. Bertling, Y. L. Lim, R. Alhathlool, *et al.*, "Three-dimensional terahertz imaging using swept-frequency feedback interferometry with a quantum cascade laser," *Optics Letters,* vol. 40, pp. 994-997, 2015.

[125] J. T. Keeley, P. Dean, A. Valavanis, K. Bertling, T. Taimre, Y. L. Lim, *et al.*, "Electrical modulation schemes for imaging by self-mixing in terahertz quantum cascade lasers," in *International Quantum Cascade Lasers Summer School and Workshop*, ed. Policoro, Italy, 2014.

[126] P. Dean, T. Taimre, A. Lui, K. Bertling, Y. L. Lim, A. Valavanis, *et al.*, "Coherent THz imaging using the self-mixing effect in quantum cascade lasers," in *Advanced Photonics*, Barcelona, 2014, p. SeTh4B.3.

[127] A. Scheuring, P. Dean, A. Valavanis, A. Stockhausen, P. Thoma, M. Salih, *et*

al., "Transient Analysis of THz-QCL Pulses Using NbN and YBCO Superconducting Detectors," *Terahertz Science and Technology, IEEE Transactions on,* vol. 3, pp. 172-179, 2013.

[128] A. Valavanis, P. Dean, A. Scheuring, M. Salih, A. Stockhausen, S. Wuensch, *et al.*, "Time-resolved measurement of pulse-to-pulse heating effects in a terahertz quantum cascade laser using an NbN superconducting detector," *Applied Physics Letters,* vol. 103, p. 061120, 2013.

[129] P. Dean, A. Valavanis, A. Scheuring, A. Stockhausen, P. Probst, M. Salih, *et al.*, "Ultra-fast sampling of terahertz pulses from a quantum cascade laser using superconducting antenna-coupled NbN and YBCO detectors," in *Infrared, Millimeter, and Terahertz Waves (IRMMW-THz), 2012 37th International Conference on*, 2012, pp. 1-2.

[130] A. Valavanis, P. Dean, A. Scheuring, M. Salih, A. Stockhausen, S. Wuensch, *et al.*, "Transient analysis of substrate heating effects in a terahertz quantum cascade laser using an ultrafast NbN superconducting detector," in *Infrared, Millimeter, and Terahertz Waves (IRMMW-THz), 2013 38th International Conference on*, 2013, pp. 1-2.

[131] A. Valavanis, P. Dean, A. Scheuring, M. Salih, S. P. Khanna, A. Stockhausen, *et al.*, "Time-resolved measurement of heating effects in a terahertz quantum cascade laser using an NbN superconducting detector," in *International Quantum Cascade Lasers School & Workshop 2012*, ed. Baden near Vienna, Austria, 2012.

[132] A. Scheuring, P. Dean, A. Valavanis, A. Stockhausen, P. Thoma, M. Salih, *et al.*, "Analysis of THz pulses of a Quantum Cascade Laser in the time-domain using superconducting direct detectors," in *Tagung Kryoelektronische Bauelemente 2012*, ed. Freudenstadt-Lauterbad, Germany, 2012.

[133] I. Kundu, "Frequency tunable terahertz quantum cascade lasers," PhD Thesis, School of Electronic and Electrical Engineering, University of Leeds, 2014.

[134] R. H. S. Alhathlool, "The Development and Applications of Terahertz Quantum Cascade Lasers," PhD Thesis, School of Electronic and Electrical Engineering, University of Leeds, 2014.

[135] M. S. b. M. Ibrahim, "Segmented and patterned single-metal terahertz quantum cascade lasers," PhD Thesis, School of Electronic and Electrical Engineering, University of Leeds, 2011.

[136] M. J. Madou, *Fundamentals of microfabrication and nanotechnology* vol. 3rd. Boca Raton, Fla; London: CRC, 2012.

[137] S. Franssila, *Introduction to microfabrication* vol. 2nd. Chichester: Wiley, 2010.

[138] *Dow Chemicals, Shipley Microposit(R) S100(R) Series Photo Resists (n.d.)*.

[139] A. G. Baca and C. I. H. Ashby, *Fabrication of GaAs Devices, EMIS Processing Series 6 (The Institution of Electrical Engineers, London, 2005), Vol 6*.

[140] M. Hatzakis, B. J. Canavello, and J. M. Shaw, "Single-Step Optical Lift-Off Process," *IBM Journal of Research and Development,* vol. 24, pp. 452-460, 1980.

[141] D. Jucknischke, H. J. Buhlmann, R. Houdre, M. Ilegems, M. A. Py, B. Jeckelmann, *et al.*, "Properties of alloyed AuGeNi-contacts on GaAs/Ga/AlAs-heterostructures," *Instrumentation and Measurement, IEEE Transactions on,* vol. 40, pp. 228-230, 1991.

[142] Y. C. Shih, M. Murakami, E. L. Wilkie, and A. C. Callegari, "Effects of interfacial microstructure on uniformity and thermal stability of AuNiGe ohmic contact to n-type GaAs," *Journal of Applied Physics,* vol. 62, pp. 582-590, 1987.

[143] A. G. Baca, F. Ren, J. C. Zolper, R. D. Briggs, and S. J. Pearton, "A survey of ohmic contacts to III-V compound semiconductors," *Thin Solid Films,* vol. 308–309, pp. 599-606, 1997.

[144] T. Sands, "Compound semiconductor contact metallurgy," *Materials Science and Engineering: B,* vol. 1, pp. 289-312, 1988.

[145] A. Messica, U. Meirav, and H. Shtrikman, "Refractory metal-based low-resistance ohmic contacts for submicron GaAs heterostructure devices," *Thin Solid Films,* vol. 257, pp. 54-57, 1995.

[146] R. Kohler, A. Tredicucci, F. Beltram, H. E. Beere, E. H. Linfield, A. G. Davies, *et al.*, "High-performance continuous-wave operation of superlattice terahertz quantum-cascade lasers," *Applied Physics Letters,* vol. 82, pp. 1518-1520, 2003.

[147] M. Fukuda, *Optical Semiconductor Devices*: John Wiley & Sons, 1999.

[148] T.-T. Lin and H. Hirayama, "Improvement of operation temperature in GaAs/AlGaAs THz-QCLs by utilizing high Al composition barrier," *physica status solidi (c),* vol. 10, pp. 1430-1433, 2013.

[149] N. M. Hinchcliffe, "Fabrication and measurement of double metal terahertz quantum cascade lasers," PhD Thesis, School of Electronic and Electrical Engineering, University of Leeds, 2009.

[150] D. H. Barker, D. T. Hodges, and T. S. Hartwick, "Far Infrared Imagery," in *Proc. SPIE 0067, Long-Wavelength Infrared, 27*, 1975, pp. 27-36.

[151] T. S. Hartwick, D. T. Hodges, D. H. Barker, and F. B. Foote, "Far infrared imagery," *Applied Optics,* vol. 15, pp. 1919-1922, 1976.

[152] T. Kleine-Ostmann, P. Knobloch, M. Koch, S. Hoffmann, M. Breede, M. Hofmann, *et al.*, "Continuous-wave THz imaging," *Electronics Letters,* vol. 37, pp. 1461 -1463, 2001.

[153] A. J. Fitzgerald, E. Berry, N. N. Zinovev, G. C. Walker, M. A. Smith, and J. M. Chamberlain, "An introduction to medical imaging with coherent terahertz frequency radiation," *Physics in Medicine and Biology,* vol. 47, p. R67, 2002-04-07 2002.

[154] D. J. Cook, B. K. Decker, G. Dadusc, and M. G. Allen, "Through-container THz sensing: applications for biodetection," in *Proc. SPIE 5268, Chemical and Biological Standoff Detection, 36*, 2004, pp. 36-42.

[155] S. M. Kim, F. Hatami, J. S. Harris, A. W. Kurian, J. Ford, D. King, *et al.*, "Biomedical terahertz imaging with a quantum cascade laser," *Applied Physics Letters,* vol. 88, pp. 153903-3, 2006.

[156] M. Walther, B. Fischer, A. Ortner, A. Bitzer, A. Thoman, and H. Helm, "Chemical sensing and imaging with pulsed terahertz radiation," *Analytical and Bioanalytical Chemistry,* vol. 397, pp. 1009-1017, 2010.

[157] W. H. Fan, A. Burnett, P. C. Upadhya, J. Cunningham, E. H. Linfield, and A. G. Davies, "Far-infrared spectroscopic characterization of explosives for security applications using broadband terahertz time-domain spectroscopy," *Applied Spectroscopy,* vol. 61, pp. 638-643, 2007.

[158] Y. C. Shen, T. Lo, P. F. Taday, B. E. Cole, W. R. Tribe, and M. C. Kemp, "Detection and identification of explosives using terahertz pulsed spectroscopic imaging," *Applied Physics Letters,* vol. 86, pp. 241116-3, 2005.

[159] H. Zhong, A. Redo-Sanchez, and X. C. Zhang, "Identification and classification of chemicals using terahertz reflective spectroscopic focal-plane imaging system," *Opt. Express,* vol. 14, pp. 9130-9141, 2006.

[160] H.-B. Liu, Y. Chen, G. J. Bastiaans, and X.-C. Zhang, "Detection and identification of explosive RDX by THz diffuse reflection spectroscopy," *Opt. Express,* vol. 14, pp. 415–423, 2006.

[161] A. Sengupta, A. Bandyopadhyay, R. B. Barat, D. E. Gary, and J. F. Federici, "THz reflection spectroscopy of C-4 explosive and its detection through interferometric imaging," in *Proc. SPIE 6120, Terahertz and Gigahertz Electronics and Photonics V*, 2006, pp. 61200A-61200A-13.

[162] P. Dean, M. U. Shaukat, S. P. Khanna, S. Chakraborty, M. Lachab, A. Burnett, *et al.*, "Absorption-sensitive diffuse reflection imaging of concealed powders using a terahertz quantum cascade laser," *Optics Express,* vol. 16, pp. 5997-6007, 2008.

[163] M. A. Brun, F. Formanek, A. Yasuda, M. Sekine, N. Ando, and Y. Eishii, "Terahertz imaging applied to cancer diagnosis," *Physics in Medicine and Biology,* vol. 55, p. 4615, 2010.

[164] S.-H. Ding, Q. Li, R. Yao, and Q. Wang, "High-resolution terahertz reflective imaging and image restoration," *Applied Optics,* vol. 49, pp. 6834-6839, 2010.

[165] P. Dean, A. D. Burnett, K. Tych, S. P. Khanna, M. Lachab, J. E. Cunningham, *et al.*, "Measurement and analysis of the diffuse reflectance of powdered samples at terahertz frequencies using a quantum cascade laser," *Journal of Chemical Physics,* vol. 134, 2011.

[166] K. Serita, S. Mizuno, H. Murakami, I. Kawayama, Y. Takahashi, M. Yoshimura, *et al.*, "Scanning laser terahertz near-field imaging system," *Optics Express,* vol. 20, pp. 12959-12965, 2012.

[167] R. Lecaque, S. Grésillon, N. Barbey, R. Peretti, J.-C. Rivoal, and C. Boccara, "THz near-field optical imaging by a local source," *Optics Communications,* vol. 262, pp. 125-128, 2006.

[168] H. Shimosato, M. Ashida, T. Itoh, S. Saito, and K. Sakai, "Ultrabroadband Detection of Terahertz Radiation from 0.1 to 100 THz with Photoconductive Antenna," in *Ultrafast Optics V*. vol. 132, S. Watanabe and K. Midorikawa, Eds., ed: Springer New York, 2007, pp. 317-323.

[169] T. Breslin, F. Xu, G. Palmer, C. Zhu, K. Gilchrist, and N. Ramanujam, "Autofluorescence and diffuse reflectance properties of malignant and benign breast tissues," *Annals of Surgical Oncology,* vol. 11, pp. 65-70, 2004.

[170] E. Rakhmatullina, A. Bossen, C. Höschele, X. Wang, B. Beyeler, C. Meier, *et al.*, "Application of the specular and diffuse reflection analysis for in vitro diagnostics of dental erosion: correlation with enamel softening, roughness, and calcium release," *Journal of Biomedical Optics,* vol. 16, pp. 107002-107002-12, 2011.

[171] B. Yu, H. L. Fu, and N. Ramanujam, "Instrument independent diffuse reflectance spectroscopy," *Journal of Biomedical Optics,* vol. 16, pp. 011010-011010-12, 2011.

[172] A. Van der Harten, T. Gulsrud, L. Kirkegaard, and A. Kiel, "A Multi-faceted Study of Sound Diffusing Elements in an Auditorium," *Proceedings of Meetings on Acoustics,* vol. 12, p. 015006, 2011.

[173] S. W. Hasinoff, A. Levin, P. R. Goode, and W. T. Freeman, "Diffuse reflectance imaging with astronomical applications," in *Computer Vision (ICCV), 2011 IEEE International Conference on*, 2011, pp. 185-192.

[174] R. A. Viscarra Rossel, D. J. J. Walvoort, A. B. McBratney, L. J. Janik, and J. O. Skjemstad, "Visible, near infrared, mid infrared or combined diffuse reflectance spectroscopy for simultaneous assessment of various soil properties," *Geoderma,* vol. 131, pp. 59-75, 2006.

[175] G. Raschke, S. Kowarik, T. Franzl, C. Sönnichsen, T. A. Klar, J. Feldmann, *et al.*, "Biomolecular Recognition Based on Single Gold Nanoparticle Light Scattering," *Nano Letters,* vol. 3, pp. 935-938, 2003.

[176] M. P. Fuller and P. R. Griffiths, "Diffuse reflectance measurements by infrared Fourier transform spectrometry," *Analytical Chemistry,* vol. 50, pp. 1906-1910, 1978.

[177] D. J. J. Fraser and P. R. Griffiths, "Effect of scattering coefficient on diffuse reflectance infrared spectra," *Appl. Spectrosc.,* vol. 44, pp. 193–199, 1990.

[178] R. A. Viscarra Rossel, R. N. McGlynn, and A. B. McBratney, "Determining the composition of mineral-organic mixes using UV–vis–NIR diffuse reflectance spectroscopy," *Geoderma,* vol. 137, pp. 70-82, 2006.

[179] M. J. Barajas, A. R. Cassiani, W. Vargas, C. Conde, J. Ropero, J. Figueroa, *et al.*, "Near-infrared spectroscopic method for real-time monitoring of pharmaceutical powders during voiding," *Appl Spectrosc,* vol. 61, pp. 490-6, 2007.

[180] A. W. M. Lee, Q. Qin, S. Kumar, B. S. Williams, Q. Hu, and J. L. Reno, "Real-time terahertz imaging over a standoff distance (>25 meters)," *Appl. Phys. Lett.*, vol. 89, p. 141125, 2006.

[181] P. Dean, N. K. Saat, S. P. Khanna, M. Salih, A. Burnett, J. Cunningham*, et al.*, "Dual-frequency imaging using an electrically tunable terahertz quantum cascade laser," *Optics Express,* vol. 17, pp. 20631-20641, 2009.

[182] P. Dean, S. Khanna, S. Chakraborty, M. Lachab, A. G. Davies, and E. H. Linfield, "Diffuse reflection imaging at terahertz frequencies for security applications," in *Proc. SPIE 6741, Optics and Photonics for Counterterrorism and Crime Fighting III*, Florence, Italy, 2007, pp. 67410R-67410R-9.

[183] S. P. Khanna, M. Salih, P. Dean, A. G. Davies, and E. H. Linfield, "Electrically tunable terahertz quantum-cascade laser with a heterogeneous active region," *Applied Physics Letters,* vol. 95, 2009.

[184] H. Luo, S. R. Laframboise, Z. R. Wasilewski, G. C. Aers, H. C. Liu, and J. C. Cao, "Terahertz quantum-cascade lasers based on a three-well active module," *Applied Physics Letters,* vol. 90, p. 041112, 2007.

[185] S. P. Khanna, S. Chakraborty, M. Lachab, N. M. Hinchcliffe, E. H. Linfield, and A. G. Davies, "The growth and measurement of terahertz quantum cascade lasers," *Physica E: Low-dimensional Systems and Nanostructures,* vol. 40, pp. 1859-1861, 2008.

[186] A. Valavanis, P. Dean, Y. L. Lim, R. Alhathlool, A. D. Burnett, S. Chowdhury, *et al.*, "Detection of concealed weapons and characterisation of crystalline powders using terahertz quantum cascade lasers," in *UK Semiconductors 2012*, Sheffield, UK, 2012.

[187] A. Valavanis, S. Chowdhury, A. Burnett, A. R. Clarkson, D. R. Bacon, S. P. Khanna*, et al.*, "Spectroscopic diffuse-reflectance imaging with a frequency-switchable terahertz quantum cascade laser," *IEEE Transactions on Terahertz Science and Technology,* 2015 [accepted].

[188] J. W. Coltman, "The specification of imaging properties by response to a sine wave input," *Journal of the Optical Society of America,* vol. 44, p. 468, 1954.

[189] P. U. Jepsen and B. M. Fischer, "Dynamic range in terahertz time-domain transmission and reflection spectroscopy," *Optics Letters,* vol. 30, pp. 29-31, 2005.

[190] P. U. Jepsen, D. G. Cooke, and M. Koch, "Terahertz spectroscopy and imaging – Modern techniques and applications," *Laser & Photonics Reviews,* vol. 5, pp. 124-166, 2011.

[191] J. E. Eberhardt, J. G. Haub, and A. W. Pryor, "Reflectivity of natural and powdered minerals at CO_2 laser wavelengths," *Appl. Opt.,* vol. 24, pp. 388–395, 1985.

[192] A. Valavanis, P. Dean, S. Chowdhury, A. D. Burnett, S. P. Khanna, A. G. Davies, *et al.*, "Spectroscopic analysis of powders through diffuse-reflectance imaging using a frequency-switchable terahertz quantum cascade laser," in *IRMMW-THz 2013: The 38th International Conference on Infrared, Millimeter and Terahertz Waves*, Mainz on the Rhine, Germany, 2013.

[193] J. D. Lindberg, "Absolute diffuse reflectance from relative reflectance measurements," *Applied Optics,* vol. 26, pp. 2900-2905, 1987.

[194] J. D. Lindberg, R. E. Douglass, and D. M. Garvey, "Absorption-coefficient-determination method for particulate materials," *Applied Optics,* vol. 33, pp. 4314-4319, 1994.

[195] H. H. Ku, "Notes on the Use of Propagation of Error Formulas," *J Research of National Bureau of Standards-C. Engineering and Instrumentation,* vol. 70C, pp. 263-273, 1966.

[196] E. F. Plinski, "Terahertz photomixer," *Bulletin of the Polish Academy of Sciences, Technical Sciences,* vol. 58, pp. 463-70, 2010.

[197] S. Preu, G. H. Döhler, S. Malzer, L. J. Wang, and A. C. Gossard, "Tunable, continuous-wave Terahertz photomixer sources and applications," *Journal of Applied Physics,* vol. 109, p. 061301, 2011.

[198] E. R. Brown, "THz Generation by Photomixing in Ultrafast Photoconductors," *International Journal of High Speed Electronics and Systems,* vol. 13, pp. 497-545, 2003/06/01 2003.

[199] I. S. Gregory, "The development of a continuous-wave terahertz imaging system," PhD thesis, Semiconductor Physics group, Cavendish Laboratory, University of Cambridge, 2004.

[200] I. S. Gregory, C. Baker, W. R. Tribe, I. V. Bradley, M. J. Evans, E. H. Linfield, *et al.*, "Optimization of photomixers and antennas for continuous-wave terahertz emission," *Quantum Electronics, IEEE Journal of,* vol. 41, pp. 717-728,

2005.

[201] E. R. Brown, F. W. Smith, and K. A. McIntosh, "Coherent millimeter-wave generation by heterodyne conversion in low-temperature-grown GaAs photoconductors," *Journal of Applied Physics,* vol. 73, pp. 1480-1484, 1993.

[202] K. A. McIntosh, E. R. Brown, K. B. Nichols, O. B. McMahon, W. F. DiNatale, and T. M. Lyszczarz, "Terahertz measurements of resonant planar antennas coupled to low-temperature-grown GaAs photomixers," *Applied Physics Letters,* vol. 69, pp. 3632-3634, 1996.

[203] C. Kadow, A. W. Jackson, A. C. Gossard, S. Matsuura, and G. A. Blake, "Self-assembled ErAs islands in GaAs for optical-heterodyne THz generation," *Applied Physics Letters,* vol. 76, pp. 3510-3512, 2000.

[204] J. E. Bjarnason, T. L. J. Chan, A. W. M. Lee, E. R. Brown, D. C. Driscoll, M. Hanson, *et al.*, "ErAs:GaAs photomixer with two-decade tunability and 12μW peak output power," *Applied Physics Letters,* vol. 85, pp. 3983-3985, 2004.

[205] C. Baker, I. Gregory, M. Evans, W. Tribe, E. Linfield, and M. Missous, "All-optoelectronic terahertz system using low-temperature-grown InGaAs photomixers," *Optics Express,* vol. 13, pp. 9639-9644, 2005/11/14 2005.

[206] M. Suzuki and M. Tonouchi, "Fe-implanted InGaAs terahertz emitters for 1.56μm wavelength excitation," *Applied Physics Letters,* vol. 86, p. 051104, 2005.

[207] D. C. Driscoll, M. P. Hanson, A. C. Gossard, and E. R. Brown, "Ultrafast photoresponse at 1.55 μm in InGaAs with embedded semimetallic ErAs nanoparticles," *Applied Physics Letters,* vol. 86, p. 051908, 2005.

[208] N. Chimot, J. Mangeney, L. Joulaud, P. Crozat, H. Bernas, K. Blary, *et al.*, "Terahertz radiation from heavy-ion-irradiated In0.53Ga0.47As photoconductive antenna excited at 1.55μm," *Applied Physics Letters,* vol. 87, p. 193510, 2005.

[209] B. Sartorius, H. Roehle, H. Künzel, J. Böttcher, M. Schlak, D. Stanze, *et al.*, "All-fiber terahertz time-domain spectrometer operating at 1.5 μm telecom wavelengths," *Optics Express,* vol. 16, pp. 9565-9570, 2008/06/23 2008.

[210] C. D. Wood, O. Hatem, J. E. Cunningham, E. H. Linfield, A. G. Davies, P. J. Cannard, *et al.*, "Terahertz emission from metal-organic chemical vapor deposition grown Fe:InGaAs using 830 nm to 1.55μm excitation," *Applied Physics Letters,* vol. 96, p. 194104, 2010.

[211] A. Fekecs, M. Bernier, D. Morris, M. Chicoine, F. Schiettekatte, P. Charette, *et al.*, "Fabrication of high resistivity cold-implanted InGaAsP photoconductors for efficient pulsed terahertz devices," *Optical Materials Express,* vol. 1, pp. 1165-1177, 2011/11/01 2011.

[212] I. S. Gregory, W. R. Tribe, B. E. Cole, M. J. Evans, E. H. Linfield, A. G. Davies, *et al.*, "Resonant dipole antennas for continuous-wave terahertz photomixers," *Applied Physics Letters,* vol. 85, pp. 1622-1624, 2004.

[213] R. Mendis, C. Sydlo, J. Sigmund, M. Feiginov, P. Meissner, and H. L. Hartnagel, "Tunable CW-THz system with a log-periodic photoconductive emitter," *Solid-State Electronics,* vol. 48, pp. 2041-2045, 10// 2004.

[214] N. Kim, S.-P. Han, H. Ko, Y. A. Leem, H.-C. Ryu, C. W. Lee, *et al.*, "Tunable continuous-wave terahertz generation/detection with compact 1.55 μm detuned dual-mode laser diode and InGaAs based photomixer," *Optics Express,* vol. 19, pp. 15397-15403, 2011/08/01 2011.

[215] HITRAN [Online]. Available: https://www.cfa.harvard.edu/hitran/

[216] J. TrÄgÅrdh, K. Macrae, C. Travis, R. Amor, G. Norris, S. H. Wilson, *et al.*, "A simple but precise method for quantitative measurement of the quality of the laser focus in a scanning optical microscope," *Journal of Microscopy,* vol. 259, pp. 66-73, 2015.

[217] G. Veshapidze, M. L. Trachy, M. H. Shah, and B. D. DePaola, "Reducing the uncertainty in laser beam size measurement with a scanning edge method," *Applied Optics,* vol. 45, pp. 8197-8199, 2006/11/10 2006.

[218] M. González-Cardel, P. Arguijo, and R. Díaz-Uribe, "Gaussian beam radius measurement with a knife-edge: a polynomial approximation to the inverse error function," *Applied Optics,* vol. 52, pp. 3849-3855, 2013/06/01 2013.

[219] I. S. Gregory, C. Baker, W. R. Tribe, M. J. Evans, H. E. Beere, E. H. Linfield, *et al.*, "High resistivity annealed low-temperature GaAs with 100 fs lifetimes," *Applied Physics Letters,* vol. 83, pp. 4199-4201, 2003.

[220] A. Claverie and Z. Liliental-Weber, "Extended defects and precipitates in LT-GaAs, LT-InAlAs and LT-InP," *Materials Science and Engineering: B,* vol. 22, pp. 45-54, 1993.

[221] J. J. Kuta, H. M. van Driel, D. Landheer, and J. A. Adams, "Polarization and wavelength dependence of metal-semiconductor-metal photodetector

response," *Applied Physics Letters,* vol. 64, pp. 140-142, 1994.

[222] S. Chowdhury, J. R. Freeman, M. C. Rosamond, R. A. Mohandas, M. Kumar, L. Li, *et al.*, "Study of the effect of annealing temperature on low-temperature-grown-GaAs photomixers," in *UK Semiconductors 2015*, Sheffield, UK.

[223] K. Grigoras, A. Krotkus, and A. Deringas, "Picosecond lifetime measurement in semiconductor by optoelectronic autocorrelation," *Electronics Letters,* vol. 27, pp. 1024-1025, 1991.

[224] N. C. Hunter, "Picosecond Pulse Measurements of Graphene," PhD Thesis, School of Electronic and Electrical Engineering, University of Leeds, 2015.

[225] R. H. Jacobsen, K. Birkelund, T. Holst, P. Uhd Jepsen, and S. R. Keiding, "Interpretation of photocurrent correlation measurements used for ultrafast photoconductive switch characterization," *Journal of Applied Physics,* vol. 79, pp. 2649-2657, 1996.

[226] S. Verghese, N. Zamdmer, Q. Hu, E. R. Brown, and A. Förster, "An optical correlator using a low-temperature-grown GaAs photoconductor," *Applied Physics Letters,* vol. 69, pp. 842-844, 1996.

[227] D. Li, L. Wei zhu, S. Zhen rong, and W. Zu geng, "Response characteristic of femtosecond LT-GaAs photoconductive switches at different voltage biases," *Journal of Physics D: Applied Physics,* vol. 42, p. 245103, 2009.

[228] C. Russell, "Broadband on-chip terahertz spectroscopy," PhD Thesis, School of Electronic and Electrical Engineering, University of Leeds, 2013.

[229] J. L. Hartke, "The Three-Dimensional Poole-Frenkel Effect," *Journal of Applied Physics,* vol. 39, pp. 4871-4873, 1968.

[230] G. A. Dussel and K. W. Böer, "Field-Enhanced Ionization," *physica status solidi (b),* vol. 39, pp. 375-389, 1970.

[231] T. H. Ning, "High-field capture of electrons by Coulomb-attractive centers in silicon dioxide," *Journal of Applied Physics,* vol. 47, pp. 3203-3208, 1976.

[232] T. Mohr, S. Breuer, D. Blömer, M. Simonetta, S. Patel, M. Schlosser, *et al.*, "Terahertz homodyne self-mixing transmission spectroscopy," *Applied Physics Letters,* vol. 106, p. 061111, 2015.

[233] J. M. Reix, T. Passvogel, G. Crone, B. Collaudin, P. Rideau, Y. Roche, *et al.*, "The Herschel/Planck programme, technical challenges for two science

missions, successfully launched," *Acta Astronautica,* vol. 66, pp. 130-148, 2010.

[234] F. Capasso, R. Paiella, R. Martini, R. Colombelli, C. Gmachl, T. L. Myers*, et al.*, "Quantum cascade lasers: ultrahigh-speed operation, optical wireless communication, narrow linewidth, and far-infrared emission," *Quantum Electronics, IEEE Journal of,* vol. 38, pp. 511-532, 2002.

[235] M. S. Vitiello, L. Consolino, S. Bartalini, A. Taschin, A. Tredicucci, M. Inguscio*, et al.*, "Quantum-limited frequency fluctuations in a terahertz laser," *Nat Photon,* vol. 6, pp. 525-528, 2012.

[236] M. Ravaro, P. Gellie, G. Santarelli, C. Manquest, P. Filloux, C. Sirtori*, et al.*, "Stabilization and mode locking of terahertz quantum cascade lasers," *Selected Topics in Quantum Electronics, IEEE Journal of,* vol. 19, pp. 8501011-8501011, 2013.

[237] A. Baryshev, J. N. Hovenier, A. J. L. Adam, I. Kašalynas, J. R. Gao, T. O. Klaassen*, et al.*, "Phase locking and spectral linewidth of a two-mode terahertz quantum cascade laser," *Applied Physics Letters,* vol. 89, p. 031115, 2006.

[238] P. Gellie, S. Barbieri, J.-F. Lampin, P. Filloux, C. Manquest, C. Sirtori*, et al.*, "Injection-locking of terahertz quantum cascade lasers up to 35GHz using RF amplitude modulation," *Optics Express,* vol. 18, pp. 20799-20816, 2010.

[239] R. Adler, "A study of locking phenomena in oscillators," *Proceedings of the IEEE,* vol. 61, pp. 1380-1385, 1973.

[240] A. L. Betz, R. T. Boreiko, B. S. Williams, S. Kumar, Q. Hu, and J. L. Reno, "Frequency and phase-lock control of a 3 THz quantum cascade laser," *Optics Letters,* vol. 30, pp. 1837-9, 2005.

[241] A. A. Danylov, T. M. Goyette, J. Waldman, M. J. Coulombe, A. J. Gatesman, R. H. Giles*, et al.*, "Frequency stabilization of a single mode terahertz quantum cascade laser to the kilohertz level," *Optics Express,* vol. 17, pp. 7525-7532, 2009.

[242] D. Rabanus, U. U. Graf, M. Philipp, O. Ricken, J. Stutzki, B. Vowinkel*, et al.*, "Phase locking of a 1.5 Terahertz quantum cascade laser and use as a local oscillator in a heterodyne HEB receiver," *Opt. Express,* vol. 17, pp. 1159-1168, 2009.

[243] P. Khosropanah, A. Baryshev, W. Zhang, W. Jellema, J. N. Hovenier, J. R. Gao, *et al.*, "Phase locking of a 2.7 THz quantum cascade laser to a microwave

reference," *Optics Letters,* vol. 34, pp. 2958-60, 2009.

[244] A. A. Danylov, A. R. Light, J. Waldman, N. R. Erickson, X. Qian, and W. D. Goodhue, "2.32 THz quantum cascade laser frequency-locked to the harmonic of a microwave synthesizer source," *Optics Express,* vol. 20, pp. 27908-27914, 2012.

[245] H. Richter, S. G. Pavlov, A. D. Semenov, L. Mahler, A. Tredicucci, H. E. Beere, *et al.*, "Submegahertz frequency stabilization of a terahertz quantum cascade laser to a molecular absorption line," *Applied Physics Letters,* vol. 96, p. 071112, 2010.

[246] Y. Ren, J. N. Hovenier, M. Cui, D. J. Hayton, J. R. Gao, T. M. Klapwijk, *et al.*, "Frequency locking of single-mode 3.5-THz quantum cascade lasers using a gas cell," *Applied Physics Letters,* vol. 100, p. 041111, 2012.

[247] Y. Ren, D. J. Hayton, J. N. Hovenier, M. Cui, J. R. Gao, T. M. Klapwijk, *et al.*, "Frequency and amplitude stabilized terahertz quantum cascade laser as local oscillator," *Applied Physics Letters,* vol. 101, p. 101111, 2012.

[248] S. Barbieri, P. Gellie, G. Santarelli, L. Ding, W. Maineult, C. Sirtori, *et al.*, "Phase-locking of a 2.7-THz quantum cascade laser to a mode-locked erbium-doped fibre laser," *Nat Photon,* vol. 4, pp. 636-640, 2010.

[249] M. Ravaro, C. Manquest, C. Sirtori, S. Barbieri, G. Santarelli, K. Blary, *et al.*, "Phase-locking of a 2.5 THz quantum cascade laser to a frequency comb using a GaAs photomixer," *Opt. Lett.*, vol. 36, pp. 3969-3971, 2011.

[250] A. E. Siegman, *Lasers*: University Science Books, 1986.

[251] D. Oustinov, N. Jukam, R. Rungsawang, J. Madéo, S. Barbieri, P. Filloux, *et al.*, "Phase seeding of a terahertz quantum cascade laser," *Nat Commun,* vol. 1, p. 69, 2010.

[252] J. Madeo, P. Cavalie, J. R. Freeman, N. Jukam, J. Maysonnave, K. Maussang, *et al.*, "All-optical wavelength shifting in a semiconductor laser using resonant nonlinearities," *Nat Photon,* vol. 6, pp. 519-524, 08//print 2012.

[253] R. P. Green, J.-H. Xu, L. Mahler, A. Tredicucci, F. Beltram, G. Giuliani, *et al.*, "Linewidth enhancement factor of terahertz quantum cascade lasers," *Applied Physics Letters,* vol. 92, p. 071106, 2008.

[254] P. Dean, Y. Leng Lim, A. Valavanis, R. Kliese, M. Nikolić, S. P. Khanna, *et al.*, "Terahertz imaging through self-mixing in a quantum cascade laser," *Optics*

Letters, vol. 36, pp. 2587-2589, 2011.

[255] I. Kundu, P. Dean, A. Valavanis, L. Chen, L. Li, J. E. Cunningham, *et al.*, "Discrete Vernier tuning in terahertz quantum cascade lasers using coupled cavities," *Optics Express,* vol. 22, pp. 16595-16605, 2014.

[256] M. S. Vitiello and A. Tredicucci, "Tunable emission in THz quantum cascade lasers," *IEEE Transactions on Terahertz Science and Technology,* vol. 1, pp. 76-84, 2011.

[257] S. Chakraborty, O. Marshall, C. W. Hsin, M. Khairuzzaman, H. Beere, and D. Ritchie, "Discrete mode tuning in terahertz quantum cascade lasers," *Optics Express,* vol. 20, p. B306, 2012.

[258] V. Torres-Company and A. M. Weiner, "Optical frequency comb technology for ultra-broadband radio-frequency photonics," *Laser & Photonics Reviews,* vol. 8, pp. 368-393, 2014.

[259] D. Turčinková, G. Scalari, F. Castellano, M. I. Amanti, M. Beck, and J. Faist, "Ultra-broadband heterogeneous quantum cascade laser emitting from 2.2 to 3.2 THz," *Applied Physics Letters,* vol. 99, p. 191104, 2011.

[260] J. Maysonnave, N. Jukam, M. S. M. Ibrahim, K. Maussang, J. Madéo, P. Cavalié, *et al.*, "Integrated injection seeded terahertz source and amplifier for time-domain spectroscopy," *Optics Letters,* vol. 37, pp. 731-733, 2012.